Sparse Methods for Hyperspectral Unmixing and Image Fusion

Dissertation

zur Erlangung
des Doktorgrades der Naturwissenschaften (Dr. rer. nat.)
des Fachbereichs Mathematik / Informatik
der Universität Osnabrück

vorgelegt
von

Jakub Bieniarz

Osnabrück, 2015

Sparse Methods for Hyperspectral Unmixing and Image Fusion

Dissertation

zur Erlangung
des Doktorgrades der Naturwissenschaften (Dr. rer. nat.)
des Fachbereichs Mathematik / Informatik
der Universität Osnabrück

vorgelegt
von

Jakub Bieniarz

Erstgutachter:
Hon.–Prof. Dr.–Ing. Peter Reinartz
Zweitgutachter:
Prof. Dr.–Ing. Manfred Ehlers
Tag der mündlichen Prüfung: 2. Dezember 2015

Osnabrück, 2015

Sparse Methods for Hyperspectral Unmixing and Image Fusion

Abstract

In recent years, the substantial increase in the number of spectral channels in optical remote sensing sensors allows more detailed spectroscopic analysis of objects on the Earth surface. Modern hyperspectral sensors are able to sample the sunlight reflected from a target on the ground with hundreds of adjacent narrow spectral channels. However, the increased spectral resolution comes at the price of a lower spatial resolution, e.g. the forthcoming German hyperspectral sensor Environmental Mapping and Analysis Program (EnMAP) which will have 244 spectral channels and a pixel size on ground as large as 30 m $\times$ 30 m. The main aim of this thesis is dealing with the problem of reduced spatial resolution in hyperspectral sensors. This is addressed first as an unmixing problem, i.e., extraction and quantification of the spectra of pure materials mixed in a single pixel, and second as a resolution enhancement problem based on fusion of multispectral and hyperspectral imagery.

This thesis proposes novel methods for hyperspectral unmixing using sparse approximation techniques and external spectral dictionaries, which unlike traditional least squares-based methods, do not require pure material spectrum selection step and are thus able to simultaneously estimate the underlying active materials along with their respective abundances. However, in previous works it has been shown that these methods suffer from some drawbacks, mainly from the intra dictionary coherence. To improve the performance of sparse spectral unmixing, the use of derivative transformation and a novel two step group unmixing algorithm are proposed. Additionally, the spatial homogeneity of abundance vectors by introducing a multi-look model for spectral unmixing is exploited.

Based on the above findings, a new method for fusion of hyperspectral images with higher spatial resolution multispectral images is proposed. The algorithm exploits the spectral information of the hyperspectral image and the spatial information from the multispectral image by means of sparse spectral unmixing to form a new high spatial and spectral resolution hyperspectral image. The introduced method is robust when applied to highly mixed scenarios as it relies on external spectral dictionaries.

Both the proposed sparse spectral unmixing algorithms as well as the resolution enhancement approach are evaluated quantitatively and qualitatively. Algorithms developed in this thesis are significantly faster and yield better or similar results to state-of-the-art methods.

Zusammenfassung

Eine deutliche Erhöhung der Anzahl von spektralen Kanälen in optischen Fernerkundungssensoren ermöglicht genauere spektroskopische Analysen von Objekten auf der Erdoberfläche. Moderne hyperspektrale Sensoren sind in der Lage, das reflektierte Licht mit Hunderten angrenzenden schmalen spektralen Kanälen aufzuzeichnen. Die hohe spektrale Auflösung führt jedoch zu einer geringeren räumlichen Auflösung, so besitzt z.B. der deutsche Hyperspektralsensor EnMAP (Environmental Mapping and Analysis Program) mit 244 spektralen Kanälen nur eine Pixelgröße von 30 m auf dem Boden. Hauptmotivation dieser Dissertation ist das Problem der reduzierten räumlichien Auflösung in der hyperspektralen Fernerkundung zu behandeln. Mögliche Optimierungen hierzu sind die spektrale Entmischung, das heißt, Extraktion und Quantifizierung der Spektren von reinen Materialien in einem einzelnen Pixel, und die Auflösungsverbesserung basierend auf Fusion von multispektralen und hyperspektralen Bilder unter Benutzung der Entmischungsalgorithmen.

In dieser Arbeit wird ein neuartiges Verfahren zur hyperspektralen Entmischung mit Sparse-Approximationstechniken und spektralen Bibliotheken vorgeschlagen, die im Gegensatz zu der herkömmlichen, auf kleinste Quadrate basierten Methode, eine Endmember Vorauswahl erfordert und somit in der Lage ist, gleichzeitig die in jedem Pixel vorhandenen Materialien zusammen mit ihrer jeweiligen Häufigkeiten zu schätzen. In früheren Arbeiten wurde gezeigt, daß diese Verfahren einige Nachteile haben, hauptsächlich aufgrund der Kohärenz innerhalb der Bibliotheken. Zur Verbesserung der Entmischung wird ein Ansatz über Ableitungen sowie ein neuer dualer Algorithmus vorgeschlagen. Darüber hinaus wird der Ansatz dahingehend erweitert, die räumliche Homogenität des Abundance-Vektors durch Einführung eines Multi-Look-Modells für die Entmischung zu nutzen.

Basierend auf den oben ausgeführten Entwicklungen wird ein neues Verfahren zur Fusion von Hyperspektraldaten mit höher räumlich aufgelösten Multispektraldaten vorgeschlagen. Der Algorithmus nutzt die spektralen Informationen der hyperspektralen Bilder und die räumliche Information aus multispektralen Bildern durch sparse-Entmischung, um ein neues Bild hoher räumlicher und spektraler Auflösung zu erzeugen. Durch die verwendete spektrale Bibliothek ist das vorgeschlagene Verfahren auch dann robust, wenn es in komplexen Szenarien angewendet wird.

Die vorgeschlagenen sparse-Entmischungs Algorithmen sowie die Auflösungsverbesserung werden schließlich quantitativ und qualitativ bewertet. Es wird gezeigt, dass die entwickelten Algorithmen wesentlich schneller sind und bessere oder ähnliche Ergebnisse wie die state-of-the-Art-Methoden liefern.

Acknowledgments

At first, I would like to express my gratitude to Rupert Müller who has played a fundamental role as my supervisor at the DLR German Aerospace Center during my doctoral work. Rupert provided me with valuable guidance, assistance and expertise without which I would not have been able to successfully complete this thesis. I am grateful to my doctoral advisor Prof. Peter Reinartz for giving me the opportunity to conduct this research work, as well as his helpful guidance, support and motivation. I could not have imagined a better supervisor and advisor than Rupert and Peter. I would also like to thank Prof. Xiaoxiang Zhu for her valuable advices and discussions as well as for carefully reviewing my thesis. I am grateful to Prof. Manfred Ehlers from the University Osnabruck for his insightful comments and remarks to my work.

I would like to thank the German Academic Exchange Service (DAAD) for financially supporting my research work. Moreover, many thanks go to Prof. Richard Bamler, director of the DLR Remote Sensing Technology Institute (MF),for many precious suggestions and for enabling me to conduct my research work in the friendly and stimulating environment.

Furthermore, I would like to thank Prof. Mario Parente for inviting for a scientific exchange in his group at the University of Massathusets Amherst. Through the introduction to planetary remote sensing has contributed to the part of my thesis in which I applied my methods to the Martian data.

Special thanks go to all of my DLR colleagues. In particular, Daniele for not only a being a great office mate, but also an advisor in many aspects during my research work. Janja, Jagmal, Claas, Muriel, Kevin, Octa and Esteban for being colleagues and friends beyond the work. I would also like to thank Rolf Stätter for great private discussions and his help in reviewing this thesis.

My deepest appreciation goes to Kasia for her priceless support, for helping me stay motivated during the time of my PhD. Kasia also provided helpful corrections for this thesis. Finally, I would like to thank my whole family for their constant support.

Contents

List of Figures

Acronyms

κ	Cohen's Kappa.
A-MSE	Abundance Mean Squared Error.
ACC	Accuracy.
AISA	Airborne Hyperspectral Imaging Systems.
AVIRIS	Airborne visible/infrared imaging spectrometer.
BPDN	Basis Pursuit Denoising.

CNMF	Coupled non-Negative Matrix Factorization.
CRISM	Compact Reconnaissance Imaging Spectrometer for Mars.
EM	Endmember.
FCLS	Fully-Constrained Least Squares.
FISTA	Fast Iterative Shrinkage-Thresholding Algorithm.
FN	False Negative.
FP	False Positive.
GSD	ground sampling distance.
HiRISE	High Resolution Imaging Science Experiment.
Hyperion	Hyperspectral Imaging sensor on Earth Observing-1 satellite.
JSM	Joint Sparsity Model.
LARS/LASSO	Least Angle Regression LASSO.
LASSO	Least Absolute Shrinkage and Selection Operator.
LMM	linear mixing model.
MAE	Mean Absolute Error.
MAP/SMM	maximum a posteriori stochastic mixing model.
MLJSF	Multi-Look Joint Sparsity Fusion.
MLJSM	Multi-Look Joint Sparsity Model.
MLJSR	Multi-Look Joint Sparsity Reconstruction.
MNS	Minimum-Norm Solution.
MRO	Mars Reconnaissance Orbiter.
MSE	Mean Squared Error.
nBPDN	non-negative Basis Pursuit Denoising.
NCC	normalised cross correlation.
NIR	near-infrared.

nLASSO	non-negative Least Absolute Shrinkage and Selection Operator.
NNLS	Non-Negative Least Squares.
NOMP	Non-Negative Orthogonal Matching Pursuit.
NRMSE	Normalised Root Mean Squared Error.
OA	overall accuracy.
OLS	Ordinary Least Squares.
OMP	Orthogonal Matching Pursuit.
PAN	panchromatic.
PSF	Point Spread Function.
R-MSE	Reflectance Mean Squared Error.
RSS	Residual Sum of Squares.
SAD	Spectral Angle Distance.
SAM	Spectral Angle Mapper.
SNR	Signal-to-Noise-Ratio.
SNT	Sensitivity.
SPAMS	SPArse Modeling Software.
SPC	Specificity.
SRE	Signal to Reconstruction Error.
SRF	Spectral Response Function.
SSIM	structural similarity.
SUnSAL	sparse unmixing via variable splitting augmented Lagrangian.
SUnSAL-TV	SUnSAL and Total Variation.
SWIR	short-wavelength infrared.
TN	True Negative.
TP	True Positive.
TSGU	Two Step Group Unmixing.
USGS	the United States Geological Survey.

VNIR	visible and near-infrared.
WV2	World View 2.

1

Introduction

The human eye contains three types of photoreceptor cells known as cones, each sensitive to a different range of light. Every cone type is able to distinguish 100 colors, allowing us to see 100^3 colors (Neitz et al., 2001). Yet, this spectral range and resolution is often not sufficient to e.g. distinguish salt from sugar or real from artificial plants. This is because the distinct *spectral features* are often very subtle or are located beyond the *spectral range* of the cones. Therefore if we would have hundred of cones making us able to distinguish 100^{100} colors, the question whether the object we are observing is sugar or salt would not be a problem any more.

As adding cones to the eye is impossible, a similar thing has been done with modern imaging sensors. The *hyperspectral* imaging sensors, with hundreds of narrow spectral channels spread over a wide spectral range, were developed to allow very detailed detection, classification and quantification of objects. Such sensors have been very quickly adapted in *remote sensing*, where the spectroscopic information enabled development of applications such as mineral mapping, vegetation healthy monitoring or environmental monitoring.

Unfortunately, the richness of spectral information comes at the price of a decrease in spatial information. Adding spectral channels means that the light has to be split among them, and in order to provide sufficient amount of light for each channel. The size of a pixel in the sensor or the dwelling time must be larger. This results in decrease of the *spatial resolution* i.e. the reduction of the amount of geometrical details visible in the image. Another problem arising with the reduced spatial resolution is the increased amount of *mixed pixels*, i.e., pixels containing a mixture of spectra from more than one pure material. This process is known as *spectral mixing* and its effect has essential impact in applications such as classification, detection or mapping. In this thesis both problems problems will be addressed.

Researchers found that the spectral mixing can be easily inverted using the rich spectral information delivered by the hyperspectral sensors. This inversion process, named *spectral unmixing*, is usually approached in two steps. At first, pure spectra of materials also known as endmembers are extracted from the image. Then, abundances, i.e., the amount of each endmember in every pixel, are estimated. The inversion can be done based on the assumed

mixing model e.g. using a *linear mixing model*, which states that the spectrum of a mixed pixel can be expressed as the integrated sum of the spectra of all endmembers within the captured pixel (Keshava, 2003). One way to obey the problem of endmember identification is to use a predefined set of labelled endmembers, e.g. measured in the laboratory, known as *spectral dictionary*. Assuming that in the image all possible endmembers can occur, such dictionary should be very large with usually many more endmembers than spectral channels. This fact makes the abundance estimation hard or even not possible using typical least squares based methods (Bioucas-Dias et al., 2012). However, in the past two decades researchers found many efficient ways to solve the at first glance 'unsolvable' problems when they fulfil the assumption that the estimates are *sparse* (Baraniuk, 2007; Baraniuk et al., 2008; Candes and Wakin, 2008; Chen et al., 1998; Donoho and Elad, 2003; Elad, 2010). What in essence means that the number of non-zero elements in the estimated vector is much less than the number of zero elements. This requirement based on the a priori information seems to be applicable to the *sparse spectral unmixing*, in which one expects to find only few endmembers in each hyperspectral image pixel. The spectral unmixing with large spectral dictionaries using a sparsity prior has been first used by Parente and Zymnis (2005), Iordache et al. (2011) and Bieniarz et al. (2012) but it has also been shown that this approach suffers from several drawbacks and limitations. Firstly, the large spectral dictionaries exhibit high *mutual coherence*, which affects the uniqueness of the results of sparse spectral unmixing (Bieniarz et al., 2012; Iordache et al., 2011). Secondly, the methods proposed to solve sparse spectral unmixing have a high computational complexity, making these algorithms inefficient with applications to large images. Finally, the pixel-based algorithms, in light of the high mutual coherence of the dictionary and noise in the data, often produce spatially inconsistent results (Bieniarz et al., 2015; Iordache et al., 2012b).

In order to find novel, more suitable sparse spectral unmixing methods, it is important to address the above problems. The first contributions contained in this work are focused on tackling the problem of the mutual coherence of spectral dictionaries. This is done in two manners, by expanding existing

sparse approximation algorithms with a preprocessing step, and by reducing the size of the spectral dictionary. Subsequently, the problem of spatial inconsistency is tackled by the introduction of a novel model for sparse spectral unmixing based on the linear mixing model but also taking into account spatial correlations among neighbouring pixels. Additionally, the use of the well studied algorithm Least Angle Regression LASSO (LARS/LASSO) is proposed to solve sparse unmixing problem which can significantly reduce execution time.

Spectral unmixing addresses the problem resulting from the decreased spatial resolution, but it also has been shown that it can be used to enhance the resolution of hyperspectral images (Zhukov et al., 1999). This is usually done by means of fusion of the spectral unmixing results from a lower spatial resolution hyperspectral image with a higher spatial resolution image. E.g. Yokoya et al. (2012) and Bieniarz et al. (2011) fused high spatial resolution multispectral image, i.e. an image characterised by a lower number of spectral channels than the hyperspectral image, with the result of image-based spectral unmixing. The main advantage of using these methods is the ability of reconstructing the high spatial resolution without losing the spectral resolution, which is usually the case when applying other sharpening methods Grohnfeldt et al. (2014). However, when the resolution of highly mixed hyperspectral image is low, these methods are hindered by the inaccuracies in the unmixing step. This drawback is addressed in this thesis by applying sparse unmixing methods for the unmixing, and a new multi-look model for fusion which accounts for spatial correlations in the higher spatial resolution image. Unlike in methods based on image-based unmixing, the complete set of spectra can not be used for the whole image. Thus, a novel window based method for hyperspectral-multispectral image fusion is presented.

This work is divided in three parts. The first part introduces the concepts which are essential for the understanding of the proposed methods and algorithms. Chapter 2 presents a theoretical background on optical remote sensing systems. This includes concepts of image generation with its typical problems but also the introduction to mixing and unmixing problems in hyperspectral imagery.

After introducing the data related theory, the background for the methodology is introduced in chapter 3. Here the methods and algorithms for solving underdetermined systems of equations are discussed, along with introducing typical regularisation problems and algorithms designed to solve these kind of problems.

In the second part the proposed methodology including algorithms and improvements is presented. First, the developments in sparse spectral unmixing are discussed in chapter 4. Here the concepts for reduction of coherence are presented. These are followed by the introduction of a novel unmixing algorithm, which improves the performance of sparse spectral unmixing with large spectral dictionaries. This chapter presents an algorithm for unmixing spatially correlated images, which is the main result of this thesis. Chapter 5 describes the developed algorithm for hyperspectral image resolution enhancement, and its contributions to the state of the art.

The third part of the thesis is dedicated to experimental results, evaluation of presented algorithms and conclusions. In chapter 6 the developed sparse spectral unmixing algorithms are compared to the state of the art highlighting the implemented improvements. Chapter 7 features experiments with resolution enhancement methods using several representative data sets, both simulated and real. Conclusions and ideas for future work are presented in chapter 8.

Part I

Theoretical Background

2

Hyperspectral Imaging – Remote Spectroscopy

The objective of this chapter is to present the basic concept of hyperspectral remote sensing as well as the principles of image generation. The physics of imaging spectroscopy including atmosphere effects on the image product will be discussed. Also, the definition of spectral, spatial resolution and noise in the hyperspectral image will be provided. Based on these introductory concepts first overview of spectral mixing and the unmixing principle will be considered.

In *optical remote sensing* electromagnetic signals propagated from the Earth are measured using a sensor mounted on an aircraft or spacecraft platform (Richards and Jia, 1999). These measurements quantify optical properties of the Earth's surface and atmosphere and are used as an input for numerous *remote sensing applications* ranging from environmental monitoring, through agricultural assessment to security and defence.

Most of the optical remote sensing sensors are *passive sensors* acquiring images by recording reflected sunlight or the electromagnetic radiation emitted by the objects. Such sensors can take images in a specific electromagnetic wavelength range commonly in the visible and near-infrared (VNIR) and sometimes short-wavelength infrared (SWIR). Optical remote sensing sensors can be classified depending on the number of spectral bands, i.e., providing one or more images at different spectral ranges:

- Panchromatic (PAN) sensors can take single images usually in a wide spectral range.
- *Multispectral* sensors are capable of acquiring simultaneously several images in different spectral ranges, i.e., several spectral bands.
- *Hyperspectral* sensors exhibit a large number of narrow, adjacent spectral bands covering a wide spectral range see Figure 2.1.

This thesis is dedicated to the development of new methods for hyperspectral image processing. In the following sections the basic concepts and theoretical background of this work will be discussed. Note that even though the main focus will be put on hyperspectral data all the physical background as well as image acquisition concepts are common with the multispectral data.

2.1 Physics of Imaging Spectroscopy

Hyperspectral imaging is known also as *imaging spectroscopy*. This name comes from the ability to take spectroscopic measurements allocated spatially

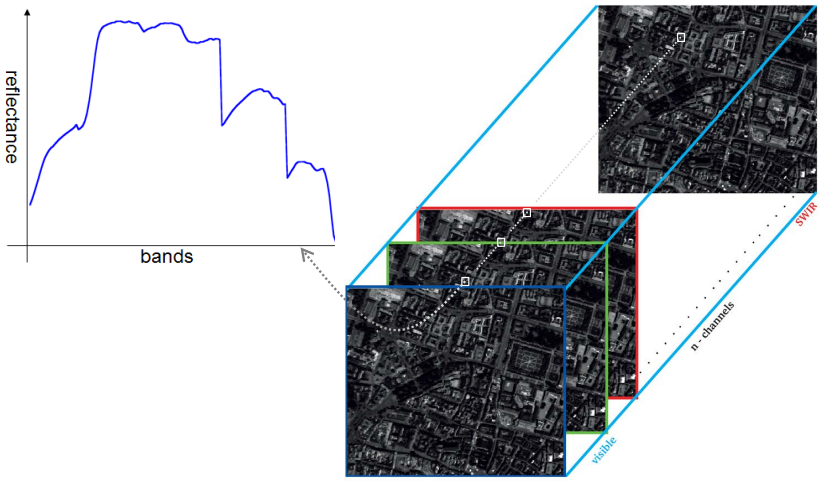

Figure 2.1: Concept of hyperspectral imaging. Hyperspectral images can be represented as a stack of images taken at hundreds narrow adjacent bands over a wide spectral range. As a consequence each spatial pixel from this image can be represented as a reflectance spectrum.

in an image (Figure 2.1). Spectroscopy aims at studying interactions between atoms and molecules, with the electromagnetic spectrum. These interactions can be either absorption, reflection or transmission and can be represented as a function of the wavelength.

2.1.1 Reflectance Spectrum

Reflectance is a unit-less ratio defined as the intensity of the reflected light normalized by the intensity of the incident light (Bachmann, 2007; van der Meer et al., 2001). A function of reflectance at various wavelengths is called *reflectance spectrum*. Opposite to the reflectance spectrum is the *transmittance* spectrum determined by the amount of light transmitted by the surface normalized by the intensity of the incident light. Besides the transmitted and reflected light, some portion is absorbed by a surface. The measure of the light which has been absorbed with relation to the incident light is known as *absorption*. The relation between the transmittance τ_λ, reflectance R_λ, and absorption α_λ can be written as

$$\tau_\lambda + R_\lambda + \alpha_\lambda = 1. \tag{2.1}$$

This relationship is shown in Figure 2.2

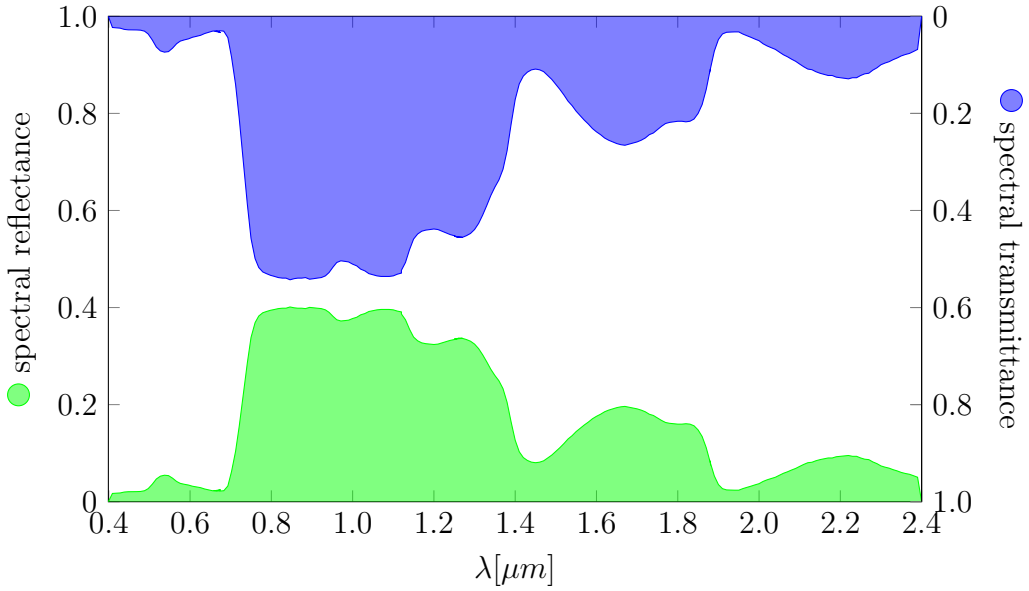

Figure 2.2: Plot of spectral reflectance and transmittance of a green vegetation. The white area between the reflectance and transmittance represents the amount of energy absorbed by the medium.

2.1.2 At-Sensor Radiance Spectrum and Effects of the Atmosphere

Remote sensing optical sensors measure the *at-sensor radiance*, i.e., the quantity of the radiation incident on the sensor. This radiation is composed of the radiation reflected from the Earth's surface plus the influences of the atmosphere. The gases and aerosols contained in the atmosphere interact with the light modifying its energy. Thus, the at-sensor radiance L_s is dependent on the reflectance of the surface as well as atmospheric effects as follows

$$L_s = R\frac{\tau_\phi}{\pi}\varepsilon_G + L_p \quad [Wm^{-2}\mathrm{sr}^{-1}], \tag{2.2}$$

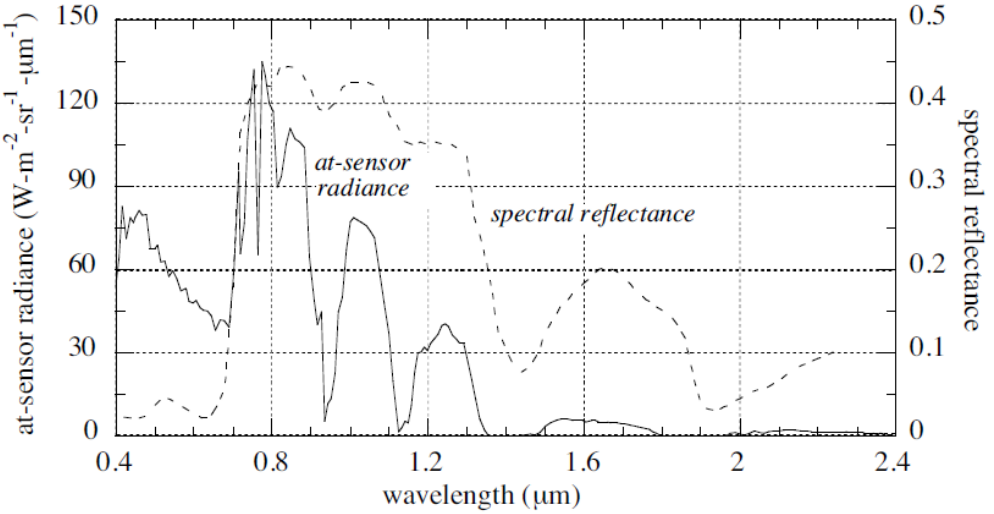

Figure 2.3: Comparison or radiance and reflectance spectrum of grass. The shape of the radiance spectrum is strongly influenced by the absorption features from the atmosphere (from Schowengerdt, 2006, p. 57).

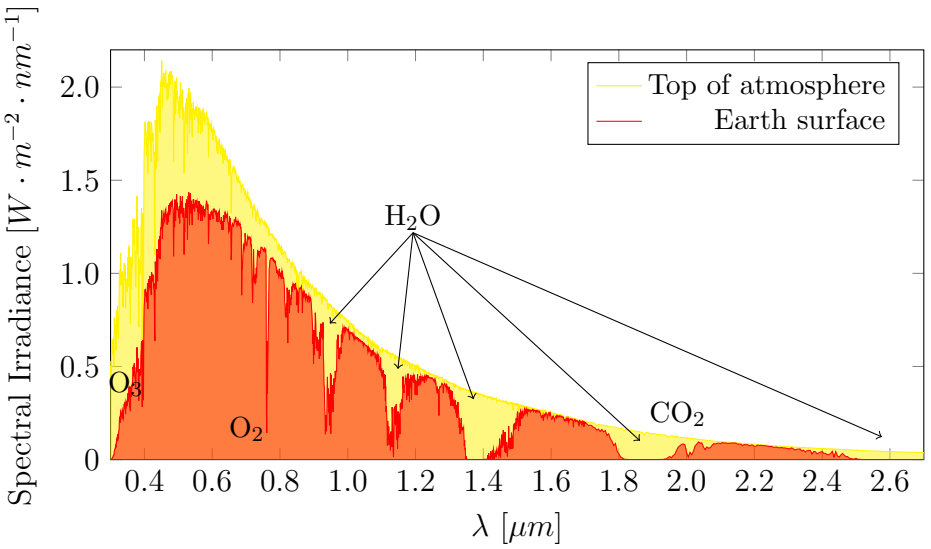

Figure 2.4: Solar irradiance at top of atmosphere and at sea level. The irradiance at the Earth's surface contains many absorption features caused by the gases in the atmosphere.

with the *irradiance* at the Earth's surface (Figure 2.4) ε_G defined as

$$\varepsilon_G(\lambda) = \varepsilon(\lambda)\tau_\theta \cos\phi\tau_\theta(\lambda) + \varepsilon_D(\lambda) \tag{2.3}$$

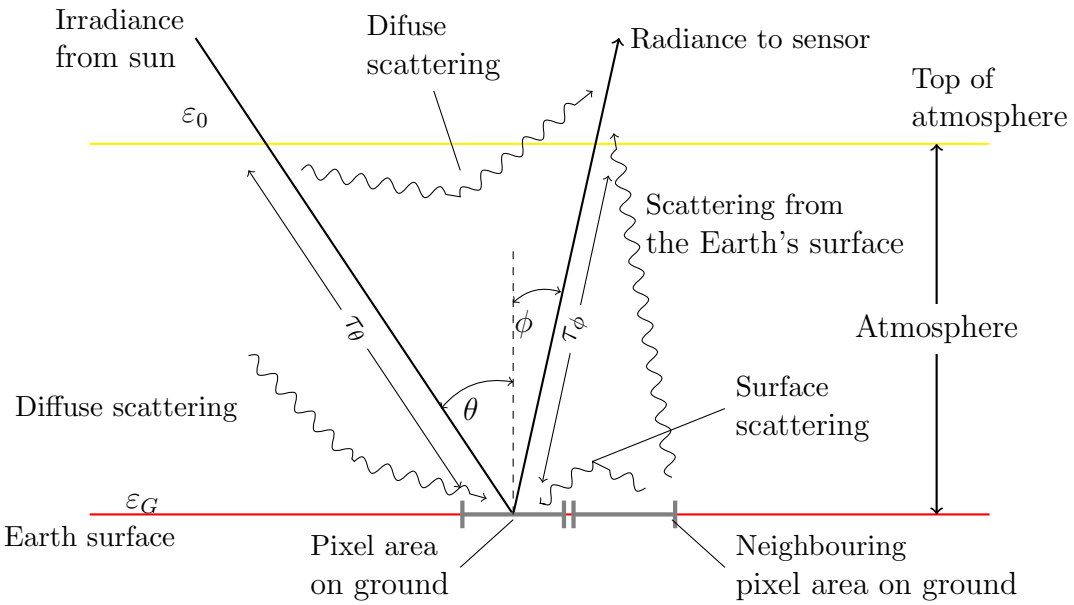

Figure 2.5: A schema of the effects in the atmosphere determining the at-sensor radiance. Remote sensing optical sensor receives energy reflected from the Earth's surface. This energy is determined by the atmospheric transmittance as well as interactions like diffuse scattering, surface scattering, scattering from the Earth's surface or diffuse scattering. (Modified from Richards and Jia, 1999, p. 28)

where

- R is the reflectance
- L_p indicates the *path radiance*, which is an additional radiation that can reach the sensor by either scattering from the Earth's surface or diffuse scattering of incoming light.
- τ_ϕ is the *atmospheric transmittance* between the surface reflection point and the sensor and
- *atmospheric transmittance* τ_θ between the source and the reflection point with angles respectively ϕ and θ.
- the average spectral irradiance $\varepsilon_{\Delta\lambda}$ in the channel and the
- *sky irradiance* ε_D caused similarly by the diffuse scattering and surface scattering.

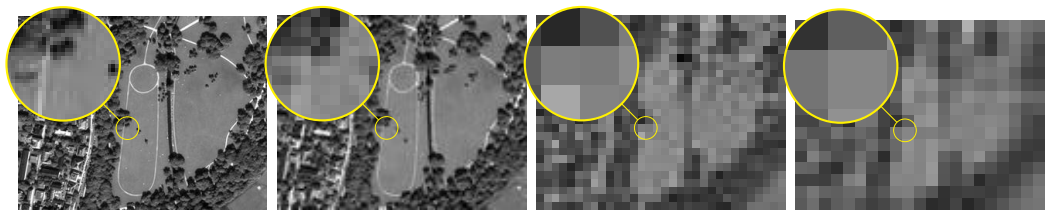

a) GSD = 2m b) GSD = 5m c) GSD = 20m d) GSD = 30m

Figure 2.6: Comparison of different GSDs. The GSD shown in a) and b) are in typical range for spaceborne multispectral sensors. c) and d) exhibit the GSD of modern hyperspectral spaceborne sensors.

A schema of these effects is illustrated in Figure 2.5. The influences of the atmosphere can be seen directly in the at-sensor radiance spectrum when compared to the reflectance spectrum. The characteristic features of the reflectance curve are often masked and modified by the atmospheric transmittance, sky irradiance and path radiance (for e.g. see Figure 2.3).

In order to retrieve the reflectance spectrum from the at-sensor radiance an inverse processing of the equation (2.2) including the modelling of the atmospheric effects has to be done. This type of processing is known as *atmospheric correction*. The discussion of the atmospheric correction methods can be found in Datt et al., 2003; van der Meer et al., 2001, p. 279-281; Richter and Schläpfer, 2011; Schowengerdt, 2006, p. 337-341.

2.2 Spatial Versus Spectral Resolution

The *resolution* of a sensor can be defined as the smallest quantity which can be measured by the sensor. The resolution of the sensor is often determined by its design properties. In the following section the spectral and spatial resolution properties will be discussed.

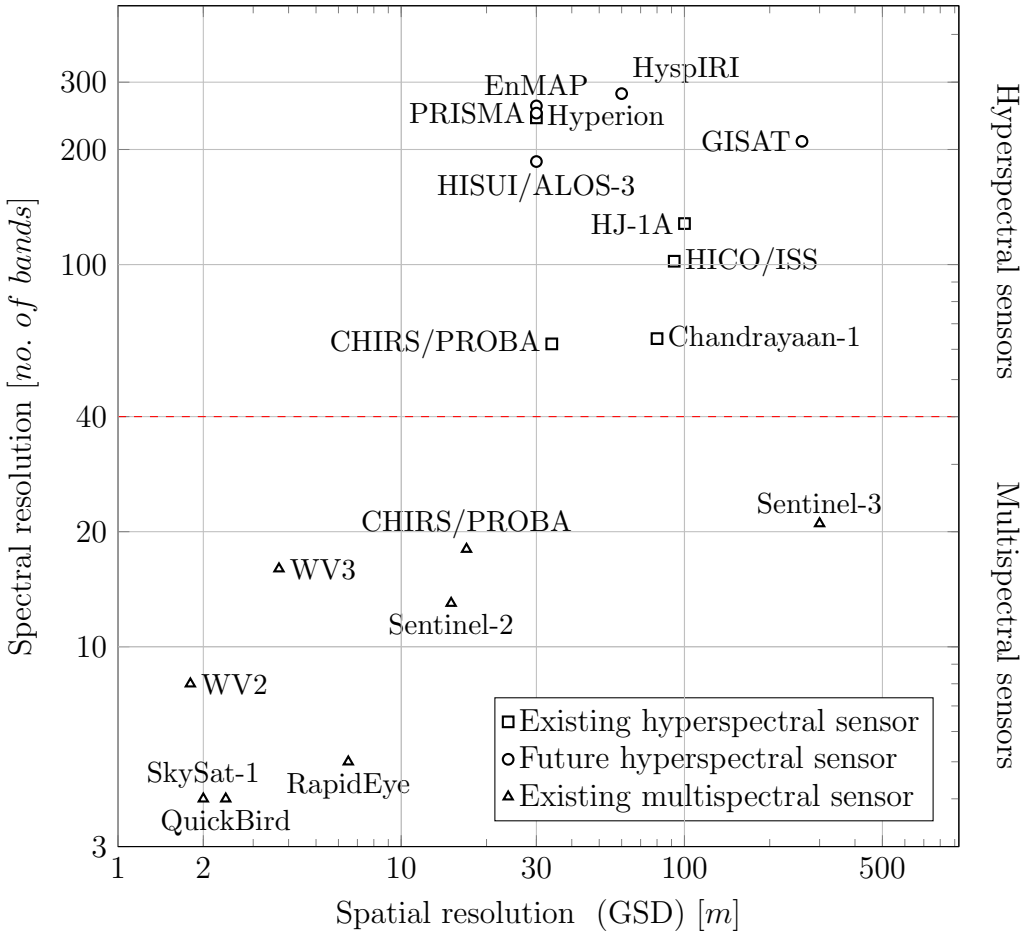

Figure 2.7: Comparison of the spatial and spectral resolution of current and future space-borne hyperspectral and multispectral satellite missions. Red dashed line indicates the conventional border of the spectral resolution between the hyperspectral and multispectral sensors.

2.2.1 Spatial Resolution

Spatial resolution is defined as the smallest structure/detail that can be recognized in the image (Gonzalez and Woods, 2001, p.57-62). The spatial resolution in the hyperspectral image is limited by the the number and spatial distribution of the sensor elements as well as the geometry of the sensor. Additionally, the spatial resolution depends of the contrast of the imaged object and the sum of all blurring effects and distortions of the imaging system. For airborne or spaceborne sensors these effects are a function of

sensor altitude, detector size, focal length and system configuration (Wang and Weng, 2013, p. 12-13). In remote sensing the spatial resolution is often related to the GSD. The GSD is measured as a distance on ground between the centres of two neighbouring pixels. Thus it gives the intuitive relation of the resolution and the distance on the Earth's surface. Images with different GSD are shown in Figure 2.6 .

2.2.2 Spectral Resolution

Similarly to the spatial, *spectral resolution* defines the ability to resolve features in the spectrum. The increase of the spectral resolution results in the reduction of the spatial resolution and vice versa. This is simply caused by the limited amount of the incoming light which has to be split in order to feed hundreds of spectral bands. So that the the average radiance at spectral band λ is

$$L_{\Delta\lambda} \propto \frac{L_s}{K} \tag{2.4}$$

where K stands for the number of spectral bands (Shaw and Burke, 2003). Higher spectral resolution of the sensor helps to resolve fine features in the spectrum e.g. absorption features of materials (Figure 2.8). The comparison of the spatial and spectral resolution for current and planned sensors is presented in the Figure 2.7.

2.2.3 Spectral Response Function

Specification of multispectral and hyperspectral sensors determining the spectral resolution are the width, the height and the central wavelength of the spectral channel. These values define the wavelength range in which the channel responds to incoming photons as well as the spectral separation of the spectral bands. This response can be defined more precisely measuring the sensor's light detection efficiency at a specific wavelength, i.e., the signals *SRF*. The SRF is especially important for re-sampling of spectra needed for comparison of spectral properties in between sensors as well as for the image simulation. The SRF is usually given as a number of electron counts per unit

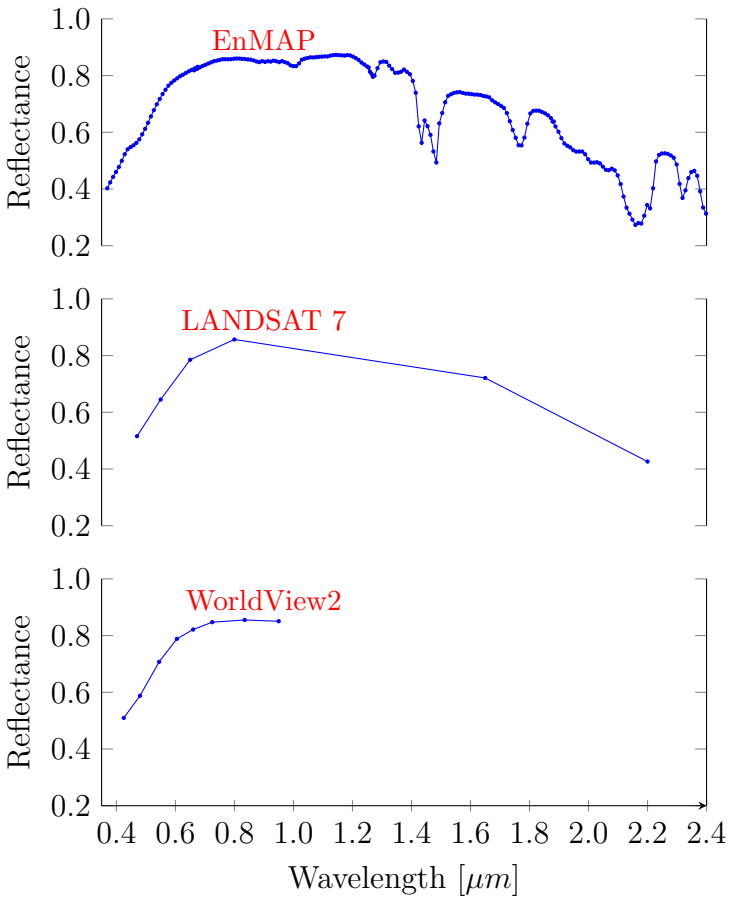

Figure 2.8: Comparison of the spectral resolution between selected sensors. Alunite spectrum plotted with different spectral resolution of two hyperspectral (AVIRIS and HyMAP) and two multispectral (LANDSAT 7 and WorldView 2) sensors. Blue dots correspond to the centers of bands for these sensors.

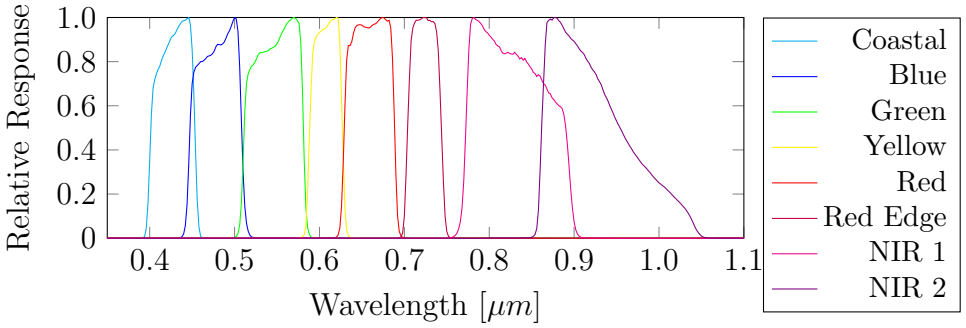

Figure 2.9: Measured SRF of eight bands of the WV2 multispectral spaceborne sensor.

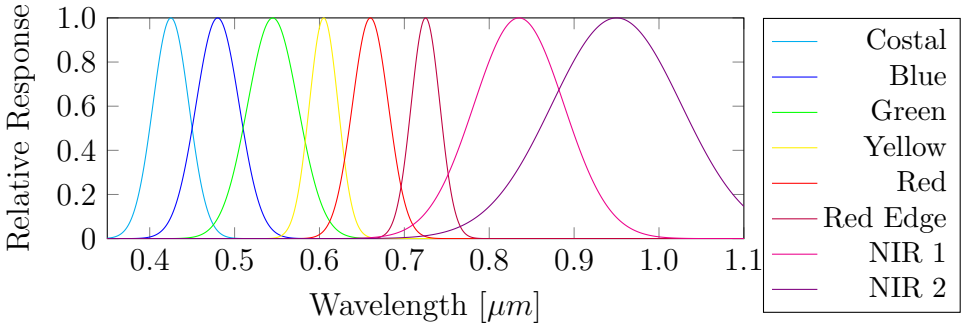

Figure 2.10: Simulated Gaussian SRF of the WV2 multispectral sensor using the given band center and standard deviation in the sensor specifications.

radiance ($\mathrm{mW} \cdot \mathrm{cm}^{-2} \cdot \mathrm{nm}^{-1} \cdot \mathrm{sr}^{-1}$) or its normalized version. The measured SRF for WorldView2 multispectral sensor is illustrated in Figure 2.9.

Sometimes the measured SRF of the sensor for a specific spectral band is not known. In such case it can be modelled with a Gaussian function

$$R_i(\lambda) = \frac{1}{\sigma\sqrt{2\pi}} e^{-\frac{(\lambda-\mu)^2}{2\sigma^2}}, \tag{2.5}$$

where λ is the wavelength from the continues range, μ is the band center wavelength and sigma is a standard deviation of that band. This simulation however, as it can be seen in Figure 2.10 it often deviates from the real SRF (Figure 2.10).

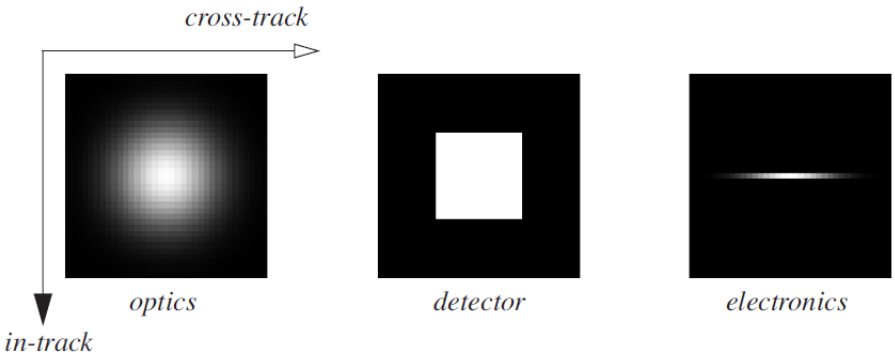

Figure 2.11: The PSF components of the Landsat satellite with 30m GSD. (from Gonzalez and Woods, 2001, p. 94).

2.2.4 Response of a sensor to a Point Spread Function

An example of Point Spread Function (PSF) is shown in Figure 2.11.

The blurring effects and distortions which determine the spatial resolution (see Section 2.2.1) are characterized by the PSF. Similarly to the SRF, the PSF describes the *spatial response function* of the sensor to the input signal. The PSF of an optical remote sensing instrument includes

- *optical* PSF_{opt} defined as the 2-D response of the imaging system to a point-source. It can be measured but often it is modelled as a 2-D Gaussian

$$\text{PSF}_{opt}(x, y) = \frac{1}{2\pi ab} e^{-x^2/a^2} e^{-y^2/a^2} \tag{2.6}$$

  where (x, y) are the spatial coordinates, a and b are the cross and long track widths,

- *image motion* PSF_{motion} modelling the movement of the image across the detector during acquisition. If the motion is in one direction the image motion PSF is modelled by a square pulse in this direction,

- *detector* $\text{PSF}_{detector}$ dependent from the shape and the area of the detector. It is usually modelled as a square pulse function,

- and *electronics* $\text{PSF}_{electronics}$, the blurring caused by the electronic components of the instrument. It also contains the additional filter-

ing sometimes introduced in order to reduce the noise (Gonzalez and Woods, 2001, p. 86-90).

Summarizing, the PSF of an image is given by

$$\text{PSF} = \text{PSF}_{opt} + \text{PSF}_{motion} + \text{PSF}_{detector} + \text{PSF}_{electronics} \tag{2.7}$$

2.2.5 Spectral Re-Sampling and Image Simulation

Each band of a lower spectral resolution image can be simulated from a higher spectral resolution image using

$$L_i = \frac{\int_{\lambda_1}^{\lambda_2} R_i(\lambda) L(\lambda) d\lambda}{\int_{\lambda_1}^{\lambda_2} R_i(\lambda) d\lambda}, \tag{2.8}$$

where L_i is a ith band of the lower resolution sensor, $R(\lambda)$ measured spectral response of band i and $L(\lambda)$ is a measured radiance or reflectance with the higher spectral resolution instrument (van der Meer et al., 2001, p. 41-44). An example of re-sampled spectra from higher to lower spectral resolution is shown in the Figure 2.6. Spatial re-sampling is usually done by interpolation of the neighbouring pixels in order to achieve the desired final GSD. The review of and comparison of resampling methods can be found in Schowengerdt, 2006, p. 300-308; Segl et al., 2010 and van der Meer et al., 2001, p. 41-44.

Similarly, the higher spatial resolution image can be degraded using the PSF of the lower resolution image. That spatial convolution function can be written as

$$s'(x, y) = \int_{\alpha_{min}}^{\alpha_{max}} \int_{\beta_{min}}^{\beta_{max}} s(\alpha, \beta) \text{PSF}(x - \alpha, y - \beta) d\alpha d\beta \tag{2.9}$$

where s' is the signal of the new lower resolution image with spatial coordinates in (x, y) and s is the signal of the higher resolution image with spatial coordinates in (α, β).

2.2.6 Signal-to-Noise-Ratio

Noise is defined as any unwanted signal contaminating the signal of interest. It is usually introduced into the image by the sensor and can occur in a very wide variety of types and models (Cerra et al., 2014; Chang and Du, 2004; Chen and Qian, 2011; Schowengerdt, 2006, 140-152). The discussion of the noise types is beyond the scope of this thesis. However, this section provides an overview of the methods of noise description and measurement.

The Signal-to-Noise-Ratio (SNR) is one of the mostly used quality measures of hyperspectral images as well as one of the crucial sensor parameters. There is no single SNR definition and it changes with application. In order to be meaningful, the ratio should be chosen taking in to account,

- the signal type which can be either at-sensor radiance or reflectance,
- different types of noise contamination (e.g. Gaussian, salt-and-pepper or quantization noise),
- the method for SNR estimation,
- and the ratio type (amplitude or power).

Generally the SNR in a digital image can be defined as

$$SNR_{amplitude} = \frac{p_{signal}}{p_{noise}} \tag{2.10}$$

where p_{signal} is the number of counted signal electrons and p_{noise} is the number of the noise electrons. The signal electrons can be estimated as follows

$$p_{signal} = A_\theta \Omega t_i \int_{\lambda_1}^{\lambda_2} \eta(\lambda) T(\lambda) \frac{\lambda}{hc} L_s(\lambda) d\lambda \tag{2.11}$$

where A_θ is the area of the sensor optics, Ω the field of view, t_i dwell time, $\eta(\lambda)$ is the quantisation and $T(\lambda)$ is the transmission of the sensor optics. Similarly the number of noise electrons is estimated as

$$p_{noise} = \sqrt{N_{sh}^2 + N_i^2} = \sqrt{p_{signal} + N_i^2} \tag{2.12}$$

where N_{sh} is the shot noise and N_i noise of the instrument. The above definition is common in image processing and is referred to as amplitude ratio SNR.

In signal processing the SNR is commonly defined ratio of signal and noise power.

$$SNR_p = \frac{p^2_{signal}}{p^2_{noise}}. \tag{2.13}$$

Both amplitude and power SNR can be expressed in decibels (dB),

$$SNR_{dB} = 10log_{10}(SNR), \tag{2.14}$$

where log_{10} stands for the common logarithm. Since the separation of signal and signal noise in the sensor is not possible, there exist several methods to estimate SNR in the image.

The common "laboratory method" for the SNR estimation is to take an image of a bright surface, compute the ratio between a mean μ_{band} and the standard deviation σ of all pixels in one spectral band

$$SNR = \frac{\mu_{band}}{\sigma_{band}} \tag{2.15}$$

Similarly the SNR can be calculated out of an image from a uniform region or locally for example in a sliding window. Because the standard deviation in this case is not only dependent from the noise but also from the variations in the window, it tends to inflate the SNR. Another method is estimation of the noise from the dark current measurement. This method however, since the dark current is only one component of the noise, tends to deflate the SNR (Schowengerdt, 2006, p. 147-149; van der Meer et al., 2001, p. 35,37).

An example of an image contaminated with random Gaussian noise of different SNR is shown in Figure 2.13.

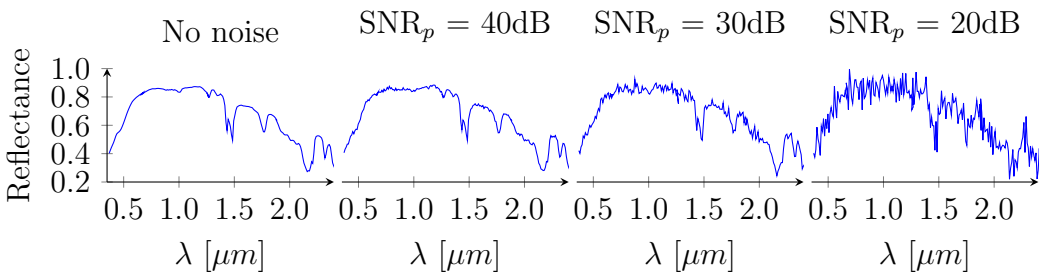

Figure 2.12: Alunite reflectance spectrum without noise and with added random noise given by different noise levels.

2.3 Spectrum of Materials

The fine spectral resolution of hyperspectral images enables tracking even smallest changes and features in the reflectance spectrum. This property allows to study the reflectance spectra in a similar way like it is done in spectroscopy. Based on the fact that each material has its own unique spectral signature it allows recognition of these materials and use in applications like mineral mapping, target detection or classification. However, unlike in laboratory based spectroscopy one can not assure the measured spectrum comes from only one *pure* material. Therefore, while studying hyperspectral reflectance spectra, the fact that these spectra might consist of a mixture of reflectance from different materials appearing in the pixel should be taken into account. In this section the spectral mixing as well as some basic definitions and concepts to deal with this problem will be discussed.

2.3.1 Spectral Mixing Model

The relatively low GSD of hyperspectral images, acquired from airborne of spaceborne platform, results usually in contribution of more than only one material spectrum in one measured spatial pixel. This means that in this pixel a mixture of spectra is recorded and the process is usually referred to as *spectral mixing*. Spectral mixing in most of the cases can be modelled as a linear system of equations

$$y_j = Ax_j, \tag{2.16}$$

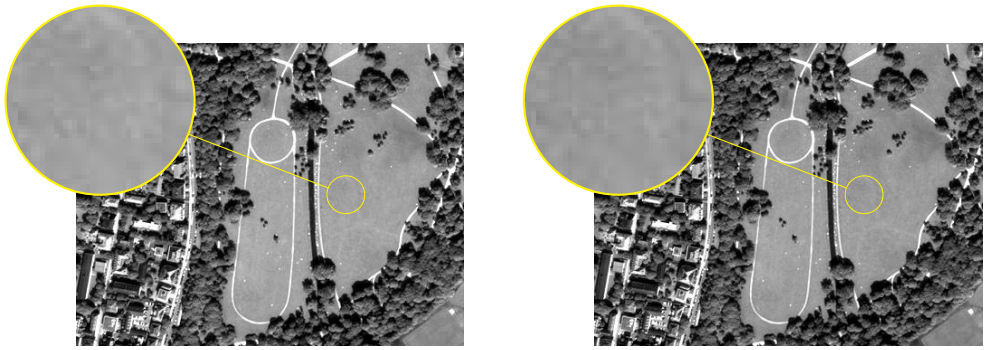

a) $\mathrm{SNR}_p \approx 0$ b) $\mathrm{SNR}_p \approx 40\mathrm{dB}$

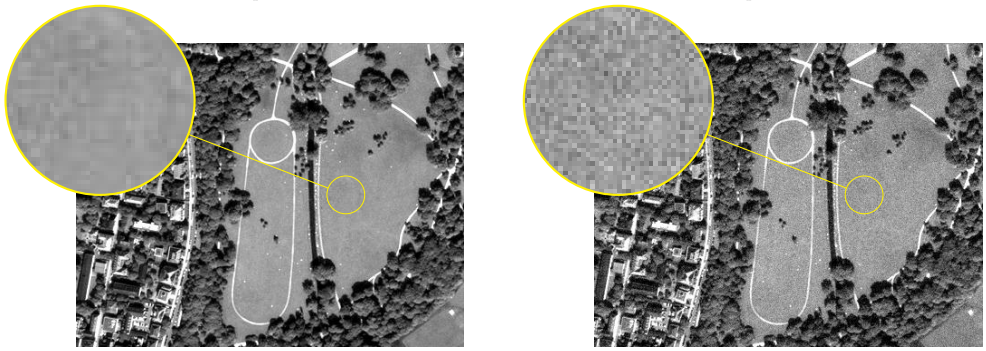

c) $\mathrm{SNR}_p \approx 30\mathrm{dB}$ d) $\mathrm{SNR}_p \approx 20\mathrm{dB}$

Figure 2.13: Comparison of spatial effects caused by additive Gaussian noise with different SNR level. The SNR ≈ 0 is achieved by filtering and down-sampling the original image with GSD = 0.2m to GSD = 2m.

where $y_j \in \mathbb{R}^m$ stands for the measured spectrum from the jth hyperspectral pixel with m spectral bands, $A \in \mathbb{R}^{[m \times n]}$ is the mixing matrix containing n unique linearly independent spectra and $x_j \in \mathbb{R}^n$ is a vector representing proportions of each element from A in the pixel y_j. This model equation (2.16) for pixel synthesis represents the linear mixing model (LMM) (Bioucas-Dias et al., 2013; Drake et al., 1999; Horwitz et al., 1971; Keshava, 2003; Keshava and Mustard, 2002). In other words, the LMM states that the radiance measured by the sensor can be represented as the integrated sum of the spectral radiance of all objects within the captured pixel. Wherein, the proportions of the a_i spectra for each ith material is in linear relation to the geometric proportions in the pixel

$$y_j = \sum_{i=1}^{n} a_i x_{j_i} \text{ where } x_{j_i} \propto \frac{\text{area}(a_i)}{\text{GSD}_{y_j}^2}. \tag{2.17}$$

Based on the above considerations, the proportions vector x_j satisfies the following positivity and sum to one constrains

$$\begin{cases} x_{j_i} \geqslant 0, \ \forall i = 1, \cdots, n, \\ \sum_{i=1}^{n} x_{j_i} = 1. \end{cases} \tag{2.18}$$

Although, most of the mixing process is linear, a fraction of radiance received by the hyperspectral sensor might have undergone a nonlinear mixing. While the linear mixing occurs at sensor the nonlinear mixing is usually caused by physical interactions of the incident light e.g. multiple scattering at either macroscopic level [Figure 2.14 e)] or microscopic level [Figure 2.14 f)] (Bioucas-Dias et al., 2013; Halimi et al., 2011; Heylen et al., 2011b; Keshava, 2003; Keshava and Mustard, 2002; Yokoya et al., 2014).

2.3.2 Spectral Endmember

Until now we have referred to the unique, linearly independent material spectrum as a final element of the mixing matrix in the LMM. This assumption is sufficient for understanding of basic concepts, need to be specified for fur-

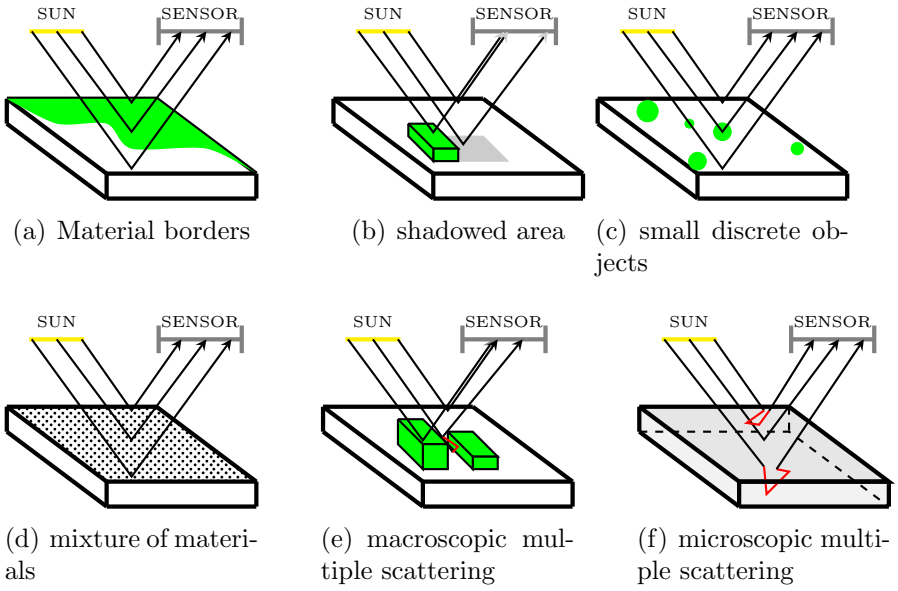

(a) Material borders (b) shadowed area (c) small discrete objects

(d) mixture of materials (e) macroscopic multiple scattering (f) microscopic multiple scattering

Figure 2.14: Possible mixing scenarios

ther consideration of this thesis. For this purpose we introduce the concept of *spectral endmember*. Spectral endmember is assumed to represent pure material at macroscopic level and varies depending on applications (Bioucas-Dias et al., 2013; Halimi et al., 2011; Heylen et al., 2011b; Keshava, 2003; Keshava and Mustard, 2002; Ma et al., 2014). In this section we present two points of view for endmember namely physical and geometrical.

Physical Approach - Material Endmember

Despite the fact that a material endmember is uniform at macroscopic scale, it can sometimes consist of other materials or chemical elements from which each separately can have its unique spectral features. The size of the macroscopic scale is highly dependent on the application and sometimes a definition of soil endmember will be sufficient, whereas in other case, a division to clay, sand, sill and loan or even consisting minerals and moisture levels might be necessary.

The spectra of endmembers are usually measured using spectrometer, in

the laboratory or in the field, and converted to the reflectance spectra. A collection of spectral endmembers are called *spectral libraries*.

Signal Processing Approach - Data Cloud

Each hyperspectral pixel consists of m spectral bands, this means that the pixel y_j can be considered as a vector in m-dimensional Euclidean space. All the hyperspectral pixels build a m dimensional *data cloud*. Taking into account the constrains from the equation (2.18) all vectors x_j will build a simplex hence the data cloud spans all pixels, y_j will be a simplex too. The geometrical definition of an endmember assumes that the *pure* spectra or endmembers occupy extremities of the m dimensional, i.e., vertices of the data cloud simplex (Keshava and Mustard, 2002; Nascimento and Dias, 2005). The graphical interpretation of that concept using real data is shown in the Figure 2.15.

2.4 Introduction to Spectral Unmixing

The method for recovery of endmembers and estimation of their amount for each pixel is called spectral unmixing. Recently, spectral unmixing is intensively studied by many researchers resulting in diverse methods where the endmembers can be retrieved from the image in the manner of geometrical approaches (vertex component analysis - VCA, pixel purity index - PPI, N-FINDR, iterative error analysis - IEA), statistical approaches (independent component analysis ICA-EA) (Bioucas-Dias and Plaza, 2011) or manual selection from existing databases of endmembers or the image itself.

The next step of the spectral unmixing is estimation of the abundance of each endmember in each hyperspectral pixel. Common approaches for abundance estimation include the method of OLS, NNLS (Keshava and Mustard, 2002) and Fully-Constrained Least Squares (FCLS) (Heinz and Chein-I-Chang, 2001). While NNLS ensures the nonnegativity of the abundances, FCLS additionally enforces that the elements of the abundance vector sum to one. Yet, these techniques are dedicated for overdetermined mixing models

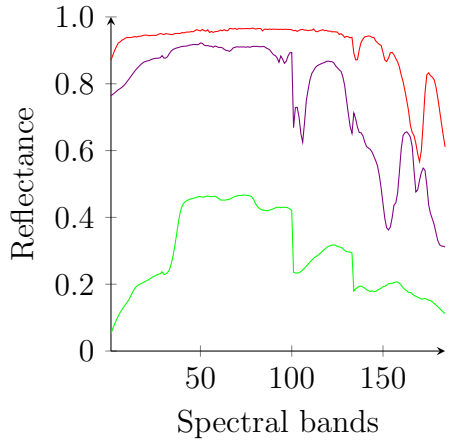

a) Endmembers.

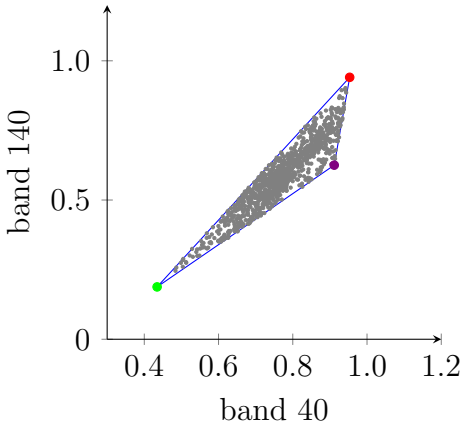

b) Simulated data cloud without noise.

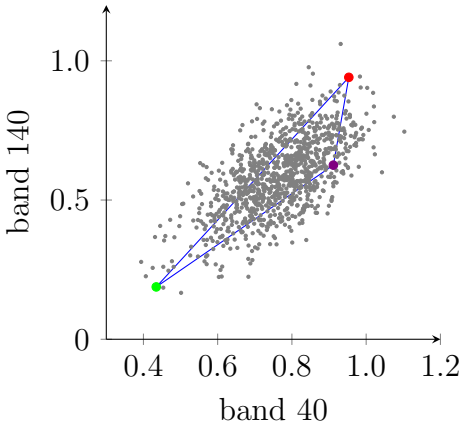

c) Simulated data cloud with added random noise (SNR_p=20dB).

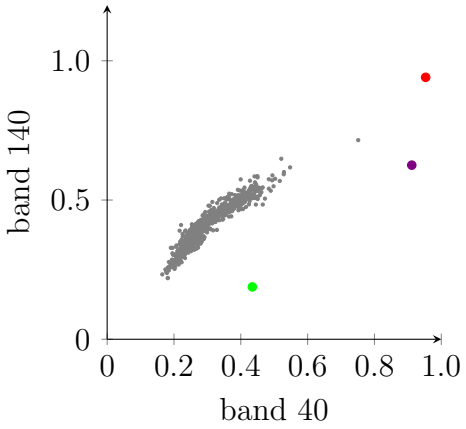

d) spectra from the library (colored points) compared to real image data cloud containing those minerals

Figure 2.15: Examples of three endmember mixtures (—●— alunite, —●— Calcite and —●— dry grass). In sub-plots (b), (c) and (d) the pixel values from bands 40 and 140 (labeled as ·) are plotted. The vertices of the mixing simplex are labeled as (——).

that require a pre-selection of endmembers from a spectral library based on *a priori* knowledge or retrieving them from the image directly (Bioucas-Dias et al., 2012). As a consequence, the amount of allowable endmembers is severely limited. The unmixing methods will be discussed more extensively in Chapter 4.

2.5 Summary

The following issues have been discussed in this chapter.

- Remote sensing hyperspectral sensors are capable of imaging the Earth's surface reflectance with very high *spectral resolution*, i.e., hundreds contiguous, few nanometres-wide bands, in a relatively wide spectral range. In general, the increase of spectral causes the decrease in the spatial resolution.
- The resolutions are determined also by the design properties of the sensor. E.g. the spectral resolution is closely related to the SRF of the sensor, i.e., the wavelength range and the sensitivity of the sensor to incoming photons. An important factor influencing spatial resolution is the PSF characterizing the blurring effects and spatial distortions.
- Images are always contaminated with different type of noise. SNR is the most common way of expressing the noise level in image processing. However, the definition of SNR depends upon the application, in this thesis we will consider the power SNR expressed in decibels.
- The spectrum recorded by the single pixel is, due to the resolution limitations, seldom coming from a single unique material. This means that it most likely contains a mixture of spectra from different materials. The process of retrieving the amount of the constituent materials is known as *spectral unmixing* and will be further studied in this thesis.

After presenting the above introductory concepts of hyperspectral imaging, in the next chapter, we will discuss the theoretical backgrounds for concepts of estimation methods used in this thesis to solve the unmixing problem.

3

Sparse Approximation – The *Magic* Method

The core of the methods developed in this thesis is based on the approximation of object properties from indirect measurements. As introduced in the previous chapter, the pixels in hyperspectral images usually consist of a mixture of reflectance spectra of materials linked to the area of the pixel fraction on ground. The spectral unmixing method aims at recovery of the amount of the spectra using the hyperspectral image data and the set of the endmembers. This approach is usually done by approximation methods. In this chapter first the basic concepts and nomenclature will be given next, general methods with examples of algorithms will be discussed, finally a modification of these methods will be presented.

3.1 Basic Concepts

3.1.1 Linear Model for Inverse Problems

The inverse problem aims to find the information about the observed object $x \in \mathbb{R}^m$ based on indirect measurement $y \in \mathbb{R}^n$ of that object. A general model for the inverse problem can be written as

$$y = \mathcal{T}\{x\} + \varepsilon \tag{3.1}$$

where $\tau : \mathbb{R}^n \longrightarrow \mathbb{R}^m$ is a known operator and ε is the residual vector often related to the additive noise. In case of a *linear model*, the operator will be a matrix $A \in \mathbb{R}^{n \times m}$

$$y = Ax + \varepsilon \tag{3.2}$$

If A has more rows than columns ($n > m$) and is full-ranked, such a system of equation is *overdetermined*. Otherwise, if A has more columns than rows ($m > n$) the model (3.2) is called *underdetermined*.

An example of a linear model is the LMM and inverse problem to this linear model is *spectral unmixing* (see section 2.4). This concept will be extended in the next chapter.

3.1.2 What is Sparsity?

A signal $y \in \mathbb{R}^n$ is $k-$sparse when the support

$$supp(y) = \{i \in [1, n] \mid y(i) \neq 0\} \tag{3.3}$$

is of cardinality $k \ll n$, i.e., only few k elements are non zero elements. Often, when the signal y is not sparse, one can find a linear representation $y = Ax$ where the vector x is sparse.

3.1.3 What is a Vector *Norm*?

A vector's b ℓ_p-norm can be defined as

$$\|b\|_p = \sqrt[p]{\sum_i |b_i|^p}, \tag{3.4}$$

where $p \in \mathbb{R}$. The most commonly used norm is the ℓ_2 norm ($\|\cdot\|_2$) known as the euclidean norm. The ℓ_2-norm is simply a length of the vector b. Whereas the ℓ_1 norm, known as the *Manhattan* norm, is simply a sum of all elements absolute values. A special case in the family of norms is the *pseudo* ℓ_0-norm. Since it is not possible to take a zero-root the *pseudo* ℓ_0 is considered to be

$$\|b\|_0 = \lim_{p\to 0} \|b\|_p^p = \lim_{p\to 0} \sum_k |x_k|^p = \#\{i : x_i \neq 0\} \tag{3.5}$$

ℓ_0 and ℓ_1 norms are recently gaining special attention in the engineering fields due to their *sparsifying* properties. This properties and its application will be discussed in the following sections.

3.2 Solving Linear System of Equations

In this section methods for solving inverse problems using different approaches for data approximation are discussed.

3.2.1 Ordinary Least Squares

An overrdetermined linear system of equations usually does not have a unique solution or has no solution at all and $Ax \neq y$ for all x. Therefore, instead of calculating x an *approximate* $\hat{x}$ has to be found. The most common way of approximating $\hat{x}$ is by finding the minimum Residual Sum of Squares (RSS)

$$RSS(x) = \sum r^2 = \sum (y - Ax) = \|y - Ax\|_2^2 \tag{3.6}$$

and accordingly

$$\hat{x}_{OLS} = \text{argmin } \|y - Ax\|_2^2 \tag{3.7}$$

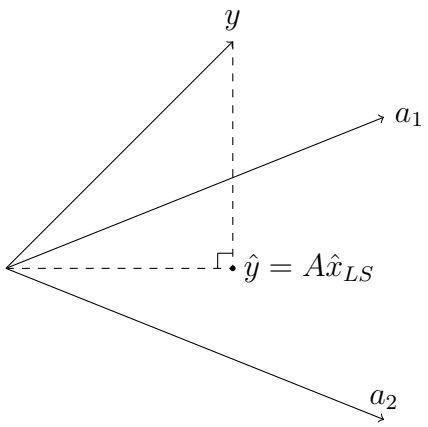

Figure 3.1: Geometrical interpretation of OLS. Estimated $\hat{y}$ is a projection of y onto the plane spanned by A with columns a_1 and a_2.

which is usually referred to as OLS. It can be geometrically interpreted as finding such $\hat{x}$ for which $RSS(x)$ will be orthogonal to each column of A

$$A^T(y - A\hat{x}_{OLS}) = 0 \Rightarrow \hat{x}_{OLS} = (A^T A)^{-1} A^T y \tag{3.8}$$

i.e. the distance between vector y and estimated vector $\hat{y} = A\hat{x}$ will be the smallest Figure 3.1. Note, that the equation (3.8) can compute the solution only when the $A^T A$ is invertible. Additionally, when the system of equations is underdetermined equation (3.8) will not find unique solution. Therefore, it is common to use the Minimum-Norm Solution (MNS)

$$\hat{x}_{MNS} = \text{argmin } \|x\|_2 \text{ subject to (s. t.) } y = Ax \tag{3.9}$$

which can be calculated using the Moore-Penrose pseudo inverse

$$\hat{x}_{MNS} = A^T(AA^T)^{-1} y. \tag{3.10}$$

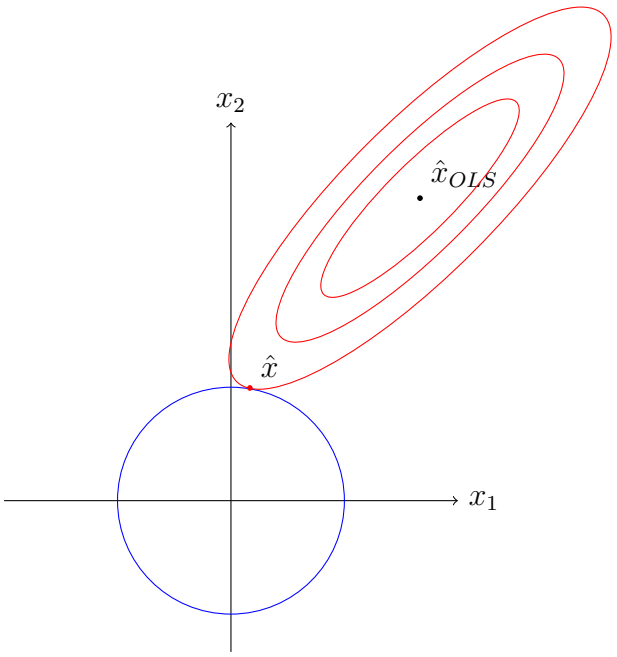

Figure 3.2: Geometrical interpretation of the ridge regression. The blue circle represents the ℓ_2 norm of the vector x. The $\hat{x}_{OLS}$ is the OLS solution and $\hat{x}$ is the solution to the ridge regression.

3.2.2 ℓ_2 Norm Regularization

The OLS and MNS will always try to find the best representation of y in sense of the smallest RSS. This means that in the presence of noise in y the OLS will approximate the signal and the noise instead of just the observed object x e.g. *overfit* the data. Even small amount of noise in the data might lead to large errors in the estimation. This instability phenomena is called *ill-posedness* (Vogel, 2002, p. 1-24).

This problem can be addressed by the ridge regression, also known as Tikhonov regularization. Here the least squares term is *regularized* by the length of the estimated vector x. The geometrical interpretation of ridge regression is shown Figure 3.2. This minimization problem can be written in general form as

$$min\|Ax - y\|_2^2 + \lambda\|x\|_2^2 \tag{3.11}$$

where λ is the penalty parameter. That means that for a specific setting of

λ a solution with upper bound δ will be promoted

$$min\|Ax - y\|_2^2 \text{ s.t. } \|x\|_2 \leq \delta. \tag{3.12}$$

where small bound δ corresponds to large penalty λ and vice versa. In order to solve this minimization problem a minor modification to equation (3.8) has to be done

$$\hat{x}_{ridge} = A^T(AA^T + \lambda I)^{-1}y \tag{3.13}$$

where I is the identity matrix. One can easily observe that if $\lambda = 0$ this equation becomes OLS, for $\lambda = \infty$, $\hat{x}_{ridge} = 0$ and for $\lambda = \langle 0, \infty \rangle$ the linear model y on A is balanced with the shrinking of $\hat{x}$.

3.2.3 ℓ_0 Norm Regularization

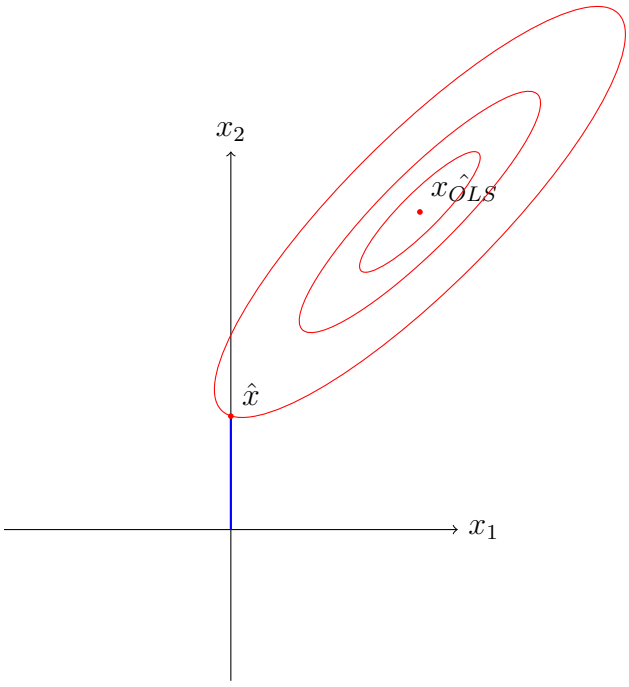

Figure 3.3: Geometrical interpretation of the ℓ_0 norm regularization. The blue line represents the ℓ_0 norm of the vector x. The $\hat{x}_{OLS}$ is the OLS solution and $\hat{x}$ is the solution to the ridge regression.

The previous method promotes solutions with restricted length of $\hat{x}$ and

even though for $\lambda \to \infty,\ \hat{x} \to 0$ the elements $\hat{x}$ will shrink towards zero but will not be set to zero. Therefore, in case when x is expected to be sparse, the ℓ_0 norm can be used as a regularizer

$$min\|Ax - y\|_2^2 + \lambda\|x\|_0. \tag{3.14}$$

The geometrical interpretation of the sparsity promoting property of this formulation is shown in (Figure 3.3). Similarly like in ridge regression an alternative equivalent formulation can be written

$$min\|Ax - y\|_2^2 \text{ s.t. } \|x\|_0 \leq \delta_0 \tag{3.15}$$

where δ_0 sets the limit on the number of non-zero elements in the vector x. If the sparsity of x is not known the minimization problem can be reformulated to be constrained by the upper bound ε on the RSS, often related to noise

$$min\|x\|_0 \text{ s.t. } \|Ax - y\|_2^2 \leq \varepsilon. \tag{3.16}$$

Because the $\|x\|_0$ term is *non-convex* it is a typical example of a combinatorial search problem. Such problems are very hard to solve (Baraniuk, 2007; Baraniuk et al., 2008; Candes and Wakin, 2008). For example consider a matrix $A \in \mathbb{R}^{n \times m}$ is of size $n = 200$ and $m = 300$ and we suppose that the sparsest solution has $k = 10$ non-zeros we have to go through $\binom{n}{k} \approx 1.4 \times 10^{18}$ combinations of $y = A_k x_k$. If the calculation of a single $y = A_k x_k$ would take only 10^{-9} second, to find a complete set of possible combinations it would take 556 days to compute x (Elad, 2010, p. 13-14).

Algorithm 1: OMP (Orthogonal Matching Pursuit)

Input: A, y, δ_0, ϵ

begin
  initialize: set all $\hat{x}_{j,\dots,m} = 0$, $\mathcal{V} = \varnothing$,$r = y$;
  for i = *1,...,*δ_0 **do**
    calculate correlation vector $\hat{c} = A^T r$;
    update active set with the greatest current correlation $\mathcal{V} = \{j : |c_j| = max(|\hat{c}_j|)\}$;
    get a subset matrix $A_\mathcal{V} = (\cdots s_j a_j \cdots)$, where $s_j = \text{sign}\{|c_j|\}$ for $j \in \mathcal{V}$;
    update the coefficient vector x and the residual r $\hat{x} \longleftarrow (A_V^T A_V)^{-1} A_V^T y,\ r \longleftarrow (y - A_V \hat{x})$;
    if *if* $\|r\|_2^2 \leq \epsilon$ **then**
      return $\hat{x}$
    ;
return $\hat{x}$;

Due to the inefficiency of the combinatorial search, another option to find the solution to problem (3.15) is to use the greedy search algorithm. However, this is proofed to work only if the the equation (3.2) fulfils several requirements (for example see Donoho and Elad, 2003; Elad, 2010, p. 65-71; Gribonval and Nielsen, 2003). Additionally, due to the *hard thresholding* the algorithm tends to select local minima to the final solution (Murphy, 2012, p. 429-430). To illustrate this problem lets consider one of the most established algorithms for sparse recovery based on greedy search - OMP. The OMP algorithm can recover a $k-$sparse solution in only k iterations. This is possible because it selects one column from A which is the most correlated with the residual r at each iteration and adds it to the set of active columns $\mathcal{V}$. Subsequently the solution $\hat{x}$ is updated solving the OLS using so constructed $A_\mathcal{V}$ and calculating a new residual r for the next iteration. For details refer to the pseudo code in Algorithm 1. The OMP algorithm can solve the problem (3.15) by setting δ and problem (3.16) if the ϵ is set. If

both parameters are set the OMP will iterate until one of the conditions is met. This type of discrete selection recovers the exact support of x. However, OMP has been reported to have strong limitation on the properties of A. As an example the high correlation among columns in A leads to the solution instability, i.e., the OMP might at first *pick up* a wrong column and later due to the hard thresholding this failure can not be corrected. This drawback should especially be considered when y is noisy.

3.2.4 ℓ_1 Norm Regularization

It has been shown that an alternative method for finding sparse approximation of x is to regularize the RSS by penalizing the ℓ_1 norm of this vector

$$min\frac{1}{2}\|Ax - y\|_2^2 + \lambda\|x\|_1 \tag{3.17}$$

This type of regularization is known as Basis Pursuit Denoising (BPDN) (Chen et al., 1998). The advantage of this approach is the substitution of the non-convex, discrete term of $\|x\|_0$ (Figure 3.3) with the convex and continuous term of $\|\cdot\|_1$ (Figure 3.4). The equation (3.17) can be equivalently expressed with its constrained version written as

$$min\|Ax - y\|_2^2 \text{ s.t. } \|x\|_1 \leq \delta_1 \tag{3.18}$$

where δ is upper bound on the ℓ_1 norm of the vector x. This formulation, more popular in the statistical community, is known as the Least Absolute Shrinkage and Selection Operator (LASSO) (Tibshirani, 1996).

The sparsity promoting property of the ℓ_1 norm can be explained comparing Figure 3.4 with Figure 3.2. The optimal solution for these functions can be found at the intersection point of the constraint surface and the objective function (Murphy, 2012, p. 430-431). One of the most popular choices in solving the (3.18) problem is the LARS/LASSO algorithm (Efron et al., 2004). The principle of the algorithm is similar to the OMP algorithm. Both start with x set to zero and at each step select column from A most correlated with the residual r and add it to the set of active columns $\mathcal{V}$. The

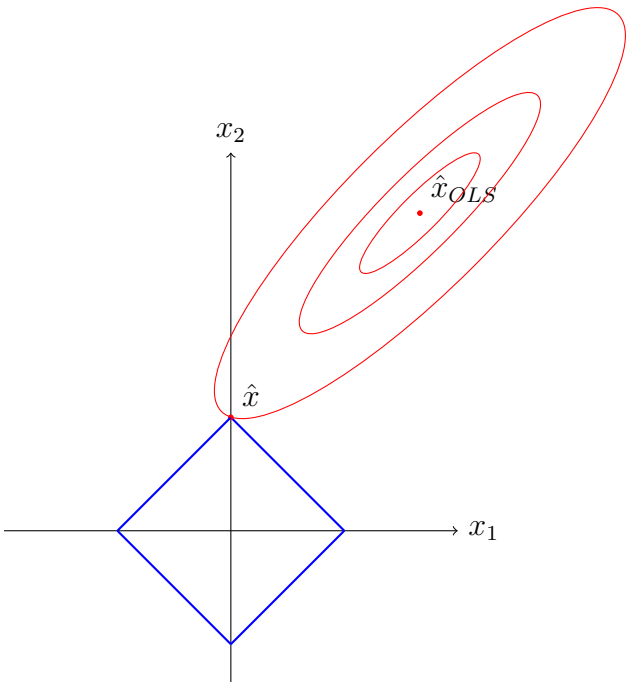

Figure 3.4: Geometrical interpretation of the ℓ_1 norm regularization. The blue square represents the ℓ_1 norm of the vector x. The $\hat{x}_{OLS}$ is the OLS solution and $\hat{x}$ is the solution to the ridge regression.

main difference between both algorithms is the way of updating the solution $\hat{x}$. While OMP computes the new solution with the new set of active columns (hard thresholding), the LARS/LASSO updates the coefficient vector $\hat{x}$ with the largest possible step size until some other column in A has the most correlation with the current residual. Then the algorithm proceeds in the equiangular direction for all active columns until the next column will became most correlated (soft thresholding). For more details please refer to Algorithm 2 or to Efron et al. (2004); Tibshirani (1996).

3.3 Non-negativity Constraint

The regularization problems can be further extended with the constrains tailored according to the *a priori* knowledge about the data model. Spectral unmixing requires the coefficient vector x to be non-negative (Keshava, 2003;

Algorithm 2: LARS/LASSO (Least Angle Regression LASSO)

Input: A, y, δ_1

begin

initialize: set all $\hat{x}_{j,\dots,m} = 0$, $\mathcal{V} = \varnothing$,$\mathcal{V}^c = \varnothing$, $r = y$;

while $\|x\|_1 \leq \delta_1$ **do**

calculate correlation vector $\hat{c} = A^T r$;

update active set with the greatest current correlation

$$\hat{C} = max|\hat{c}_j| \text{ and } \mathcal{V} = \{j : |c_j| = \hat{C}\} \tag{3.19}$$

;

get a subset matrix $A_\mathcal{V} = (\cdots s_j a_j \cdots)$, where $s_j = \text{sign}\{c_j\}$ for $j \in \mathcal{V}$;

compute equiangular vector $y_\mathcal{V}$ and the inner product vector d

$$y_\mathcal{V} = A_\mathcal{V}\omega_\mathcal{V},\ d = A^T y_\mathcal{V} \tag{3.20}$$

where $\omega_\mathcal{V} = X_\mathcal{V}\mathcal{G}_\mathcal{V}^{-1}1_\mathcal{V},\ \mathcal{G}_\mathcal{V} = A_\mathcal{V}^T A_\mathcal{V}$ and $X_\mathcal{V} = (1_\mathcal{V}^T\mathcal{G}^{-1}1_\mathcal{V})^{\frac{1}{2}}$;

compute the step size

$$\hat{\gamma} = \min^+_{j\in\mathcal{V}^c}\left\{\frac{\hat{C} - \hat{c}_j}{X_\mathcal{V} - d_j}, \frac{\hat{C} + \hat{c}_j}{X_\mathcal{V} - d_j}\right\} \tag{3.21}$$

check for the sign violation;

$\tilde{\gamma} = \min^+\{\gamma_j\}$ where $\gamma_j = -\hat{x}_j/k_j,\ k_j = s_j\omega_{\mathcal{V}j}$ for $j \in \mathcal{V}$;

if $\tilde{\gamma} < \hat{\gamma}$ **then**

change $\hat{\gamma} = \tilde{\gamma}$;

remove $\tilde{j} = \text{argmin}^+\{\gamma_j\}$ for $j \in \mathcal{V}$ from the set $\mathcal{V}$;

update the coefficient vector x and the residual r

$$\hat{x} \longleftarrow \hat{x} + \hat{\gamma}d,\ r \longleftarrow (y - A_\mathcal{V}^T\hat{x}) \tag{3.22}$$

;

return $\hat{x}$;

Keshava and Mustard, 2002; Nielsen, 2001). The minimisation objective with this constrain can be formulated as

$$\hat{x}_{NNLS} = \text{argmin } \|y - Ax\|_2^2 \; s.t. \; x \geqslant 0 \tag{3.23}$$

This quadratic programming problem can be solved using the NNLS algorithm (Bro and De Jong, 1997; Lawson and Hanson, 1974, p. 160-165). In essence the NNLS algorithm iteratively estimates coefficient vector by calculating the solution using only positive elements from the least squares estimation until the desired tolerance is met. However, the need of calculating OLS at each iteration increases the computation time significantly. Unlike OLS, NNLS under certain conditions (detailed discussion for the sparse recovery with NNLS will be provided in the next chapter) can guarantee the uniqueness of the solution for underdetermined system of equation and can provide sparse solution (Meinshausen, 2013).

Similarly, the non-negativity is often imposed on the sparse regularizes ($\ell_0,\ \ell_1$). The ℓ_0 regularized minimization with the non-negativity prior can be formulated as

$$min\|Ax - y\|_2^2 + \lambda\|x\|_0 \; s.t. \; x \geqslant 0 \tag{3.24}$$

This problem can be solved after slight modification of the OMP Algorithm (Algorithm 3) (Bruckstein et al., 2008).

In order to solve the non-negative Basis Pursuit Denoising (nBPDN)

$$min\|Ax - y\|_2^2 + \lambda\|x\|_1 \; s.t. \; x \geqslant 0 \tag{3.25}$$

with the LARS/LASSO algorithm (Algorithm 2) a minor modifications has to be done. First, change $|\hat{c}_j|$ to $\hat{c}_j$ in (3.20). Next, in step 6 set $s_j = 1$.

Algorithm 3: NOMP(Non-Negative Orthogonal Matching Pursuit)

Input: A, y, δ_0, ϵ

begin
  initialize: set all $\hat{x}_{j,\ldots,m} = 0$, $\mathcal{V} = \varnothing$,$r = y$;
  for i = *1,...,*δ_0 **do**
    calculate the following error for all $1 \leq j \leq m$,
    $\hat{\epsilon} = \min_{x_j \geq 0} \|a_j x_j - r\|_2^2 = \|r\|_2^2 - \frac{\max\{a_j^T r, 0\}}{\|a_j\|_2^2}$;
    update active set such $\mathcal{V} = \{j : \epsilon_j = min(\hat{\epsilon}_j)\}$;
    get a subset matrix $A_{\mathcal{V}} = (\cdots s_j a_j \cdots)$, where $s_j = \text{sign}\{|\epsilon_j|\}$ for $j \in \mathcal{V}$;
    update the coefficient vector x and the residual r
    $\hat{x} \longleftarrow min\|Ax - y\|_2^2 \; s.t. \; x \geqslant 0, \; r \longleftarrow (y - A_V \hat{x})$;
    if *if* $\|x\|_2^2 \leq \epsilon$ **then**
      return $\hat{x}$
    ;
return $\hat{x}$;

Finally, change the equation (3.21) to

$$\hat{\gamma} = \min_{j \in \mathcal{V}^c}^{+} \left\{ \frac{\hat{C} - \hat{c}_j}{X_{\mathcal{V}} - d_j} \right\} \tag{3.26}$$

Unlike in the NNLS algorithm the change made in the LARS/LASSO or OMP algorithm does not increase the complexity of the algorithm and the same does not increase the computation time.

3.4 Joint Sparsity

Most methods for sparse recovery are addressed to approximate scalar functions. However, often in signal and image processing applications there are hundreds of such functions to be approximated. This is the case in e.g spectral unmixing where the mixture has to be approximated for each pixel in the image. Sometimes these signals are correlated and more importantly, the linear models for the inverse problem are correlated too. In case when this correlation results in common support in the approximated vector x one

could think of joint approximation of these signals.

Suppose there exist J number of linear systems equations $y_i = Ax_i$ where $i \in 1, ..., J$ and all y_i share a portion of the information. If the measurements y_i share some information then we can imply that each coefficient vectors x_i will share a portion of the support. Based on these assumptions a model for jointly sparse signals can be formulated as

$$Y = \tilde{A}X \tag{3.27}$$

where

$$Y = \begin{bmatrix} y_1 \\ y_2 \\ y_3 \\ \vdots \\ y_J \end{bmatrix} \tag{3.28}$$

is a vector ensemble for joint signals $y_1, ...y_J$, and

$$\tilde{A} = \begin{bmatrix} A & A & \mathbf{0} & \mathbf{0} & \cdots & \mathbf{0} \\ A & \mathbf{0} & A & \mathbf{0} & \cdots & \mathbf{0} \\ A & \mathbf{0} & \mathbf{0} & A & \cdots & \mathbf{0} \\ \vdots & \vdots & \vdots & \vdots & \ddots & \vdots \\ A & \mathbf{0} & \mathbf{0} & \mathbf{0} & \cdots & A \end{bmatrix} \tag{3.29}$$

is a matrix containing copies of the matrix A and $\mathbf{0}$ matrix of same size as A, with all elements equal to zero. Then the ensemble coefficient vector can be written as

$$X = \begin{bmatrix} x_c \\ x'_1 \\ x'_2 \\ \vdots \\ x'_J \end{bmatrix} \tag{3.30}$$

where the vector x_c contains coefficients common for all j , i.e., having the same support for all j. This is enforced by the design of $\tilde{A}$ where the first

supercolumn (m first columns of $\tilde{A}$) of $\tilde{A}$. Vectors $x'_1, ...x'_j$ contain all *differences* and new elements recovered by *supercolumns* of $\tilde{A}$ containing only one copy of the dictionary A (Baron et al., 2005, 2009).

The concept of joint sparsity with application to spectral unmixing will be further discussed in the next chapter.

3.5 Summary

In this chapter we have discussed the following concepts.

- An approach of finding information about the observed object from its indirect measurements is called *inverse problem*. Often such approaches are modelled as linear system of equations.
- To solve such problems approximation methods are used. All the discussed methods are based on the minimisation of the RSS.
- OLS has been proven to be sensitive to noise in the model. Therefore it of advantage to use regularised approximation methods instead. An example of regularized OLS is the ridge regression. If the regression parameter grows the, approximated vector will shrink towards zero but seldom will not become sparse.
- If the approximated vector is expected to be sparse, ℓ_0 or ℓ_1 regularisation terms can be used.
- ℓ_0 regularisation is a non-convex function but it can be solved using greedy search algorithms like OMP.
- The ℓ_1 regularisation has been reported to be alternative to ℓ_0 regularisation. This approach is less sensitive to correlation of columns in A. An example of algorithm solving ℓ_1 approximation is the LARS/LASSO algorithm.
- Often the approximated vector is constrained to be nonnegative. This constrain transforms the OLS problem to be quadratic what significantly increases the complexity of OLS and BPDN. In contrast, the

introduction of the nonnegativity in the LARS/LASSO algorithm does not increase the complexity of the algorithm.

- The joint sparsity model can be used for approximation of correlated signals where the coefficient vectors are supposed to be sparse and have common support.

Part II

Sparse Spectral Unmixing and Resolution Enhancement

4

Sparse Spectral Unmixing

Recent work on hyperspectral image unmixing has addressed the use of overcomplete dictionaries by employing sparse models. In essence, this approach exploits the fact that hyperspectral image pixels can be associated with a small number of constituent pure materials. Sparsity-based techniques do not require endmember extraction or selection step and are thus able to simultaneously estimate the underlying active materials along with their respective abundances. However, sparse approximation methods have been reported to have problems using large spectral dictionary where the coherence between endmembers is high. The problem of sparse unmixing, dictionary coherence as well as reducing the size of the dictionary will be discussed in this chapter. In addition, this perspective will be extended so as to exploit the spatial homogeneity of abundance vectors and an alternative approach that captures both similarities and differences between neighboring abundances will be presented.

4.1 Sparse Spectral Unmixing – The Concept

Spectral unmixing is a method for quantitative analysis of hyperspectral images. This analysis includes detection of *endmembers* and estimation of their *abundance* in each pixel of the hyperspectral image. The usual approach for spectral unmixing is first, to either extract endmembers from the image or to use a preselected set of available known endmembers and second, approximate the abundance using one of the least squares based methods.

Recent work on hyperspectral image unmixing has addressed the use of overcomplete dictionaries by employing sparse models , i.e., *sparse spectral unmixing*. In contrast to conventional methods, this model operates on a very large set of endmembers usually given in advance , i.e., *spectral dictionary*. In essence, this approach exploits the fact that each hyperspectral pixel can be associated with only a small number of constituent pure materials. This implies the use of a *sparsity prior* in the abundance vectors by applying sparse approximation methods.

4.1.1 Sparsity Prior Model

Let us assume a LMM

$$y_j = Ax_j \tag{2.16}$$

where $y_j \in \mathbb{R}^m$ is the measured spectrum from the jth pixel, $A \in \mathbb{R}^{[m \times n]}$ is the mixing matrix containing endmembers and $x_i \in \mathbb{R}^n$ is the abundance vector. When A is overcomplete, i.e., it contains more endmembers than spectral channels $n > m$ or even $n >> m$ one could expect x to be *sparse* (see Figure 4.1). Considering the fact that hyperspectral sensors have usually hundreds of channels and the spatial resolution of up to 30 m, the assumption that x will be sparse is reasonable. This property brings a new look into the unmixing problem where, instead of extracting endmembers from an image or looking for endmembers manually, researchers can use hundreds of predefined endmembers.

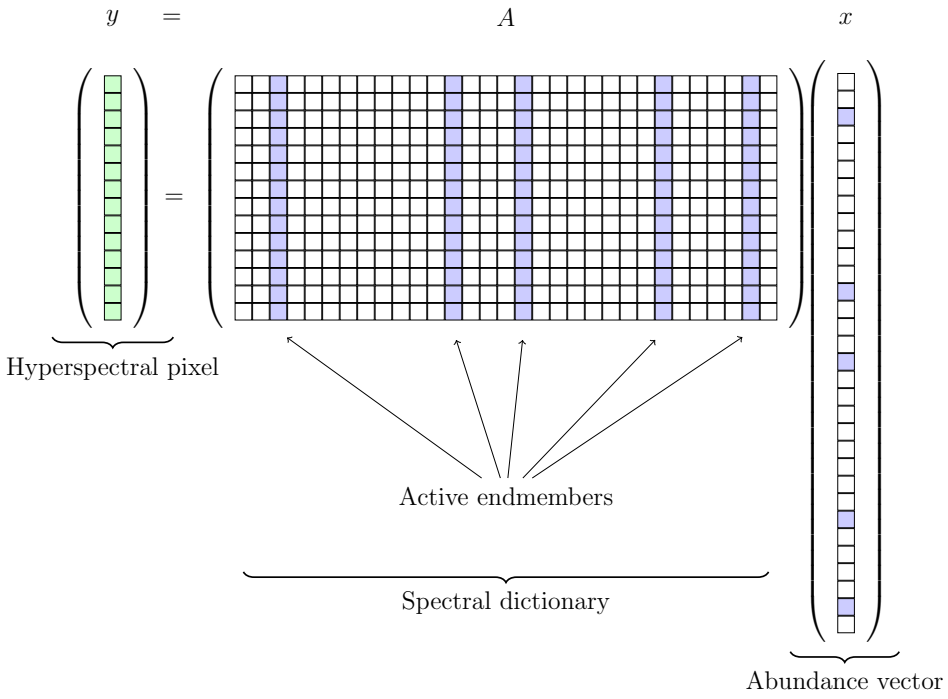

Figure 4.1: Illustration of a mixing model with sparse prior. A hyperspectral pixel can be described as a mixture of only few endmembers from a spectral dictionary weighted by a sparse abundance vector.

4.1.2 Spectral Dictionary

The matrix A containing a large set of different endmembers will be then called the *spectral dictionary*. Spectra in the dictionary can be either a large collection of unique image endmembers or a collection of spectra of materials measured *in-situ* e.g. in laboratory or by hand-hold spectrometers in the field. In this thesis we define a *spectral dictionary* as a set of linearly independent spectra. Note, that the spectral dictionary can contain several measurements of the same material as long as they are not linearly dependent. This is allowed due to the fact that spectra of the same material might differ significantly depending on e.g. water content, age of the material or mineral composition (see for example spectra of Andradite Figure 4.2).

When using spectral dictionaries containing measurements from various sensors under different conditions one should be aware that these measure-

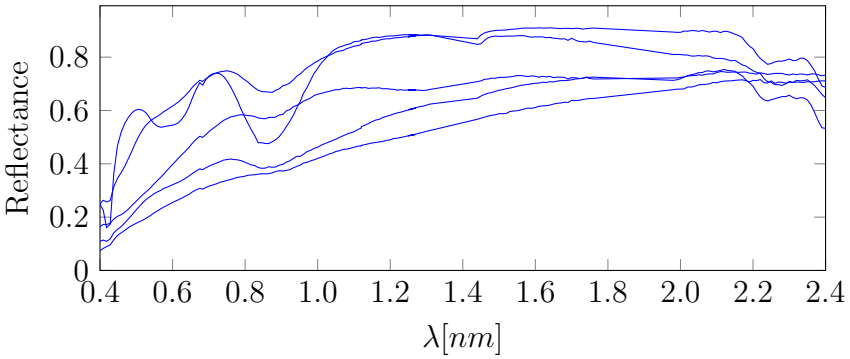

Figure 4.2: Different spectral measurements of the same material - Andradite. Taken from the spectral library *splib06* (Clark et al., 2007).

ments also contain noise. Also, the dictionary might miss some endmembers apearing in the image. As a result the space spanned by column vectors of the dictionary might not obey completely the space spanned by hyperspectral image data. Another case is that the dictionary contains pure spectra of minerals (e.g. Alunite) as well as composites of these minerals (aluminium, potassium and sulphate). Here, sparse approximation is of advantage because it will promote sole spectrum instead of mixture of more spectra.

4.1.3 Abundance Estimation With Sparse Prior

The expected sparsity of the abundance vector implies the use of sparse approximation methods. Hence, the abundance estimation problem can be formulated as the non-negative version of the OMP

$$\min \|Ax - y\|_2^2 \text{ s.t. } \|x\|_0 \leqslant \delta_0 \text{ and } x \geqslant 0 \tag{4.1}$$

where δ_0 is the upper bound set on the number of endmembers in the spectrum y. Alternatively, the sparsity can be controlled using the nLASSO formulation

$$\min \|Ax - y\|_2^2 \text{ s.t. } \|x\|_1 \leqslant \delta_1 \text{ and } x \geqslant 0 \tag{4.2}$$

or equivalent nBPDN

$$\min \frac{1}{2}\|Ax - y\|_2^2 + \lambda \|x\|_1 \text{ s.t. } x \geqslant 0 \tag{4.3}$$

Since the ℓ_1-norm and ℓ_0-norm serves as proxy for sparsity, the penalty parameter δ_0, δ_1 or λ can be used to trade sparsity of the solution for data mismatch. Also, in order to ensure physical validity, the abundance vector is constrained to be nonnegative. Additionally, the formulation 4.2 allows more intuitive control of the minimisation considering sum-to-one property of the spectral abundance. The minimization problem (4.2) is referred to as nBPDN or equivalent nonnegative sparse LASSO (Efron et al., 2004). The probability of reliable sparse unmixing, however, highly depends on the properties of the matrix A and the noise present in the spectrum (Bieniarz et al., 2012; Bioucas-Dias et al., 2012; Iordache et al., 2011, 2013).

Under certain conditions the NNLS is also able to approximate underdetermined systems of equations (Donoho and Tanner, 2005). Additionally, in certain cases NNLS can also recover sparse solution (Greer, 2012). For the sake of explanation lets consider the case in only two dimensions , i.e., A containing 2 endmembers. A measured spectrum y is a mixture of only one endmember a_1 (sparse mixture) and additive noise ϵ. Now, depending on the influence of noise, OLS, NNLS and BPDN can yield different approximations (for example see Figure 4.3).

(i) If ϵ added to y brings it outside the space spanned by A, both NNLS and sparse approximation will recover the sparse solution while OLS will instead compensate the noise by negative values of a_2.

(ii) If ϵ added to y brings it inside the space spanned by A, only sparse approximation will yield sparse solution. The OLS and NNLS will compensate the noise with a_2.

(iii) If y stays on a border of A all algorithms will result in the same approximation.

4.2 Related Work

Spectral unmixing together with abundance estimation is a concept for finding the type and amount of endmembers mixed within a hyperspectral pixel

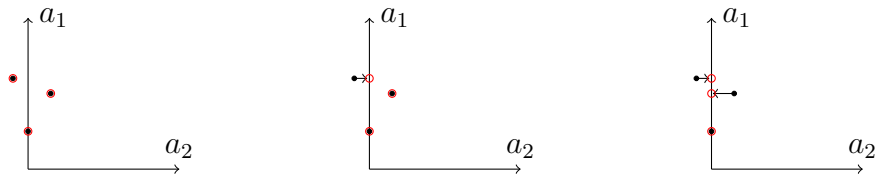

a) OLS b) NNLS c) sparse approximation

Figure 4.3: Geometrical interpretation of sparse solution to the abundance estimation problem. Black dots represent noisy measurements y while red circles are the approximate solutions $\hat{y}$. In this example the noise free y^o is known to lay on a_1.

(Ifarraguerri and Chang, 1999; Keshava and Mustard, 2002). Recently, researchers came up with the idea of exploiting the sparse nature of abundance vectors. In this section both traditional as well as new concepts of sparse unmixing will be discussed.

4.2.1 Non-Sparse-Prior Unmixing

The traditional approach for estimating the abundance of endmembers is to use a matrix A with endmembers extracted from the image and computing the abundance vector by means of the OLS based methods. The first approach to approximate abundance of endmembers was presented in Settle and Drake (1993). In this work the authors additionally constrained the OLS by the *sum-to-one* property of the abundance vector. Other early methods were introduced in Chang et al. (1998); Settle and Drake (1993); Shimabukuro and Smith (1991). However, none of these methods obey the nonnegative nature of abundances. The nonnegativity, instead was imposed by setting negative values to zero what means that these methods actually do not converge to the optimal solution (Heylen et al., 2011a). In order to fulfil the nonnegtivity property of abundances and at the same time obtain an optimal solution Heinz and Chein-I-Chang (2001) used the NNLS algorithm first introduced by (Lawson and Hanson, 1974, p. 165-167). Additionaly, Heinz and Chein-I-Chang (2001) incorporated the sum-to-one constraint in order to obey the physical property of the abundance vector. This algorithm is known as FCLS. Although, the FCLS algorithm converges to the optimal

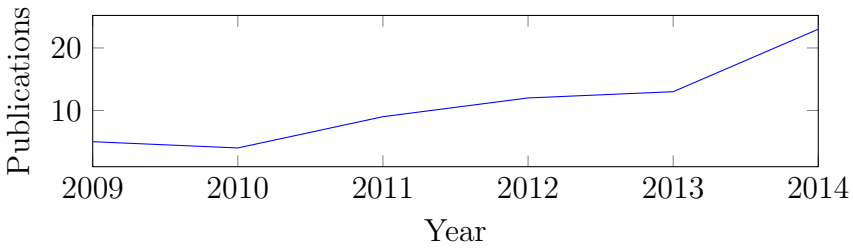

Figure 4.4: Number of publications with keywords: "sparse", "hyperspectral" and "unmixing" by year. The results are from search in IEEEXplore® .

solutions, when the number of endmembers is large or the data are noisy, it tends to overfit the data (Heylen et al., 2011a; Pu et al., 2014). Other recent approaches in abundance estimation include the Bayesian (Dobigeon et al., 2009; Themelis et al., 2012) or nonnegative matrix factorisation (Jia and Qian, 2009; Yang et al., 2011). These algorithms however, extract endmembers from the data and at the same time calculate abundances.

4.2.2 Sparse-Prior Unmixing

Sparse spectral unmixing is recently gaining more attention resulting in an increasing number of publications on that topic (Figure 4.4). The sparsity-based spectral unmixing methods estimate abundances in the presence of overcomplete spectral dictionaries (Bieniarz et al., 2012; Iordache et al., 2011; Tang et al., 2014b). These methods make use of the fact that there are typically only few endmembers inside a pixel (depending on the pixel size) compared to the large endmember spectral library (Iordache et al., 2011), i.e., the abundance vector to be estimated is sparse and has only up to few nonzero elements.

The model for linear unmixing with sparse prior was first proposed in the work of Parente and Zymnis (2005). Authors used a spectral dictionary with 117 endmembers and solved the LASSO problem to estimate the abundance vectors. This idea despite promising results has not been further developed until Guo et al. (2009) and Iordache et al. (2009) again tried to use the sparse regularisation methods for abundance estimation. However, Guo et al. (2009)

applied the ℓ_1 minimisation using only 6 endmembers extracted from the image. Iordache et al. (2009) on the other hand, used 20 simulated spectra from which the mixtures were created. Using these data authors compared application of ℓ_0, ℓ_1, OLS, and iterative spectral analysis (Rogge et al., 2006). Despite the limited experimental part, these works were very significant and brought back the attention to the *sparsity* in hyperspectral unmixing.

In Iordache et al. (2011) following the ideas from their previous paper a new, more comprehensive comparison of applying OMP and BPDN to spectral unmixing was performed. Including its non-negative versions as well as the traditional NNLS and FCLS. To solve the BPDN problem the authors used the newly proposed SUnSAL algorithm dedicated to spectral unmixing from Bioucas-Dias (2009). Additionally for the first time overcomplete dictionaries were used. This work proved the advantage of solving the abundance estimation problem as BPDN over other methods when using large spectral dictionaries. The results however, are highly dependent on the coherence of the dictionary and the fact that the spectra in the dictionary are rarely acquired with the same conditions. These problems lead to errors in the estimation. Additionally, an increase of the computational complexity while using SUnSAL is pointed out.

Some researches tried other approaches also yielding sparse solutions. Themelis et al. (2012), for example, targeted the sparse unmixing problem as a hierarchical Bayesian model incorporating nonnegativity and sum-to-one constraint. The main advantage of these method is that the parameters for the constraint as well as the sparsity parameters are selected by a new Bayesian inference iterative scheme. Chen and Zhang (2013) tested sparse unmixig using several different ℓ_p sparsifying norms where p was in the range $0 < p < 1$. It has been shown that in certain cases this approach yields better results than standard ℓ_1 minimization. However, this optimisation, due to its non-convexity, often gets stuck into suboptimal solutions. Similarly Tang et al. (2014a) used a logarithmic function in order to approximate the ℓ_0 norm.

Iordache et al. (2013) introduced the idea of collaborative sparse unmixing. In this approach, the unmixing is done by minimizing the residual error for all pixels in the image using the $\ell_{2,1}$ mixed norm as regularizer. The mixed

$\ell_{2,1}$ norm promotes sparsity among columns of the abundance matrix while minimizing the energy along the rows, i.e., the algorithm tends to select common endmembers for all pixels in the image. This approach provides good results for homogeneous areas with few active endmembers because the regularization is performed globally. Tang et al. (2015) instead of using $\ell_{2,1}$ mixed norm incorporates an additional regularization term to the unmixing problem in order to enforce the abundance of endmembers known to be present a priori.

The use of large dictionaries for spectral unmixing brings the advantage of omitting the step of endmember extraction from the image. Frankly, its size and especially similarities between spectra sometimes causes problems for the approximation. This, according to Iordache et al. (2012a) and Iordache et al. (2014), can be avoided by pruning the dictionary before applying the sparse approximation methods. The authors propose first to use the HySIME algorithm (Bioucas-Dias and Nascimento, 2008) to estimate the data subspace and select only those spectra from the library which are most correlated with that subspace. This approach improves the unmixing performance as well as reduces the computational complexity. However, since this approach is performed globally, the whole unmixing result is dependent on the initial subspace estimation and pruning step. Tang et al. (2014b) presented a new forward backward algorithm where the dictionary is preselected in a first step by performing forward backward greedy algorithm and then used to calculate abundances with NNLS. The forward backward greedy algorithm in essence performs OMP in one direction and then in similar way like OMP adds spectra to the working set by dropping "unnecessary" spectra in backward direction until the criterion of minimum error is met. Both algorithms (Iordache et al., 2014; Tang et al., 2014b) are highly dependent from the initial spectra preselection. Additionally, in (Tang et al., 2014b) the preselection does not include the nonnegativity constraint.

4.2.3 Spatial-Spectral Unmixing

Methods and algorithms presented in the previous section process either each pixel separately or the whole image at a time concentrating only on the spectral information. However, the information contained in the spatial domain might be valuable for the spectral unmixing process. The incorporation of spatial features in 'traditional' spectral unmixing has been studied by many researchers (see for example Jia and Qian (2007); Plaza et al. (2002) or Canham et al. (2011)).

Recently, the spatial information has been also successfully incorporated in methods using sparse spectral unmixing. Iordache et al. (2012b) in his work assumed that the transition between neighbouring pixels should be smooth. In order to promote the smoothness in the unmixing results an additional regularisation term, so called *total variation* has been incorporated into the sparse optimisation problem

$$min\|AX - Y\|_F^2 + \lambda\|X\|_{1,1} + \lambda_{TV}TV(X)\ s.t\ X \leq 0 \tag{4.4}$$

where F denotes the Frobenius matrix norm, $\|X\|_{1,1} = \sum_{i=1}^{n} \|x_i\|_1$ and

$$TV(X) \equiv \sum_i \sum_{j \in \rho} \|x_i - x_j\|_1 \tag{4.5}$$

with ρ denoting the neighbourhood of the ith pixel. The authors claim that if the parameter $\lambda_{TV} = 0$ the algorithm converges to the BPDN so the minimisation (4.4) can be considered as the BPDN with yet additional regularisation. This approach has been proven to greatly improve the quality of abundance estimation for images with low variations in the spatial distribution of abundances. One of the main drawbacks of this approach is the need of setting an additional parameter which makes the algorithm more complicated in use.

Another way of adding information from surrounding pixel was proposed by Tang et al. (2014b). The authors, additionally to the forward-backward greedy algorithm mentioned in previous section, added the spatial contextual

coherence cost function

$$G(X) = \frac{1}{2} \sum_{i} \sum_{j \in \rho} \|x_i - x_j\|_2^2 W_{ij} \tag{4.6}$$

where W_{ij} weights the similarities between pixels. The function is enforced in the step of solution update. Again, like in the pixel based version of the algorithm, the sparse regularisation as well as the function $G(X)$ are effective in the dictionary preselecion step and the final abundance estimation is done by means of the NNLS algorithm.

4.3 Research Questions

It has been proven that the use of a sparsity prior yields better results when compared to traditional abundance estimation methods, especially when overcomplete spectral dictionaries are used. However, many scientific questions in sparse spectral unmixing are still open, including:

- Researchers observed that the coherence between elements of the dictionary (the concept of *coherence* will be further described in the next section) causes many problems in correct estimation of abundances (Iordache et al., 2011, 2012a, 2014; Tang et al., 2014b). Are all algorithm similarly sensitive to the coherence problem? Can the coherence in the dictionary be reduced and at the same the performance of the estimation increased?

- Many sparse unmixing algorithms suffer from the high computational time due to their high complexity. Most of the algorithms solve quadratic programming problems, although very fast greedy algorithms solving the same optimisation problem exist. Can greedy algorithms perform with similar accuracy as the state of the art unmixing algorithms?

- Approaches for dictionary preselection usually select endmembers globally, i.e., the subspace of endmembers is estimated for the whole hyperspectral image. These approaches are known to be robust to noise,

however they might omit or exclude rare endmembers, present e.g. only in one pixel. Based on this fact, can pixel-based endmember preselection lead to an increase of performance for images with diverse content? Additionally, preselection of endmembers from a coherent spectral dictionary adds uncertainty of the preselection accuracy, which is later propagated to the unmixing result. Is a selection of a whole group of endmembers instead of just one able to increase the endmember estimation accuracy?

- An incorporation of spatial information in the sparse unmixing process has been proven to greatly improve the unmixing results (Iordache et al., 2012a; Tang et al., 2014b). State of the art methods add an additional regularisation term to the minimisation of the cost function which increases the complexity and makes the algorithms less intuitive. This type of regularisation imposes the spatial smoothness to the calculated abundances which might not always be true. Is there another way of exploiting intra pixel similarities and the fact of sharing some endmembers by the neighbouring pixels, without forcing them to be smooth and without introducing yet another cost function?

The following chapter will focus upon answering the above research questions.

4.4 Dictionary Coherence Problem - Derivative Unmixing

4.4.1 Dictionary Coherence

One of the most important condition in sparse approximation methods is the *mutual coherence* of the dictionary A. Mutual coherence is a measure of maximum correlation between pairs of endmembers a_i of the dictionary expressed as

$$\mu = \max_{i \neq j} |\varphi_i^T \varphi_j| \tag{4.7}$$

where $\varphi_i = \frac{a_i}{\|a_i\|_1}$ is the normalised endmember. However, mutual coherence is a worst-case measure and it reflects the most extreme correlations in the dictionary.

There have been numerous theoretical works discussing the stability of the solution recovery of the sparse vector depending from the mutual coherence (Ben-Haim et al., 2010; Cands and Romberg, 2006; Donoho et al., 2006; Elad, 2007; Tropp, 2004). In essence, the smaller the coherence between the endmembers, the better the abundance vector can be approximated using the ℓ_1 or ℓ_0 minimization (Starck et al., 2010). Following Donoho et al. (2006), a stable solution for ℓ_0 minimisation can be guaranteed when the sparsity k of the abundance vector is $k < (\mu^{-1} + 1)/2$. Now, consider the case of using a spectral dictionary containing 224 unique spectra selected from the United States Geological Survey (USGS) spectral library (Clark et al., 2007). The mutual coherence for this dictionary is equal $\mu_{USGS} = 0.999$ what indicates that maximally $k = 1$ sparse solution can have a guaranteed unique solution, i.e., only pure spectra can be approximated. Despite these limitations, the sparse approximation methods have been reported to perform well when used for spectral unmixing (Chen and Zhang, 2013; Guo et al., 2009; Iordache et al., 2012a, 2010, 2009; Parente and Zymnis, 2005; Tang et al., 2014b). However, many authors claimed that the correlated endmembers in the dictionary cause problems in these approaches. In the next section we will discuss a possible way of reducing correlations between endmembers in the dictionary and simultaneously increase the performance of sparse unmixing.

4.4.2 Derivative Method for Coherence Reduction

Derivatives of spectra have been used in spectroscopy for years (Lawson and Hanson, 1974). Applying 1'st, 2'nd or even 3'rd order derivatives helped many researchers in detecting and comparing spectral features and has been used in many applications including identifying plant stress (Smith et al., 2004), landcover classification (Tsai and Philpot, 2002) or even in unmixing for abundance estimation of spectrally similar materials (Debba et al., 2006).

The differentiation of a discrete function estimates the slope over the

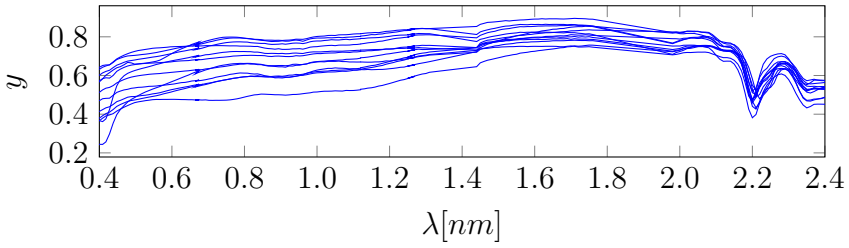

a) Original spectra

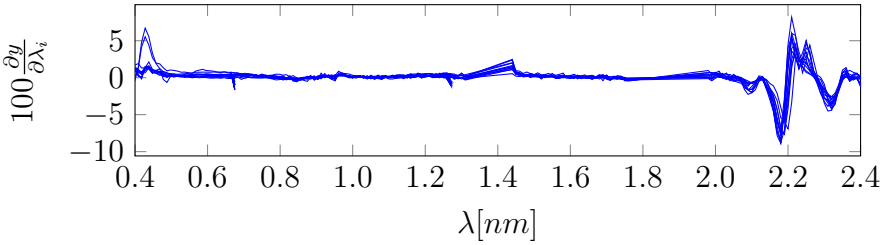

b) Derivative spectra

Figure 4.5: Muscovite spectra selected from spectral library *splib06* (Clark et al., 2007). Although these are spectra of the same material they differ significantly when considering reflectance spectra (a). After applying derivative significant spectral features are easier identifiable (b).

changing independent variable. In case of spectral derivatives the independent variable is the spectral band number. The derivative of a spectrum can be calculated in the following way

$$\frac{\partial y}{\partial \lambda} \approx \frac{y(\lambda_i) - y(\lambda_{i+1})}{\Delta \lambda}, \tag{4.8}$$

where λ_i is the wavelength of a hyperspectral band i. Then $\Delta\lambda = \lambda_i - \lambda_{i+1}$for m spectral bands. The differentiation of spectra does not result in more information contained in the original bands but it decreases background reflectance and can therefore considerably improve the detection of convoluted weaker absorption features (Bieniarz et al., 2012; Talsky, 1994; Tsai and Philpot, 1998). For example see Figure 4.5.

The property of amplifying fine spectral features by the spectral derivative

can be used in reducing coherence in the spectral dictionary. The influence of spectral derivative can be easily explained in the frequency domain. Low frequencies in the reflectance spectrum have usually high amplitude (see Figure 4.6). Applying the derivative equation (4.8) to the reflectance spectrum is equivalent to filtering out low frequencies [Figure 4.6 (b)]. This can be interpreted as removing one common direction from a vector often responsible for correlations between the spectra (for example see Figure 4.5). Applying spectral derivative to the spectral dictionary does not necessary reduce the mutual coherence but it reduces the correlations in the dictionary. For comparison between coherence of spectra and matrices computed for original signal and after applying the derivative refer to Figure 4.7 and Figure 4.8. Also, the amount of highly correlated spectra is significantly reduced using the derivative (Figure 4.9).

The spectral derivative is calculated using a linear operator and therefore can be written in a matrix form as

$$\frac{\partial y}{\partial \lambda} = \mathcal{S}y \tag{4.9}$$

where the spectral derivative operator $\mathcal{S}$ is defined as

$$\mathcal{S} = \begin{bmatrix} \frac{1}{\Delta\lambda_1} & \frac{-1}{\Delta\lambda_1} & 0 & 0 & \cdots & 0 \\ 0 & \frac{1}{\Delta\lambda_2} & \frac{-1}{\Delta\lambda_2} & 0 & \cdots & 0 \\ 0 & 0 & \frac{1}{\Delta\lambda_3} & \frac{-1}{\Delta\lambda_3} & \cdots & 0 \\ \vdots & \vdots & \vdots & \vdots & \ddots & \vdots \\ 0 & 0 & 0 & \cdots & \frac{1}{\Delta\lambda_i} & \frac{-1}{\Delta\lambda_i} \end{bmatrix} \tag{4.10}$$

with $\Delta\lambda$ denoting forward difference operator for band numbers. It is also easy to see that applying the spectral derivative to both sides of LMM equation

$$\mathcal{S}y = \mathcal{S}Ax \tag{4.11}$$

does not change the properties of the abundance vector.

Another advantage of using the mixing model with spectral derivative equation (4.11) is the fact that the derivative reduces the influence of the

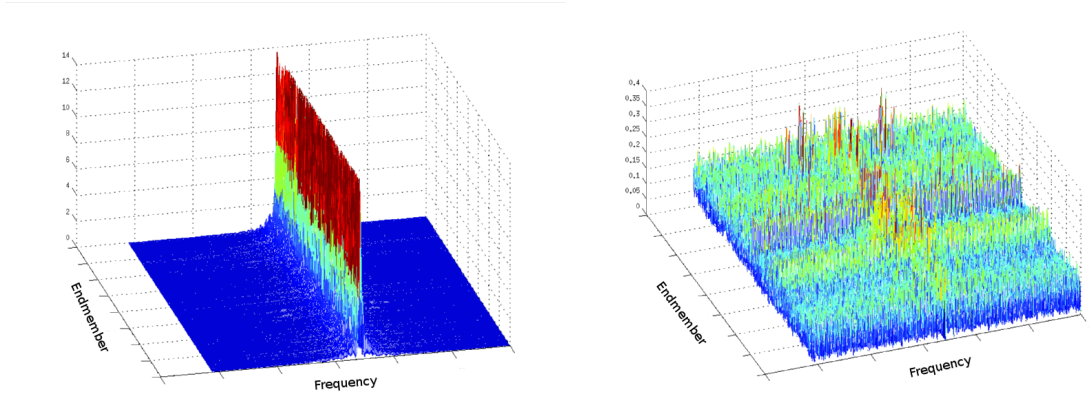

a) Fourier transform of the original USGS Dictionary with 792 spectra and 184 bands

b) Same as a) after derivative transform

Figure 4.6: Comparison of the Fourier transform before and after applying spectral derivative.

illumination conditions (Talsky, 1994). This is especially important when using external dictionaries due to the fact that the consisted spectra were usually collected under different conditions (Clark et al., 2007).

The main drawback in using spectral derivative is their sensitivity to noise. This issue and performance of the derivative unmixing in presence of noise will be shown in the experimental part of the thesis.

4.5 Large Dictionary - Endmember Pre-selection Unmixing

The high mutual similarities between spectra of many materials may lead to unstable solutions. This effect can be reduced by pruning the dictionary. Pruning is usually done by selecting the most reliable endmembers from a redundant dictionary before performing actual abundance estimation (Iordache et al., 2014; Tang et al., 2014b). However, one should note that selecting endmembers from a dictionary e.g. those the most correlated with the data does

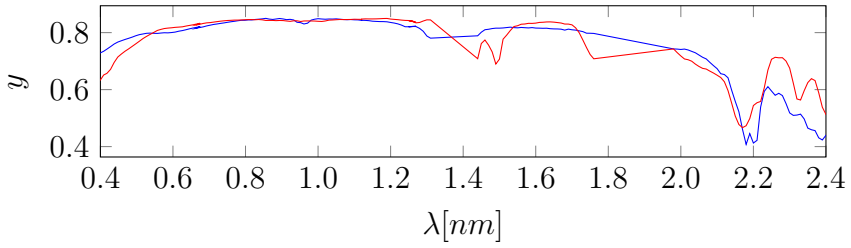

a) Original spectra. The coherence of these spectra pair equals 0.998

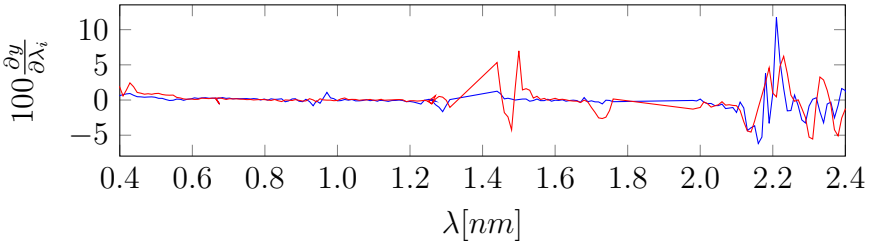

b) Derivative Spectra. The coherence of these spectra pair equals 0.281

Figure 4.7: Comparison of original and derivative spectra of Nanohematite and Smectite.

not guarantee selecting the correct ones. This leads to the same problem of correlations as in the sparse unmixing , i.e., removal or selection of a wrong endmember from the spectral dictionary. Additionally, when pruning of the dictionary is done globally , i.e., the endmembers are selected for the whole dataset at once, sometimes endmember which e.g. appear in only one pixel might be neglected from the dictionary.

In this section a new algorithm for TSGU will be presented. In order to avoid wrong endmember selection the algorithm, instead of selecting only one endmember, selects a group of correlated endmembers which is done at pixel level. From these groups a new pruned dictionary is constructed which is used in a final step for abundance estimation.

4.5.1 Dictionary Clustering

Each spectrum is usually similar to more than one spectrum by sharing same spectral features. This is often the case when the spectra belong to the same

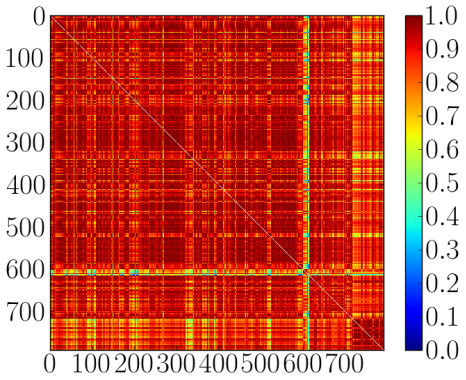

a) original USGS Dictionary with 792 spectra and 184 bands

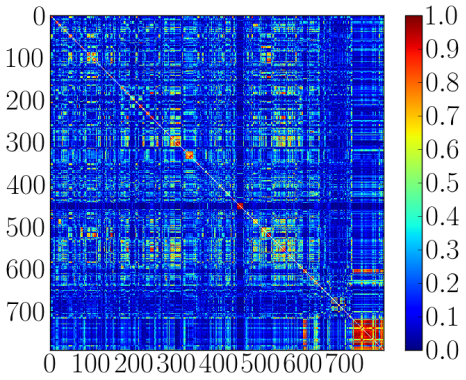

b) original USGS Dictionary with 792 spectra and 184 bands after derivative transform

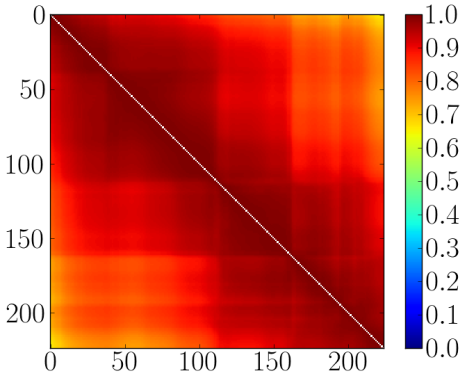

c) reduced USGS Dictionary with 224 spectra and 184 bands

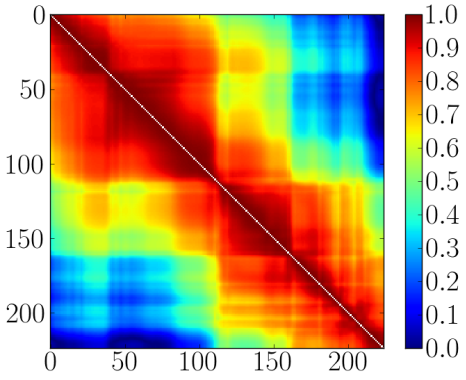

d) reduced USGS Dictionary with 224 spectra and 184 bands after derivative transform

Figure 4.8: Comparison of the correlation matrices computed from different dictionaries.

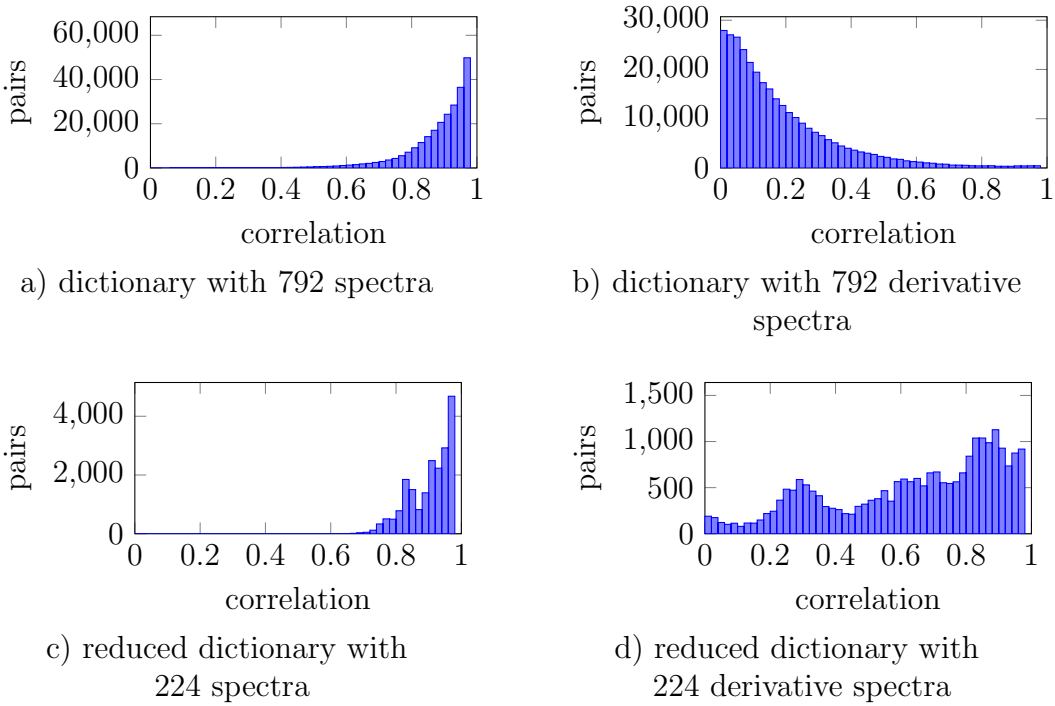

a) dictionary with 792 spectra

b) dictionary with 792 derivative spectra

c) reduced dictionary with 224 spectra

d) reduced dictionary with 224 derivative spectra

Figure 4.9: Histograms showing the number of endmember pairs with specific correlation. Correlations were computed for each endmember in the dictionary against all other endmembers.

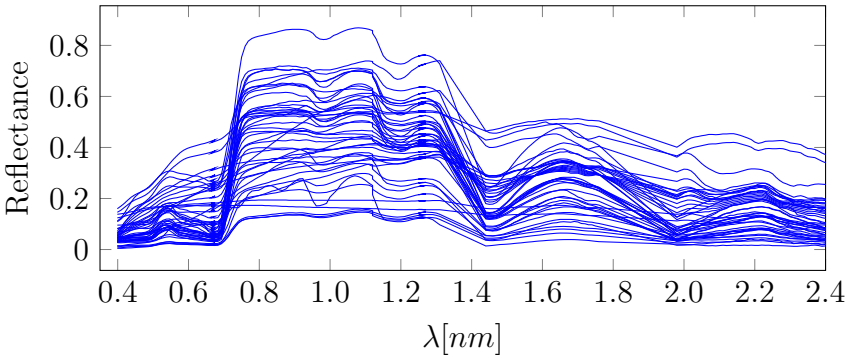

Figure 4.10: Spectra of different materials related to the semantic group vegetation from the spectral library *splib06* (Clark et al., 2007).

semantic group (see e.g. vegetation spectra Figure 4.10). Based on these similarities a dictionary can be clustered in groups of similar materials by means of a similarity measure (Hogan et al., 2009; Ramachandran et al., 2014).

One of the most popular and robust clustering algorithm is *K-Means*. It aims at minimizing the sum of squares in k number of clusters.

$$\min \sum_{1}^{k} \sum_{\mathcal{C}_i} \|a - \mu_i\| \tag{4.12}$$

where $\mathcal{C}_i$ is a ith cluster containing similar endmembers and μ_i is the mean of endmembers in this cluster.

4.5.2 Two Step Group Unmixing

As an initial step of the TSGU algorithm the clustering on a dictionary A is performed with a predefined number of clusters k. Then the algorithm operates on pixel level, i.e., each unmixing is performed for each pixel separately. For each pixel, first the initial unmixing using nLASSO or OMP is performed. Next, a new dictionary is created containing clusters of endmembers in which at least one endmember has a positive abundance. Using the pruned dictionary a second unmixing using nLASSO is performed and the final abundance vector is set. The pseudo code for this algorithm is shown

in Algorithm 4.

Algorithm 4: TSGU (Two Step Group Unmixing)

Input: A, $Y^{[m\times p]}$, δ_1, δ_{TSGU}, ϵ, c

begin
  Clustering: using *K-means* algorithm cluster dictionary A with n elements $\{a_1, a_2, ..., a_n\}$ in to a k sets of clusters where $\mathcal{L} = \{l(a)|a = 1, 2, ..., n\}$ is the set of clusters labels of A;
  initialize: set all $\hat{x}_{j,i}$ for $j \in 1, ..., m, p \in 1, ..., p$ to 0;
  for i = *1,...,p* **do**
    compute the initial $x_j^{(0)}$ abundance using the nLASSO or NOMP;
    find set of clusters $\mathcal{C}$ and labels of active endmembers $\mathcal{L}_\mathcal{C} = \{l(j)|j : x_j^{(0)} \neq 0\}$;
    construct a new pruned dictionary $A_\mathcal{C}$ containing endmembers labeled $\mathcal{L}_\mathcal{C}$;
    compute abundances $\hat{x}_i^\mathcal{C}$using dictionary with selected clusters $A_\mathcal{C}$ using nLASSO;
    set $[\hat{X}(j,i)|j \in C] \longleftarrow \hat{x}_i^\mathcal{C}$;
return $\hat{X}$;

4.6 Spatial Information – Multi-Look Joint Sparsity Model

Until now the presented methods were considering each pixel as a separate measurement. This concept was so far preferred as it is the traditional way of dealing with the unmixing problem. However, we should keep in mind that hyperspectral *images* besides the spectral information contain not less relevant spatial information. Usually, the spectral information is related to the spectral response of an object whereas spatial information is related to

a) b)

Figure 4.11: Illustration of spatial correlation among neighboring hyperspectral pixels. Pixels in the HyMap hyperspectral image (a) with a ground pixel size of 4 m are very often mixed. The mixture is usually spatially correlated, i.e., neighboring pixels contain common endmembers. E.g. all four neighboring pixels in (a) contain spectra from the road as seen in the high resolution ©Google Earth Image (b).

the texture of that object. Both are affected by the fact that usually a pixel will contain a mixture of some spectral signatures from its neighbours, which is due to e.g. oversampling effects in line scanner images (Müller et al., 2002). Therefore incorporating spatial information, i.e., neighouring pixels can improve the unmixing results (Iordache et al., 2012b; Plaza et al., 2002; Tang et al., 2014b). This however, should be done carefully because the neighbouring pixels besides the shared information from common objects might contain additional unique information (Figure 4.11).

4.6.1 Multi Look Joint Sparsity Model (MLJSR)

Based on the above facts a new model for spectral mixing including spatial-spectral relation can be formulated. Consider a set of spatially neighbouring pixels of size J. By applying the LMM, each pixel in this set can be formulated as a combination of endmembers weighted by abundances of these endmembers

$$y_j = Ax_j, \; j \in J \tag{4.13}$$

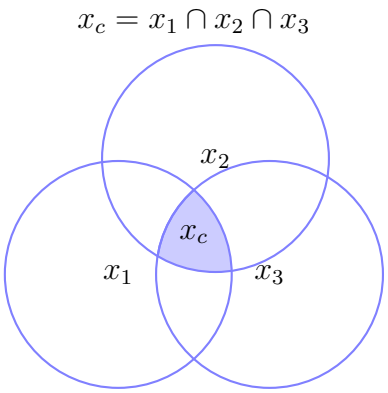

Figure 4.12: Venn diagram describing composition of the coefficient vector X_j. Modified from Baron et al. (2005)

Now, consider that every of the neighbouring pixel contains a portion of shared endmember abundance i.e a common abundance x_c for all $1 \leq j \leq J$ and abundances present only in that jth pixel x'_j. Then the model can be reformulated to a new Multi-Look Joint Sparsity Model (MLJSM)

$$y_j = Ax_c + Ax'_j \tag{4.14}$$

where the multiple neighboring pixels are hereinafter referred to as *looks*. The concept of the common endmember x_c is presented in Figure 4.12.

4.6.2 Multi-Look Joint Sparsity Reconstruction Algorithm

A new algorithm MLJSR can be formulated by applying the MLJSM and the joint sparsity concept introduced in section 3.4. Given the reflectance values of the jth hyperspectral pixel y_j in m hyperspectral bands, the model for MLJSM in a window with size of J pixels can be rewritten as

$$\tilde{y}_j = \tilde{A}\tilde{x}_j + \tilde{\varepsilon}_j \tag{4.15}$$

where $\tilde{\varepsilon}_j \in \mathbb{R}^{Jm}$ is an additive residual vector, $\tilde{y}_j \in \mathbb{R}_{\geq 0}^{Jm}$ is an ensemble of neighbouring hyperspectral pixels,

$$\tilde{y}_j = (y_1, y_2, y_3 \cdots y_J)^\top \tag{4.16}$$

and $\tilde{A} \in \mathbb{R}_{\geq 0}^{Jm \times (J+1)n}$ is a new spectral Joint Sparsity Model (JSM) dictionary composed of original spectral dictionaries containing endmembers arranged in blocks as follows,

$$\tilde{A} = \begin{bmatrix} A & A & 0 & 0 & \cdots & 0 \\ A & 0 & A & 0 & \cdots & 0 \\ A & 0 & 0 & A & \cdots & 0 \\ \vdots & \vdots & \vdots & \vdots & \ddots & \vdots \\ A & 0 & 0 & 0 & \cdots & A \end{bmatrix} \tag{4.17}$$

The first block column $(\tilde{a}_{11}..., \tilde{a}_{Jm \times n})$ of the dictionary $\tilde{A}$ is responsible for recovery of the common accounts for x_c contained in all J pixels. The block diagonal part of $\tilde{A}$ reconstructs the endmembers, which are not present in all pixels and are referred to as innovations. Then a new joint abundance vector $\tilde{x} \in \mathbb{R}_{\geq 0}^{(J+1)n}$ can be written as

$$\tilde{x}_j = [x_c, x'_1, x'_2 \cdots x'_J]^\top \tag{4.18}$$

and the abundance for the jth pixel can be computed using

$$x_j = x_c + x'_j. \tag{4.19}$$

After the ensemble vectors and the JSM dictionary has been introduced a minimisation problem solving the unmixing problem using MLJSM can be formulated as follows

$$\min_{\tilde{x}_j} \frac{1}{2} \|\tilde{A}\tilde{x}_j - \tilde{y}_j\|_2^2 + \gamma \|\tilde{x}_j\|_1 \text{ subject to } X_j \geq 0 \tag{4.20}$$

where again γ is responsible to trade sparsity for data mismatch. However, unlike in a standard sparse unmixing equation (4.3) the ℓ_1 regularisation influences the abundance of all pixels in the window. Due to the design of the joint abundance vector equation (4.18), setting γ properly high, will prune it to first recover common endmembers x_c and second the differences and unique endmembers in x_c. This allows to keep $\|\tilde{x}_j\|_1$ low. One of the advantages of the above MLJSM formulation is the fact that it can be solved using any BPDN method.

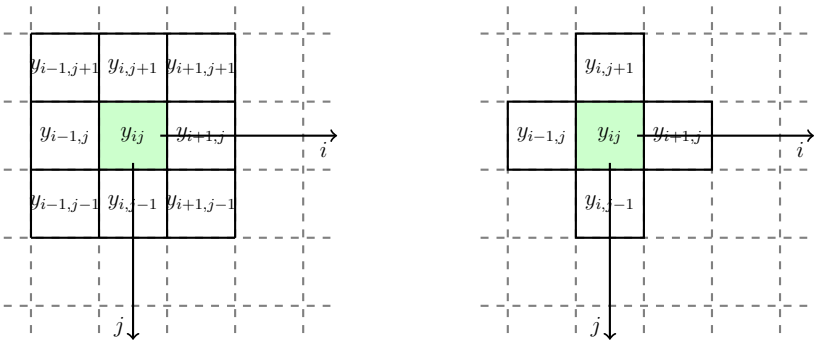

a) $J = 9$ b) $J = 5$

Figure 4.13: Schema describing how the ensemble pixel Y_j is created.

Algorithm 5: MLJSR (Multi-Look Joint Sparsity Reconstruction)

Input: A, $Y^{[m\times p]}$, γ, J

begin
  initialize: set all $\hat{X}^{[n\times p]}$ to 0, create the JSM dictionary $\tilde{A}$ using equation 4.17;
  for *k = 1,...,p* **do**
    construct ensemble $\tilde{y}$ by applying equation 4.16 where $y_1 = Y_p$ is the middle pixel in a window and $y_{2,\ldots,J}$ are the neighbouring pixels;
    estimate $\tilde{x}$ solving minimisation 4.20;
    set $\hat{x}_k$ using equation 4.19;
return $\hat{X}$;

The algorithm to perform spectral unmixing using MLJSM is presented in Algorithm 5 hereafter referred to as MLJSR. The unmixing is done in a sliding window. In this thesis two window shapes are considered, namely, a square-shaped [with J = 9, see Figure 4.13 a)] and a cross-shaped [with J = 5, see Figure 4.13 b)] window.

4.7 Complexity of the Discussed Algorithms

The algorithms for sparse unmixing, although all aim at finding sparse solutions to the same linear mixing model can have great differences in their computational complexity. Consider an unmixing problem with p pixels and n endmembers in the dictionary A and m spectral channels. Below we present the complexity analysis for selected algorithms.

- BPDN using LARS/LASSO algorithm for a single pixel the complexity is of $O(nmk+nk^2)$ where k is the number of nonzero coefficients. When the approximation is done for p pixels the pre-computation of the gram matrix A^TA can reduce the cost of p times previous complexity to $O(n^2m + pn(m + k^2))$ for the whole minimization (Bach et al., 2011; Mairal et al., 2010).

- MLJSM using LARS/LASSO algorithm: Accordingly, the MLJSM is solved by the same solver as BPDN the complexity will be of $O(\tilde{n}^2\tilde{m} + p\tilde{n}(\tilde{m} + k^2))$ where $\tilde{m} = mJ$ and $\tilde{n} = n(J + 1)$ for the window of size J.

- OMP: $O(pnmk)$ exhibits very similar complexity to the LARS/LASSO algorithm. The decrease in complexity is also achieved thanks to pre-computation of the Gram matrix A^TA (Mailhé et al., 2011).

- NNLS and FCLS: $O(n^2pi)$ where i is the number of iterations.

- The complexity of TSGU consists of the preselection of $O(n^2m+pn(m+k^2))$ and the final abundance estimation done by means of NNLS $O(n'^2pi)$. Here, n' denotes the number of endmembers after preselection and i iterations needed by the NNLS algorithm. Note that the complexity of etimation varies in each pixel, because n' is dependent from the preselection step.

- BPDN using SUnSAL algorithm has the same complexity as NNLS $O(n^2pi)$ where i is the number of iterations needed until convergence (Iordache et al., 2010).

- SUnSAL-TV is an extension of SUnSAL algorithm. The algorithm additionally computes at each step the total variation penalty. Therefore, its complexity is of $O(n^2pi + mpi \log m)$ (Iordache et al., 2012b).

- The complexity OLS is of $O(n^2p)$.

Algorithms LARS/LASSO, MLJSM, and OMP have significantly lower complexity considering the case when the number of pixels is larger than the number of bands, which is a reasonable assumption. The actual computational time additionally depends on the iterations needed by the particular algorithm to converge. This will be tested in the experimental part of this thesis.

4.8 Summary

In this chapter the sparse spectral unmixing problem has been addressed. The following sumarizing remarks can be drawn

- The application of modern signal processing methods for sparse approximation allows a more automatized and intuitive approach to hyperspectral unmixing. However, unlike traditional least squares-based

methods, sparsity-based techniques do not require a preselection of endmembers and are thus able to simultaneously estimate the underlying active materials along with their respective abundances. So the expensive step of manual selection or extraction of endmembers can be avoided.

- The results of the sparse approximation methods are highly dependent on the properties of the dictionary e.g. mutual coherence. This limits the usability of some dictionaries and causes errors in the results. A proposed way to deal with this problem is to reduce the correlations between endmembers in the dictionary by applying a derivative transform to the data and dictionary. The problem of correlations has been stated by many researchers and the proposed derivative method is a first approach to deal with this problem.

- Another approach to precondition the unmixing problem is to reduce the size of the spectral dictionary. The proposed TSGU method operates pixel wise by performing first a preselection of endmember groups and second estimation of abundances for endmembers in these groups. This method thanks to the group preselection, unlike other state of the art algorithms, is less susceptible to removal of significant endmembers. Additionally, the preselection reduces the size of the unmixing problem what results in lower complexity of the second unmixing problem.

- Having in mind that hyperspectral images exhibit spatial correlations. therefore the use of spatial along with the spectral information might help in the unmixing process. One possible way to do so is to use the new MLJSR algorithm for spectral unmixing. This approach is able to relax, yet exploit, the assumption of spatial homogenity by introducing a new MLJSM that captures both similarities and differences between neighbouring abundances.

The above concepts as well as the new proposed algorithms will be assessed with experiments in chapter 6.

5

Hyperspectral Image Resolution Enhancement

The relatively low spatial resolution of space-borne hyperspectral images is the main drawback to derive value added products. Recently, several techniques have been proposed in order to enhance the spatial resolution of the hyperspectral image by means of fusion with higher spatial resolution multispectral images. In this chapter techniques for resolution enhancement focused on utilising spectral unmixing results enhancement are discussed. Also a new method based on the multi-look joint sparse model is presented.

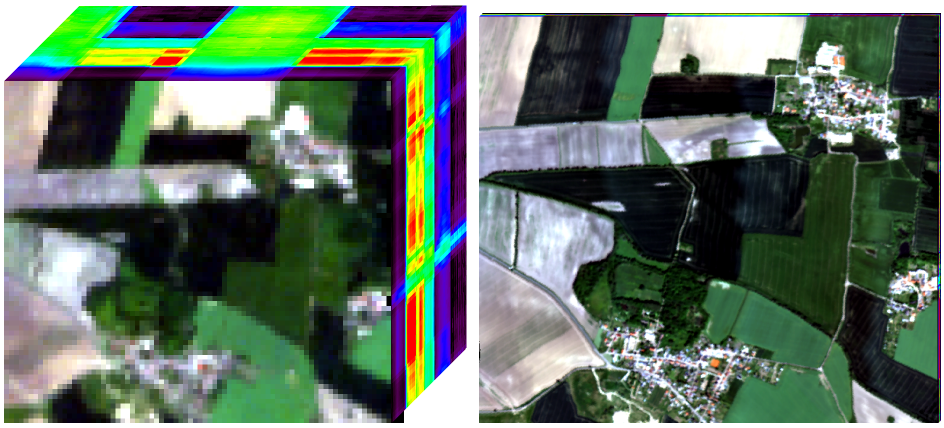

a) Hyperspectral data cube b) Multispectral data cube

Figure 5.1: Comparison of hyperspectral and multispectral data cubes of the same region.

5.1 Unmixing Based Hyperspectral Resolution Enhancement - the Concept

As already mentioned in section 2.2 the spatial resolution of current and future hyperspectral spaceborne sensors is severely limited due to the amount of the light needed to be split to hundreds of spectral bands. As a result many applications which require high spatial resolution will have limited usability with these systems. This problem is typically addressed by resolution enhancement methods, which aims at increasing the spatial resolution of a hyperspectral image while preserving valuable spectral information. One option for the resolution enhancement is to fuse information from the hyperspectral image with a higher spatial resolution image but with fewer bands. For this purpose imagse from a multispectral sensor can be used. Recalling Figure 2.7, e.g., the Hyperion sensor has 224 spectral bands and GSD of 30m, while WV2 samples the image with 8 spectral bands and GSD of 2m. As a result of fusion of these two image types a high spatial and spectral resolution imagery should be able to be generated.

5.2 Related Work

5.2.1 Sharpening Methods

A typical and widely known example of fusion based resolution enhancement is the sharpening of the multispectral image a high resolution panchromatic image and is called pan-sharpening, where the lower spatial resolution of the multispectral image is being *sharpened* using the spatial information from the usually higher resolution pan image (Stathaki, 2011). There have been dozens of pan-sharpening methods developed which are widely used in many applications to increase the image quality of the space-borne color satellite imagery, e.g. in services like google earth, bing maps or yahoo maps. A common denominator for all sharpening methods is the requirement of the temporal consistency (the images were acquired at the same time), spatial range consistency (images of the same area) and spectral range consistency (i.e. the PAN image SRF covers the same spectral range as the SRFs of the sharpened multispectral bands) (Alparone et al., 2007; Ehlers, 2008; Thomas et al., 2008).

Similarly to pan-sharpening, the resolution enhancement of the Hyperspectral image using a multispectral image is recently gaining more attention from researchers. This is additionally driven by the large amount of planned hyperspectral satellite missions as well as the rising number of applications for these data. However, the multispectral-hyperspectral resolution enhancement brings much more challenges to face than the pan-sharpening where the key role plays the lack of a platform carrying both the hyperspectral and the multispectral sensors. It also results in temporal in-consistency. Another problem is caused by the significant increase of dimensionality of these data where hundreds hyperspectral bands are being *sharpened* using few multispectral bands. Additionaly, often some bands of the hyperspectral image do not have overlaping multispectral bands in the corresponding spectral range. In light of these facts, the direct use of the pan-sharpening methods

for multispectral-hyperspectral resolution enhancement is limited. Therefore, researchers developed new methods or modified existing ones (Chen et al., 2014) in order to make them applicable to the hyperspectral image *sharpening*. Some of the new methods include the principle component sharpening (Winter et al., 2002), Bayesian fusion (Hardie et al., 2004a; Wei et al., 2013; Zhang et al., 2012) or simply blur transform (Mayumi and Iwasaki, 2011). Some authors approached the resolution enhancement of the hyperspectral images by fusion with panchromatic images (Capobianco et al., 2007; Licciardi et al., 2012; McKeown Jr et al., 1999). The problem of hyperspectral image sharpening has also been approached using sparse regularisation methods. E.g. in Grohnfeldt et al. (2013, 2014) authors make use of the co-trained high and low resolution multispectral dictionary containing patches of the image. This dictionary is then used to estimate the low resolution multispectral image by a linear combination of patches. Then the high resolution patches are used to estimate the high resolution image.

5.2.2 Unmixing Based Methods

Another approach to resolution enhancment of the hyperspectral data is to apply the information obtained from the hyperspectral unmixing. As it has been described in chapter 4, usually the hyperspectral pixels are mixed i.e. they consist of signals from more than one unique endmember. This fact, can be used to allocate these endmembers in a new higher spatial resolution image according to the information retrieved from the high resolution multispectral image. The principle of spectral mixing for image resolution enhancement has been first used by Zhukov et al. (1999) where the low resolution hyperspectral image has been unmixed in a window using information from the classification of the high resolution multispectral image. Then the high resolution hyperspectral image was reconstructed by assigning endmembers to the high resolution classification map. In this method it is assumed that the classes in the multispectral image were related to endmembers in the multispectral image. Even though the assumption seem to work in experiments the

algorithm might have problems with more diversified images or where there is no pure pixel. Another unmixing based method was proposed in Robinson (1997) and Robinson et al. (2000). Here however the hyperspectral image was *sharpened* using the unmixing results and the panchromatic image. A different approach but also related to spectral unmixing was presented by Eismann and Hardie (2005a) where instead of the popular linear mixing model the stochastic mixing model (Eismann and Hardie, 2004) for the hyperspectral unmixing was applied. This was used together with the maximum a posteriori method by Hardie et al. (2004b) to estimate the high resolution hyperspectral image. A simple algorithm for hyperspectral resolution enhancement has been shown by Bieniarz et al. (2011) where the endmembers were extracted using the vertex component analysis method. The endmembers were resampled to the spectral resolution of the mutispectral sensor and used to estimate the abundances in the high resolution multispectral image. Finally, abundances of the high resolution image were combined with hyperspectral endmembers to reconstruct the high resolution hyperspectral image. The main drawback of this method was the limitation on the number of endmembers constrained by the dimensionality of the multispectral image, i.e., number of spectral bands. A similar model for resolution enhancement was presented in Kawakami et al. (2011) where the abundance estimation of the multispectral image is performed with a sparsity prior. Also Yokoya et al. (2012) utilised a similar scheme in the CNMF method. However, here the abundance of endmembers in the multispectral and hyperspectral image was iteratively updated. The estimation was done using the non negative matrix factorisation method. This method for initialisation used endmembers extracted by vertex component analysis. Also Bendoumi et al. (2014) showed that the limitation of the number of endmembers can be overcome by subdivision of the hyperspectral image into regions.

5.3 Research Questions

In previous related works it has been shown that the resolution enhancement of hyperspectral images can be performed by fusion with higher resolution multispectral images using the information from spectral unmixing. In this chapter the actual state-of-the art in research is pushed forward by answering following research questions:

- The endmembers extracted from the image at first point are not assigned to any materials, i.e., a supervised recognition of the spectral features related to specific materials is required. This means that the unmixing performed in the traditional resolution enhancement algorithms serves rather as a decomposition than having a physical meaning. However, spectra from external spectral dictionaries represent specific material. Based on that fact, is it possible to use these dictionaries as an input to the resolution enhancement algorithm in order to retrieve meaningful low as well as high resolution material abundance maps?

- The unmixing based methods for hyperspectral resolution enhancement usually preform the abundance estimation on the multispectral image. The low number of spectral bands severely limits the amount of the endmebers which can be used. This fact is especially important for large diversified scenes. Can the preselection of endmembers for the multispectral unmixing allow the use of large amount of spectra in the dictionary?

5.4 Multi-Look Jointly Sparse Fusion

In this section the MLJSF algorithm is presented. The algorithm utilises previously presented concepts of sparse spectral unmixing (chapter 4) and in

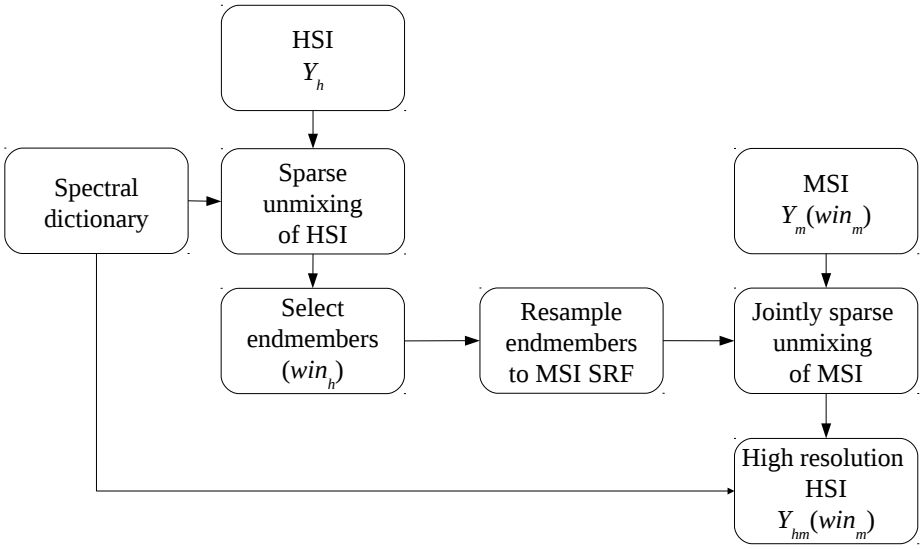

Figure 5.2: Scheme of the proposed method. MSI denotes multispectral image and HSI hyperspectral image.

particular is using the LMM and MLJSM. The algorithm in contrast to the state of the art methods does not extract endmembers from the image, but performs the unmixing of the hyperspectral data using a spectral dictionary and the nLASSO algorithm. Finally it fuses the result of the unmixing with the multispectral image in a window based manner. The scheme of the MLJSM is presented in Figure 5.2 and consists of the steps described in following sections.

Spectral Unmixing

In a first step the low resolution hyperspectral image Y_h is unmixed using a spectral dictionary A_h containing spectral endmembers and the nLASSO method using the linear model

$$y_h = A_h x_h + \epsilon_h \tag{5.1}$$

where y_h is the p'th pixel of Y_h, x_h is an abundance vector and ϵ_h denotes the noise in the hyperspectral pixel. Note that the spectral dictionary in the MLJSF method is not restricted to the external spectra but it also can be retrieved from the image using any common endmember extraction algorithm like in Bieniarz et al. (2011) or Yokoya et al. (2012). The main purpose of this step is to detect endmembers mixed in each hyperspectral pixel.

Resampling and Window Based Endmember Selection

In order to use the dictionary A_h for the multispectral image it has to be resampled to match the spectral resolution of the multispectral sensor (see section 2.2.5). The new multispectral dictionary A_m image is defined as

$$A_m = RA_h \tag{5.2}$$

where R is a matrix of a size $[m_m \times m_h]$ containing SRFs of the m_m multispectral bands sampled in the range or the hyperspectral sensor with m_h bands.

From now on the algorithm performs in a sliding window win_h for all hyperspectral pixels p_h. In each win_h a set $\mathcal{V} = \{j : x_i \neq 0\}$ of contributing spectra is selected and a new pruned multispectral dictionary $A_m^{\mathcal{V}}$ is constructed. The step of selecting spectra is crucial for this method because it reduces the complexity of the problem by excluding unused endmembers.

Unlike most of resolution enhancement methods the MLJSF algorithm has been inplemented to be able to fuse not aligned images using only an affine transformation matrix. This advantage is very useful when e.g. extensive interpolation is needed for the co-registration. Additionally the window-based selection of endmembers makes the algorithm relatively robust to the co-registration error or small errors in the transformation matrix.

Multispectral Unmixing - Fusion

The dictionary selected in the previous step is now used to perform the abundance estimation in the corresponding window win_m of the multispectral image. The model for multispectral unmixing can be written as

$$y_m = A_m^{win_m} x_m^{win_m} + \epsilon_m \tag{5.3}$$

The abundance estimation is done using the MLJSR algorithm. Since in the higher resolution image the neighbouring pixels are more likely composed of the same materials, they will share abundances and therefore the use of MLJSM helps in the joint recovery for these materials. Additionally, the decrease of the dimensionality in the spectral domain limits the applicability of standard pixel based methods, where the MLJSR uses the surrounding pixels to support the approximation.

High Resolution Hyperspectral Image Reconstruction

Once the abundance of the selected materials has been estimated the reconstruction of high spatial and high spectral resolution pixels is performed in a win_m. The new high spatial and high spectral resolution pixel is reconstructed again using the LMM

$$y_{hm} = A_h x_m \tag{5.4}$$

The spatial structures as well as the material abundances are retrieved from the high resolution abundance matrix X_m and the spectral information is used from the hyperspectral dictionary. A pseudo code for the MLJSM method is presented in Algorithm 6.

Algorithm 6: MLJSF (Multi-Look Joint Sparsity Fusion)

Input: HSI $Y_h^{[m_h \times p_h]}$, MSI $Y_m^{[m_m \times p_m]}$, hyperspectral dictionary A_h, signal response function of the MSI R

Output: High spatial resolution HSI $Y_{hm}^{[m_h \times p_m]}$

begin
- **initialize:** Compute the initial X_h abundance using the nLASSO;
- Resample A_h to multispectral channels using equation equation (5.2);
- Set all elements of the multispectral abundance matrix X_m to 0;
- **for** *i = 1,...,p_h* **do**
  - find set of active endmembers $\mathcal{V} = \{j : x_i \neq 0\}$ in $win_h(i)$;
  - get a subset A_m for $j \in \mathcal{V}$ constructing a new pruned dictionary $A_m^{\mathcal{V}}$;
  - compute abundances $X_{win_m}^{\mathcal{V}}$ of the corresponding window win_m in a multispectral image using $A_m^{\mathcal{C}}$ and the MLJSR algorithm;
  - set $[X_m(j, win_m)|j \in V] \longleftarrow X_{win_m}^{\mathcal{V}}$;
- Reconstruct the high resolution HSI using equation (5.4);

return Y_{hm};

In case of MLJSF the abundance estimation is performed on both datasets and therefore the portion of noise is removed from both y_h and y_m. Note, that this assumption requires very good unmixing results as well as atmospheric correction for both datasets.

5.5 Summary

In this chapter the MLJSF algorithm for resolution enhancement of hyperspectral image data has been presented. The following has been discussed

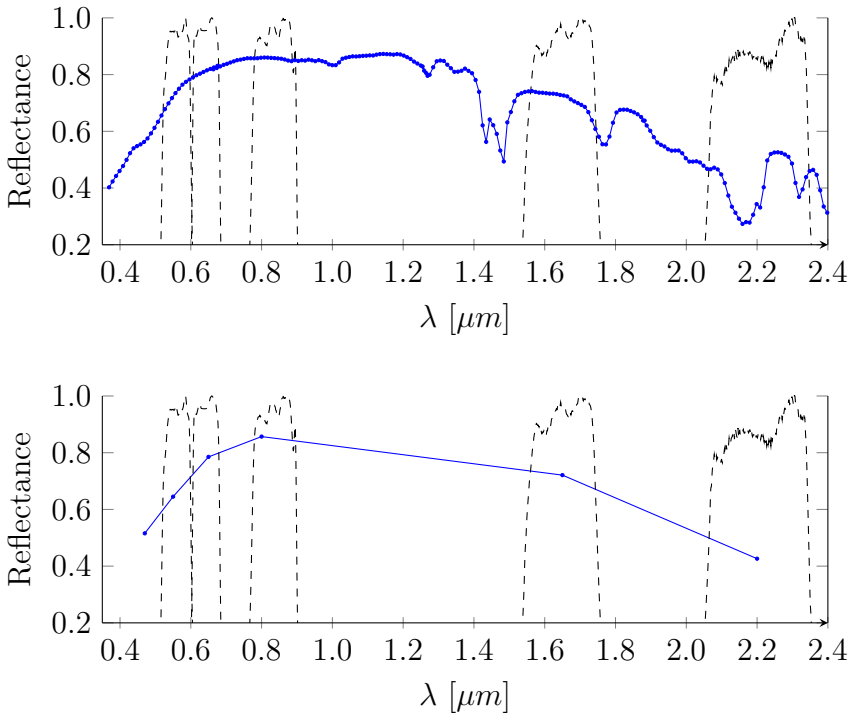

Figure 5.3: Comparison between the spectral resolution of a hyperspectral and a multispectral image. The dashed line represents the relative SRF of the Landsat 7 sensor.

- The growing amount of future hyperspectral spaceborne sensors and applications for high resolution hyperspectral data will require *sharpened* hyperspectral data. However, often current pan-sharpening methods can not be directly applied for this purpose and therefore developments of new robust methods are needed.

- The presented algorithm utilises sparse spectral unmixing techniques and high resolution multispectral image data to provide a high resolution hyperspectral image. The algorithm works with external libraries which allows to avoid the endmember extraction process. Additionally, as *by-products*, provides meaningful abundance maps referring to actual endmembers. These maps are produced in both high as well as low resolutions.

- MLJSF uses sparse approximation methods for both unmixing steps. These methods have been shown to outperform traditional abundance methods (see chapter 4). Also LASSO and MLJSR are much faster than other state of the art methods.

Part III

Results and Conclusion

6

Evaluation of Sparse Spectral Unmixing Models

In this chapter the comprehensive comparison of sparse approximation methods applied to spectral unmixing is presented. First, the pixel based methods including the proposed approaches i.e. derivative method for coherence reduction as well as TSGU will be compared to the state of the art methods. The comparison will be performed using simulated data. Second, the performance of the MLJSR in different settings will be tested by comparison to pixel based methods and spatial unmixing methods. Third, selected algorithms will be tested using real hyperspectral scenes. Finally, the algorithms are compared for the speed performance taking into account different settings

.

6.1 Evaluation Criterion

The result of the spectral unmixing and the abundance recovery should be evaluated considering both the accuracy of estimation of the abundance vector as well as the accuracy of the detection of endmembers. Since abundance recovery aims at estimating the abundance vector $\hat{x}$ and not reconstruct the hyperspectral signal $\hat{y}$, in this chapter the performance measures of $\hat{x}$ will be advantageous. However, this can only be done when ground truth data i.e. the true actual fractional abundance is available. Therefore, in case of the real data experiments, due to the lack of ground truth data only qualitative analysis will be performed. In order to evaluate the results of tested unmixing methods the following measures will be applied.

6.1.1 Abundance Mean Squared Error

To measure the error of the abundance estimation the A-MSE is used. Which is defined as relative version of the Mean Squared Error (MSE)

$$\text{A-MSE} = \frac{\|x - \hat{x}\|_2^2}{\|x\|_2^2} \tag{6.1}$$

where x is the ground truth abundance and $\hat{x}$ is the estimated abundance. High values of A-MSE indicates high error while low A-MSE low error with perfect reconstruction for A-MSE$\rightarrow$ 0. Since A-MSE measures the power of both signal and error, larger residuals contribute more to the error when compared to small residuals.

6.1.2 Reflectance Mean Squared Error

Similarly to A-MSE the R-MSE measures the error in reflectance. R-MSE is defined as

$$\text{R-MSE} = \frac{\|y - A\hat{x}\|_2^2}{\|y\|_2^2} \tag{6.2}$$

where A denotes the spectral dictionary used for unmixing. This measure is used by many researchers but it is not able to directly measure the accuracy of abundance estimation. However, comparing R-MSE with A-MSE can be helpful in studding the results of abundance estimation. E.g. if R-MSE is low and A-MSE is high this indicates that the algorithm might have had problems in selecting correct endmembers due to e.g. coherence in the dictionary.

6.1.3 Mean Absolute Error

Table 6.1: Comparison between MSE and MAE. The original vector is sparse and has only one nonzero value equal 1. e_i denotes the residual error defined as $e_i = |x_i^o - \hat{x}_i|$.

Example No.	1	2	3	4	5	6
e_1	0.2	0.1	0.1	0	0	0
e_2	0.2	0.1	0.1	0	0	0
e_3	0.2	0.3	0.1	0.4	0.1	0
e_4	0.2	0.3	0.5	0.4	0.7	0.8
MSE	0.16	0.19	0.28	0.32	0.5	0.64
MAE	0.8	0.8	0.8	0.8	0.8	0.8

A-MSE tends to over-represent large errors and neglect values of small errors. Therefore in case when all errors should be weighted equally the use of MAE is of importance. This is especially useful to track small errors often related to overfitting i.e. noise compensation. MAE measures the average

magnitude of errors weighted equally. The relative MAE is defined as

$$\text{MAE} = \frac{\|x - \hat{x}\|_1}{\|x\|_1}. \tag{6.3}$$

MAE can have values form 0 to ∞ the smaller MAE is, the better the estimation. Additionally comparing MAE with A-MSE allows to indicate what type of the error occurs. Low MAE and high A-MSE indicate presence of very large errors while high MAE and low A-MSE suggests presence of many small errors but not large errors. An example is given in Table 6.1.

6.1.4 Endmember Detection Accuracy

In order to evaluate the accuracy of detecting correct endmembers in the abundance vector confusion matrix values are used. The confusion matrix is calculated by comparing the binarized version of the estimated abundance vector $\hat{x}^b$ and the binarized ground truth vector x^b defined as

$$x^b(i) = \begin{cases} 0 & \text{if } x(i) = 0 \\ 1 & \text{if } x(i) > 0 \end{cases}, \; \hat{x}^b(i) = \begin{cases} 0 & \text{if } \hat{x}(i) = 0 \\ 1 & \text{if } \hat{x}(i) > 0 \end{cases}. \tag{6.4}$$

The detection of an endmember i is considered as *True Positive (TP)* when $x^b(i) = \hat{x}^b(i) = 1$. When $x^b(i) \neq \hat{x}^b(i)$ the detection is labelled as *False Positive (FP)*. Similarly, when $x^b(i) = \hat{x}^b(i) = 0$ detection is *True Negative (TN)* and for $x^b(i) \neq \hat{x}^b(i) = 0$ detection is *False Negative (FN)*. Based on the confusion matrix the following accuracy measures are considered:

Accuracy

ACC measures general accuracy of endmember detection considering both TP and TN by comparing them to the ground truth values. The ACC is

calculated as follows

$$\mathrm{ACC} = \frac{\sum \mathrm{TP} + \sum \mathrm{TN}}{\sum \mathrm{P} + \sum \mathrm{N}} \tag{6.5}$$

Where P denotes $x^b(i) = 0$ and N denotes $x^b(i) = 1$.

Sensitivity

To measure how well the algorithm detects endmembers the SNT rate is defined as

$$\mathrm{SNT} = \frac{\sum \mathrm{TP}}{\sum \mathrm{P}} \tag{6.6}$$

The SNT can range from 0 to 1 and represents proportion of TP to the ground truth. Where 0 means that there were no TP and 1 when all P have been correctly detected i.e. $\sum \mathrm{P} = \sum \mathrm{TP}$.

Specificity

Similarly the SPC is defined as

$$\mathrm{SPC} = \frac{\sum \mathrm{TN}}{\sum \mathrm{N}} \tag{6.7}$$

The SPC can have values from 0 to 1 where 1 indicates that all N were detected and 0 indicates that there has been no TN. The measure of SPC indicates how well the algorithm sets values to 0.

Note that ACC, SNT and SPC are used only to show the detection accuracy and they do not provide evaluation of the abundance accuracy. Therefore, these measures should be interpreted carefully and taking into account that e.g. very high SNT can result from very dense results i.e. many $\hat{x}^b(i) = 1$ or very high SPC can be caused by very sparse solutions i.e. many $\hat{x}^b(i) = 0$.

6.2 Pixel Based Sparse Unmixing and Spectral Derivative Application

6.2.1 Experiment Settings

For the pixel based sparse unmixing the spectral dictionary was created using 432 selected spectra from the USGS spectral library (Clark et al., 2007). Every spectrum has been resampled to match the original SRF of the Airborne visible/infrared imaging spectrometer (AVIRIS) sensor using formulas described in section 2.2.5. The complete list of used spectra is presented in Appendix B.

To simulate spectral mixtures the following simulation scenario is constructed

1. Form a mixing matrix $M \in \mathbb{R}^{[m \times n']}$ by selecting n' endmembers at random from A,
2. Create an abundance vector $x'^{[n']}$ by randomly assigning elements such as $x_i > .01$ and $\|x\|_1 = 1$,
3. Generate a mixed spectrum by means of LMM $y'^{[m]} = Mx' + \varepsilon'$, where $\varepsilon'^{[m]}$ is Gaussian noise with an $\text{SNR}[dB] = 10\log_{10}\frac{\|y'[m]\|_2^2}{\|\varepsilon'[m]\|_2^2}$.

The simulated data consisted of 10 000 spectra containing mixtures of 2 to 10 equally distributed endmembers. In such way 5 sets of data were generated with SNRs of 20dB, 30dB, 40dB and 50dB.

In the experiment following algorithms were used to perform abundance estimation

- nLASSO and nLASSOd where "d" denotes use of the derivative method. The solver used for this problems was from the software package SPArse

Modeling Software (SPAMS) reported in Mairal et al. (2010) with plug-in for python.

- NOMP and NOMPd implemented in python (see Algorithm 3).
- Fast Iterative Shrinkage-Thresholding Algorithm (FISTA) and FISTAd algorithm solving nBPDN problem (for details see (Jenatton et al., 2010)). The algorithm was executed using the the software package SPAMS in python.
- TSGU using nLASSO for preselection. The solver was implemented in python following Algorithm 4.
- TSGU-NOMPd using NOMPd for preselection.
- NNLS using python built-in function *scipy.optimize.nnls*
- SUnSAL using the Matlab code from (Bioucas-Dias, 2012).
- FCLS using Matlab built-in function *lsqlin*

Every algorithm was run with 10 different parameter settings and the result with the highest A-MSE was chosen. The algorithms were executed on Intel(R) Core(TM) i5-2520M CPU @ 2.50GHz processor with 8GB of RAM using Python 2.7.3 and Matlab 7b.

6.2.2 Results and Discussion

Global Errors

First, the algorithms were compared globally by calculating the mean values of A-MSE, MAE and R-MSE for all estimated abundance vectors in each data set with different SNR. The results are shown in Figure 6.1.

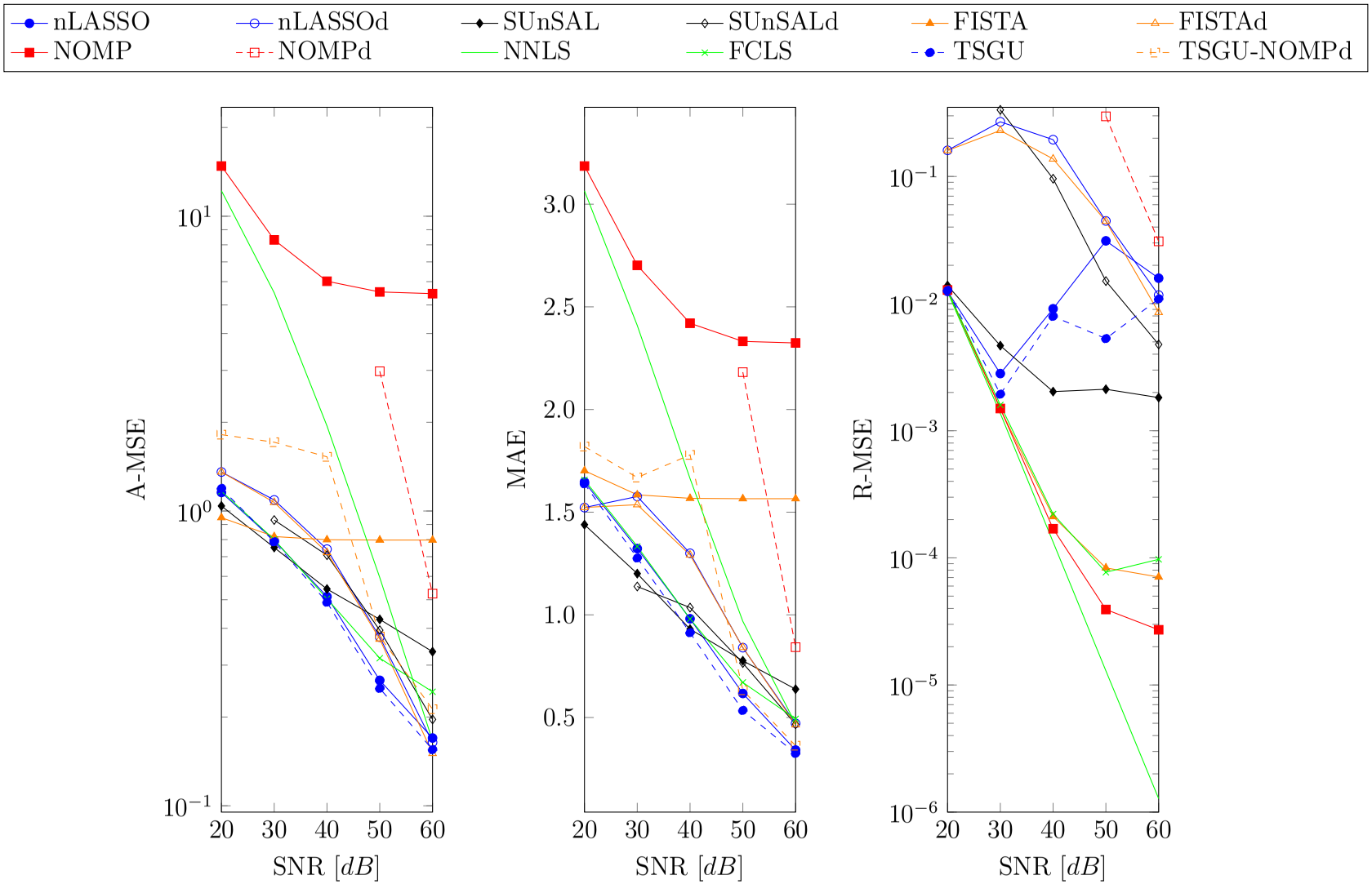

Figure 6.1: Plots of mean errors for datasets with different SNR values. The plots present (from left to right) A-MSE, MAE and R-MSE.(For algorithms NOMPd and SUnSALd the results with very high errors were excluded in order to enable visualisation of the results)

Considering the A-MSE measure, algorithms nLASSO, TSGU, SUnSAL and FCLS perform similarly for SNR values equal 20dB and 30dB with slightly lower mean A-MSE when using SUnSAL. For SNRs from 40dB to 60dB algorithm TSGU exhibit the lowest A-MSE followed by nLASSO and FCLS. The NOMP method performs the worst showing the highest A-MSE values for all test cases. However, for SNRs 50dB and 60dB and applying the derivative method (NOMPd) seems to significantly improve the results of the NOMP algorithm. This is also the case for SUnSALd and FISTAd. Similarly to mean A-MSE, the mean MAE measure indicates the best performance for TSGU in SNR range of 40dB to 60dB. Using the R-MSE measure shows that the algorithm NNLS provide the best estimation of $\hat{y}$ followed by OMP, FISTA and FCLS. Note, that the algorithms NNLS and NOMP have low R-MSE but high A-MSE and MAE values indicating very good reconstruction of spectrum but poor estimation of abundance vector.

Errors With Respect to Number of Mixed Spectra

The Figure 6.2 shows A-MSE errors with regard to endmembers in the ground truth for different SNR scenarios. For all algorithms the increase in the contribution of endmembers results in an increase of the A-MSE error. In the test cases with low SNR i.e. 50dB and 60dB, there is significant decrease in A-MSE and MAE error for FISTA, NOMP and SUnSAL algorithm after applying the derivative method (FISTAd, NOMPd and SUnSALd). Similarly to the A-MSE error, the MAE error rises with the increase of the contributing endmembers (Figure 6.3). The nLASSO algorithm exhibits a more stable MAE curve than the A-MSE curve which indicates the presence of large errors e.g. mixture of 5 endmembers in SNR 50dB case or mixture of 6 endmembers for SNR equal 60dB. In all test cases considering both measures A-MSE and MAE the algorithm TSGU outperforms LASSO. Similarly TSGU-OMPd exhibit lower errors than OMP whereas for high SNR values it results in similar A-MSE and R-MSE as the ℓ_1 regularized algorithms.

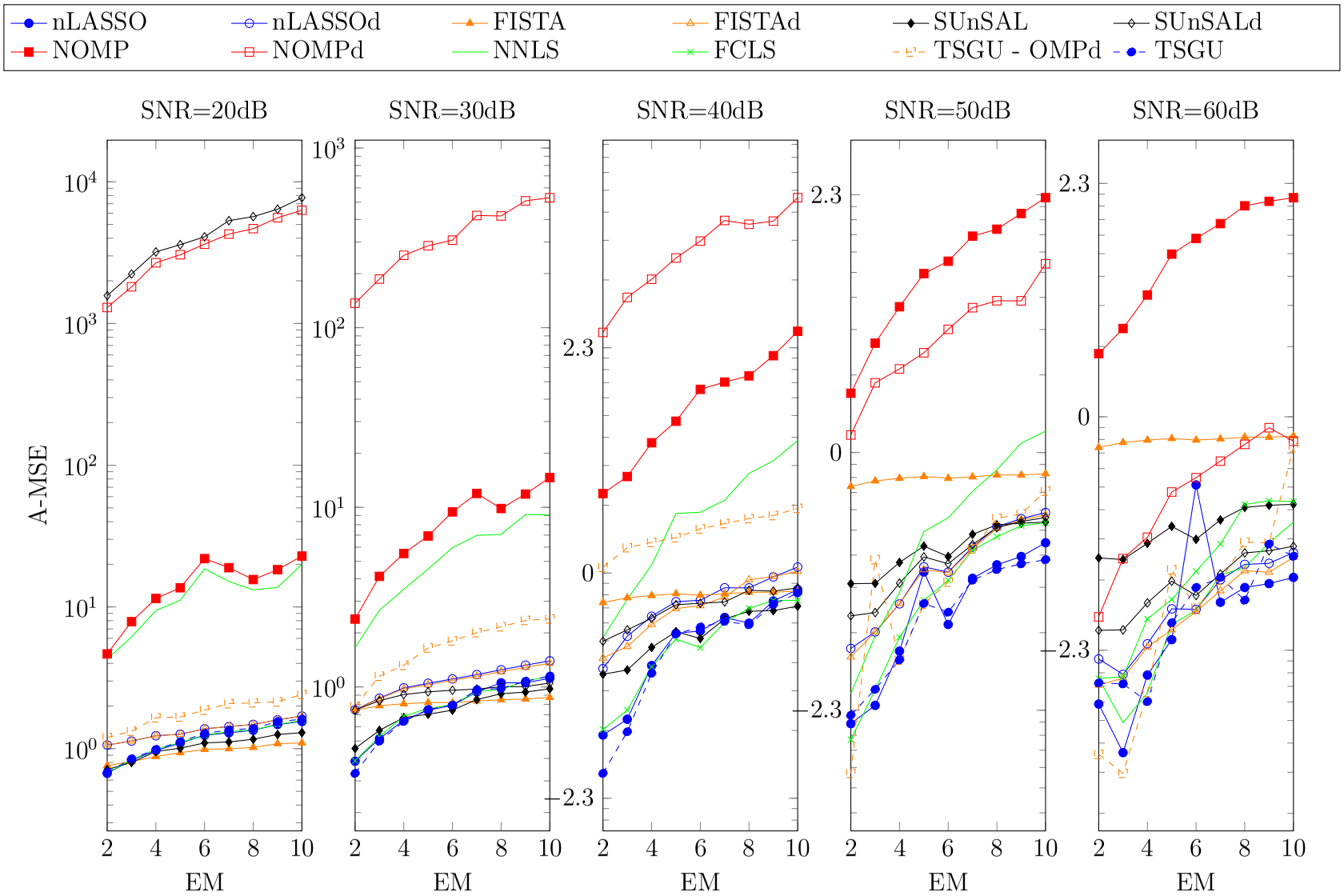

Figure 6.2: Results of abundance estimation for different SNR values. Plots present relation between the A-MSE measure and the number of contributing .

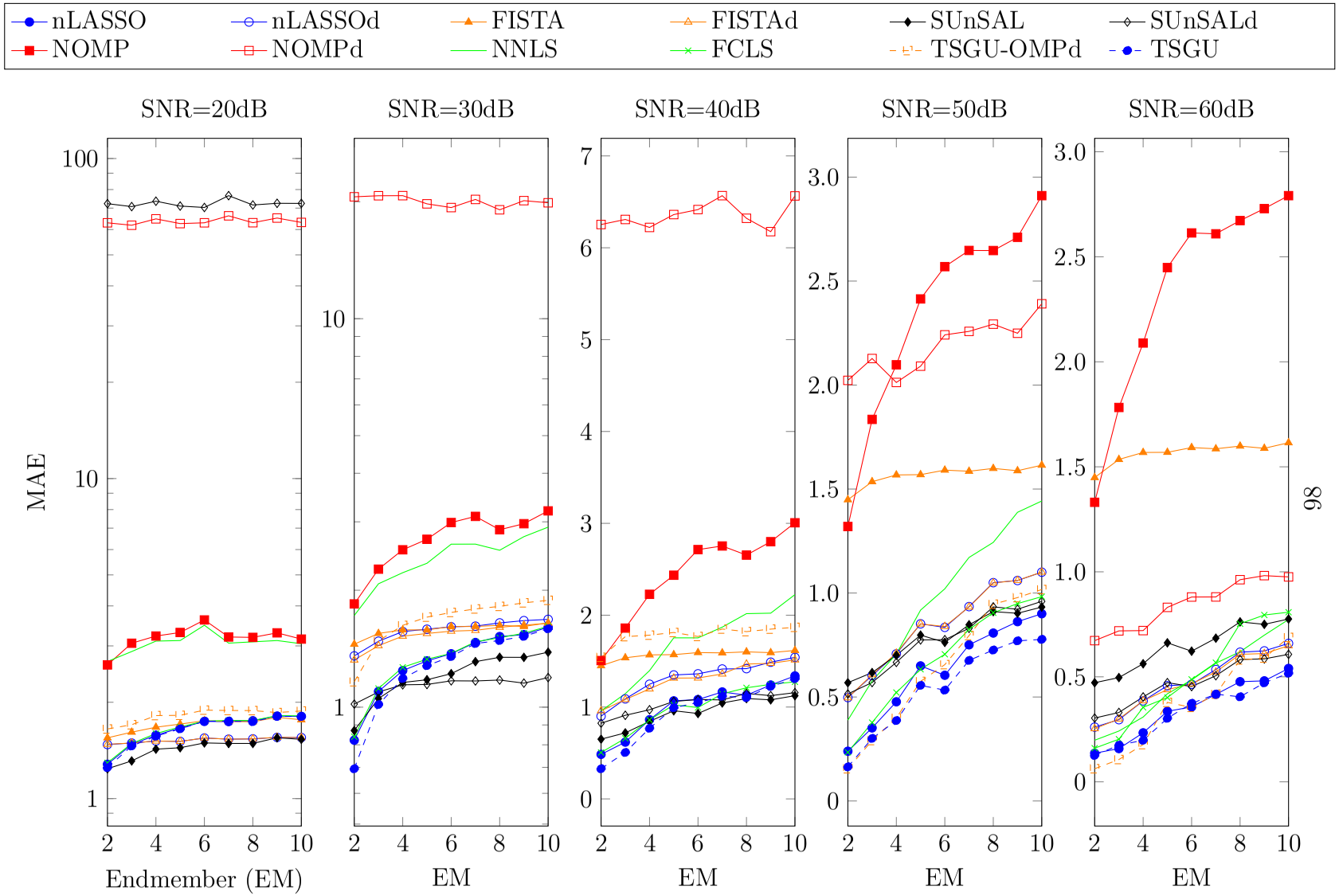

Figure 6.3: Results of abundance estimation for different SNR values. Plots present relation between the MAE measure and the number of contributing EM.

Accuracy of Endmember Detection

The ACC of endmember detection, depending on the number of mixed spectra in the ground truth and the SNR value is plotted in Figure 6.4. All algorithms except FISTA exibit high values of ACC ranging from 0.93 for spectra mixed of 10 pure spectra to 0.98 for mixtures of only two endmembers. The ACC appears to remain similar for all SNR values. The FISTA algorithm exhibits the worst accuracy ranging form 0.64 to 0.93. However, the FISTAd algorithm exhibits similar ACC values to other algorithms, where as for SNR=20dB it has the highest ACC along with the nLASSOd algorithm. Algorithms TSGU and TSGU-NOMPd for all SNR are among the three with the highest ACC.

Figure 6.5 shows the relation of the SNT and number of mixtures in the ground truth for test cases with SNR values from 20dB to 60dB. For the test scenario with low SNR=20dB all algorithms were able to detect only less than a half of the endmembers with FISTA having the highest SNT values. For SNRs 30dB and 40dB besides FISTA the algorithms TSGU, nLASSO and FCLS show the highest SNT. Algorithms nLASSO and NNLS performed the best for scenarios with high SNRs of 50dB and 60dB. Using the SNT measure shows that the detection of the endmembers drastically decreases with the increase of number of mixed endmembers. E.g. in the test case with SNR of 40dB using TSGU lagorithm the SNT is of 0.98 for mixture of 2 endmembers and it decreases to 0.47 for the mixture of 10 endmembers.

Considering the SPC measure (Figure 6.6) it is clear that the all sparse unmixing algorithms except FISTA outperformed NNLS with setting values to zero. While LASSO has similar SPC as FCLS, TSGU and TSGU-OMPd perform better for all test cases and number of mixtures.

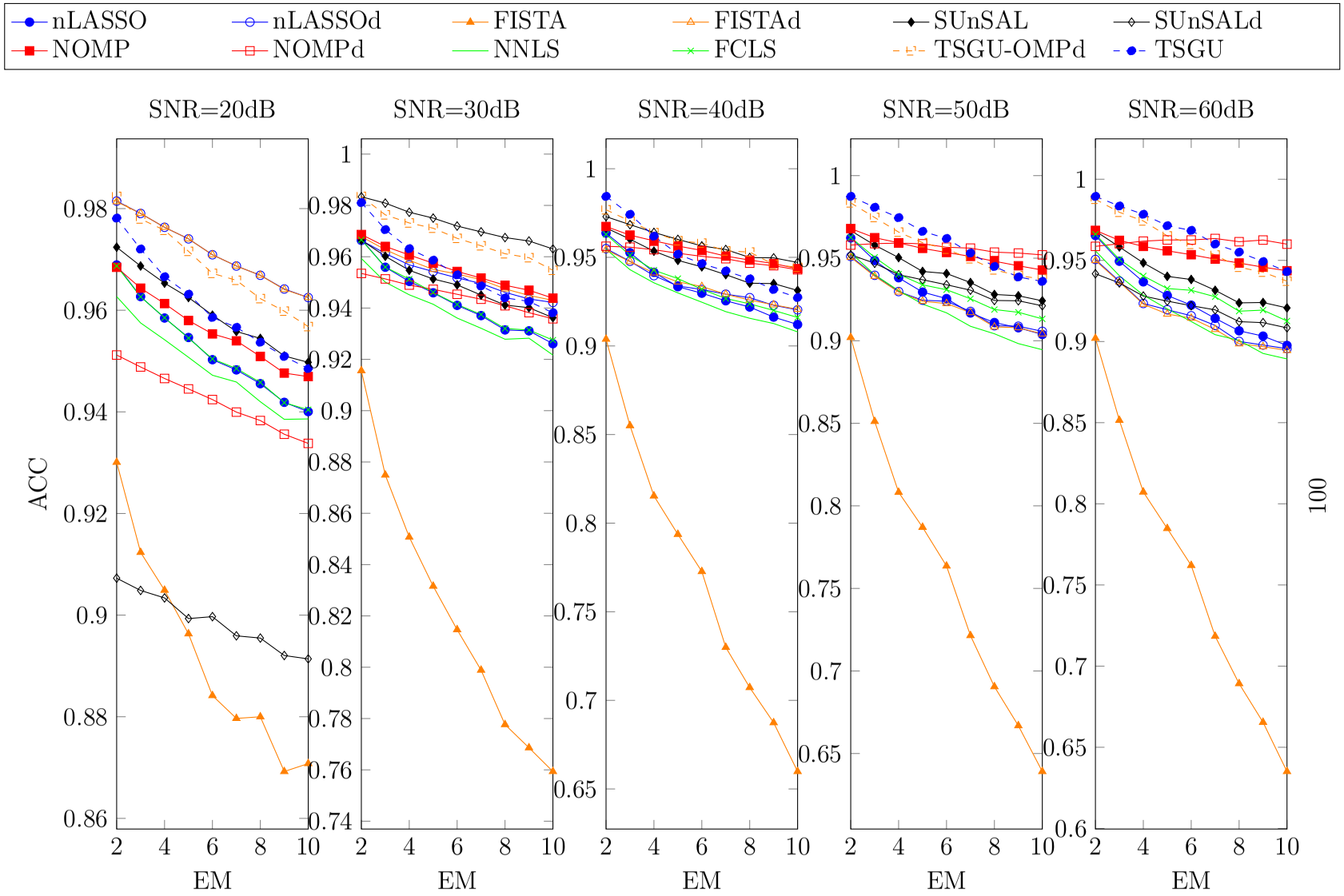

Figure 6.4: Results of abundance estimation for different SNR values. Plots present relation between the ACC measure and the number of contributing EM.

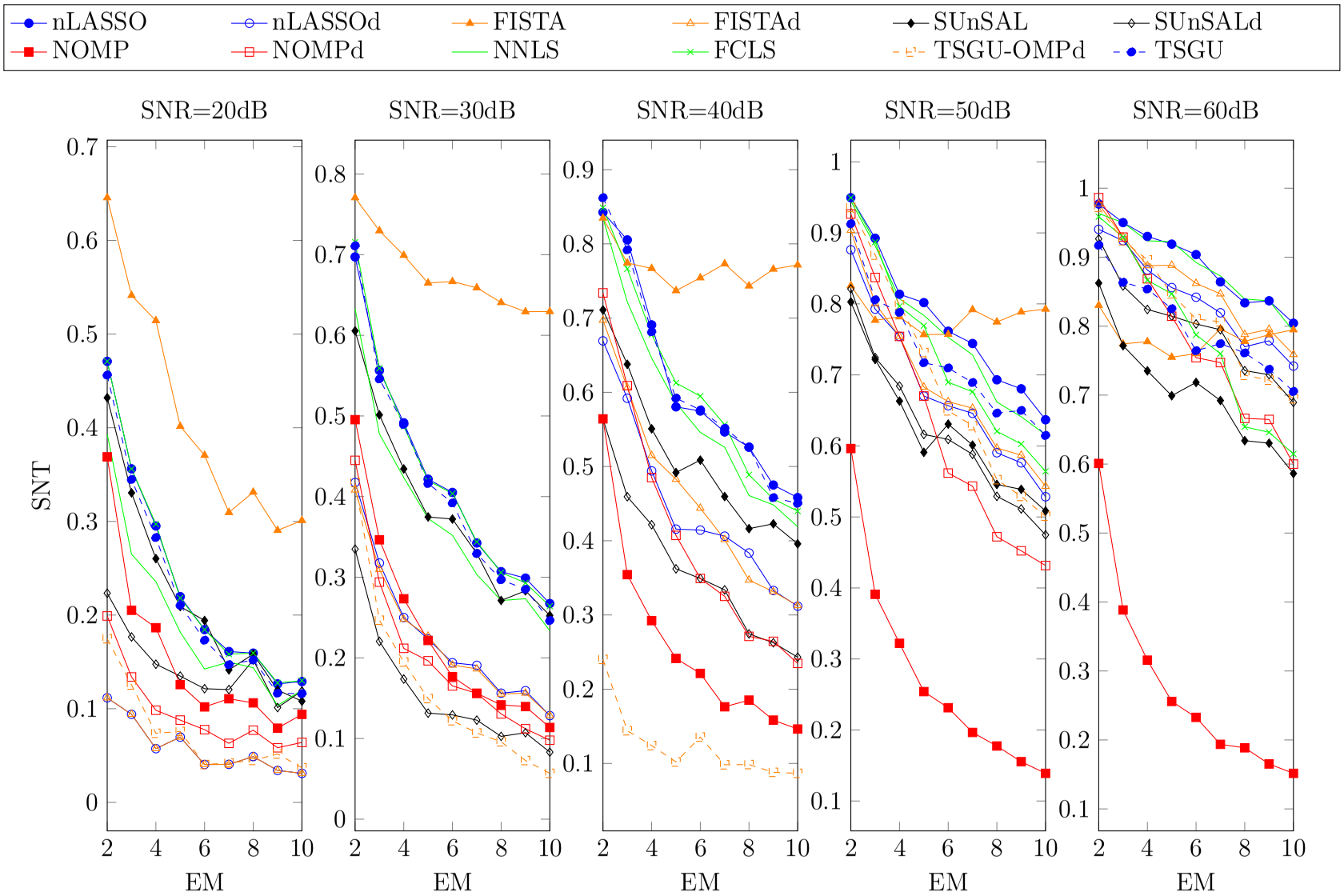

Figure 6.5: Results of abundance estimation for different SNR values. Plots present relation between the SNT measure and the number of contributing EM.

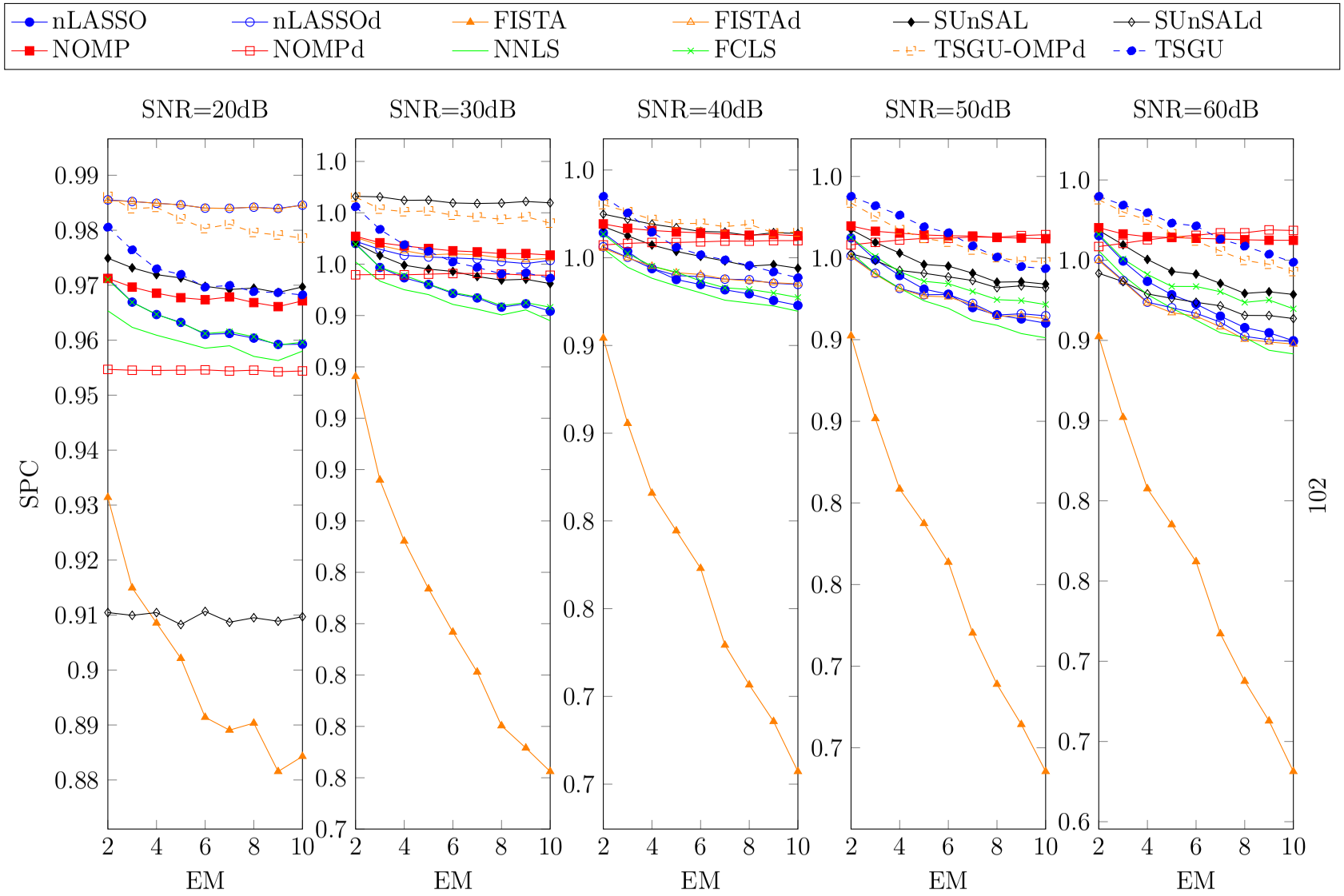

Figure 6.6: Results of abundance estimation for different SNR values. Plots present relation between the SPC measure and the number of contributing EM.

6.3 Spatial Unmixing

The proposed MLJSM algorithm has been tested using simulated and real hyperspectral data. The algorithm LARS/LASSO used for the optimization problems BPDN and MLJSR is reported in Mairal et al. (2010). Two sliding windows for MLJSR were considered, namely, a square-shaped (with J = 9) and a cross-shaped (with J = 5) window. For both, the unmixed pixel y_j was located in the center of the window. Additionally the results were compared with the SUnSAL-TV algorithm using the solver from Bioucas-Dias (2012).

6.3.1 Experiment Settings

In this experiment, n=240 spectra selected from the USGS Digital Spectral Library (splib06) Clark et al. (2007) were used to form the dictionary $A \in \mathbb{R}^{[m \times n]}$ with $m = 224$ spectral channels like in Iordache et al. (2012b). The simulated images were created as follows:

1. form a mixing matrix $M \in \mathbb{R}^{[m \times n']}$ by selecting n'=10 endmembers at random from A,
2. create an abundance cube $X'(c, r, n')$, where columns c and rows r are c=r=100. For all layers n' set randomly 144 elements to 1,
3. blur all layers n' using gaussian filter with standard deviation $\sigma = 0.025$,
4. normalize $\forall c, r, n' : X'(c, r, n') = \frac{X'(c,r,n')}{\sum_n X'(c,r,n')}$,
5. create a hyperspectral data cube $Y'(c, r, m)$ by means of LMM $\forall c, r : Y'(c, r, m) = MX'(c, r, n') + \varepsilon'(c, r, m)$, where $\varepsilon'(c, r, m)$ is gaussian noise with a signal-to-noise ratio $\text{SREdB} = 10\log_{10}\|Y'(c, r, m)\|_2^2 / \|\varepsilon'(c, r, m)\|_2^2$

In simulations four test cases with SRE values of 20, 30, 40 and 50 dB were considered [Figure 6.7(a)-(h)]. The simulated images contained mixtures from two to ten endmembers distributed as shown in Figure 6.7(i).

For each test case the solutions were calculated using NNLS, nLASSO, SUnSAL-TV and MLJSR with sixty uniformly distributed γ parameter settings such that, $\gamma = e^i, i \in \langle -1, 11 \rangle$. Additionally, since SUnSAL-TV requires two regularization parameters, we have tested the second parameter λ_{TV}(Iordache et al., 2013) with values 0.0001, 0.0005, 0.001, 0.005, 0.01 and 0.05 resulting in 360 different parameters settings for each test case.

6.3.2 Results and Discussion

Global Errors

Figure 6.8 shows the A-MSE for different γ settings using the MLJSR, nLASSO and SUnSAL-TV methods. In this particular case, MLJSR exhibits better performance than nLASSO and SUnSAL-TV. In Figure 6.9 the mean A-MSE, MAE and R-MSE are shown as a function of SNR. For all A-MSE values γ parameter has been chosen from the set of solutions so as to favour each particular algorithm (see for example Figure 6.8). In terms of A-MSE, both settings of MLJSR algorithm outperformed NNLS and nLASSO at all noise levels. MLJSR with J=9 window is reported to have lower MAE than SUnSAL-TV for low SNR 20dB and 30dB values and lower A-MSE for SNR 30dB and 50dB. In sense of R-MSE all algorithms performed very similarly. Only for the case with SNR 20dB NNLS shows lower R-MSE than SUnSAL-TV, both MLJSR versions and LASSO, respectively.

Local Errors

To evaluate the accuracy of abundance estimation the A-MSE and MAE were calculated at pixel level for whole abundance vectors. Figure 6.10 shows the A-MSE of the estimated abundance vectors using different algorithms. The ℓ_1 regularized algorithms outperform the NNLS [Figure 6.10 (r)-(u)] algorithm for all test cases. Algorithms incorporating spatial information i.e. the MLJSR [Figure 6.10 (a)-(h)] and SUnSAL-TV [Figure 6.10 (i)-(l)] significantly outperform the pixel based methods nLASSO [Figure 6.10 (m)-(p)] and NNLS. The SUnSAL-TV and both settings MLJSR perform similarly while errors having lower spatial variations. The errors produced by the MLJSR with window size $J = 9$ appear to be smaller when compared to the $j = 5$ version of the algorithm.

When considering MAE again the algorithms incorporating spatial information outperformed nLASSO and NNLS Figure 6.9. The MAE error is studied in more details in Figure 6.12 for the SNR 20dB case. The MAE was calculated at pixel level for whole abundance vectors (Figure 6.12 left column), only abundance of present endmembers (Figure 6.12 middle column), and false recovery of non-present endmembers i.e. endmembers present in recovered abundance but not present in the ground truth abundance (Figure 6.12 right column). For the 20 dB test case all ℓ_1 regularized algorithm exhibit significantly lower overall MAE than NNLS (mean MAE for the whole test image was equal 1.43 for MLJSR with J=9, 1.44 for MLJSR with J=5, 1.47 for SUnSAL-TV, 1.49 for nLASSO and 3.42 for NNLS). Both settings of MLJSR (mean MAE=0.38) along with nLASSO (mean MAE=0.34) have lower MAE for non-present endmembers when compared to SUnSAL-TV (mean MAE=0.48) and NNLS (mean MAE=2.36). All algorithms were able to recover abundances of present endmembers with relatively similar MAE.

Accuracy of Endmember Detection

The accuracy of endmember detection measures are presented on Figure 6.13. For all test cases nLASSO has the highest ACC followed by both MLJSM settings. The SUnSAL-TV algorithm exhibits significantly lower ACC when compared to other methods. On the other hand SUnSAL-TV exhibits the highest SNT and at the same time the lowest SPC what indicates that the results are not sparse i.e. there are many $\hat{x}^b(i) = 1$. When compared to nLASSO and NNLS, both settings of MLJSM have higher SNT where MLJSM with $J = 9$ is performing the best.

Visual Comparison of the Results

The results of abundance estimation of the ten contributing endmembers is shown in Figure 6.14 for the SNR 20dB test case, Figure 6.15 for the SNR 30dB test case, Figure 6.16 for the SNR 40dB test case and Figure 6.17 for the SNR 50dB test case.

The MLJSR algorithm with $J = 9$ when compared to other algorithms, seems to recover endmembers most acurately for all SNR values. The MLJSR algorithm with $J = 5$ results in slightly worse results i.e. the abundances seem to be more noisy. Hovever, it still has visually more consistent results when compared to other algorithms. E.g. the spatial details EM 1, EM 2, EM 4, EM 9 and , EM 10 were very well recovered using both MLJSR settings while results of SUnSAL-TV seem to fail in recovery of spatial details and values of many pixels are significantly different to the ground truth. Results of both NNLS and nLASSO algorithms have significant problems with recovering smooth transitions between pixels and fail in recovery of low

abundances or set abundance values to high e.g. nLASSO EM 4. For all algorithms the recovery improves with the increase of the SNR. However, for NNLS the sparsity decreases with the increase of SNR. All algorithms had problems in recovery of EM 3, EM 7 and EM 8. The algorithm MLJSR was able to detect some pixels for EM 3 and EM 7 in all SNR cases. The algorithm NNLS seems to detect all endmembers in the test case SNR 50 dB. However,the results for SNR 50dB seem to do not match the ground truth at all.

6.4 Real Data

To test the proposed algorithms and perform comparison two scenes with real hyperspectral data have been used. First, a HyMAP sensor image of an urban area is used with a dictionary containing endmembers specific to this type of area. Second, a well investigated mineralogy study area of Cuprite hills is used with a dictionary containing hundreds of mineral spectra. The scenes have been selected so to assess the algorithms in two different scenarios with different hyperspectral sensors and different libraries.

6.4.1 Hymap

In this real data experiment a hyperspectral scene acquired over Munich, Nymphenburg district, with the airborne sensor HyMap (Cocks et al., 1998) was used. The scene has a size of 100 × 100 pixels with originally 126 spectral channels reduced to 96 after discarding noisy and absorption bands. The image has been atmospherically (Richter and Schläpfer, 2011) and geometrically Müller et al. (2002) corrected with a ground resolution of 4 m. To form a spectral dictionary we used 90 man-made materials, vegetation, and soil spectra selected from the splib06 library (Clark et al., 2007), merged with

39 endmembers from a roof-material dictionary (Heiden et al., 2005). The dictionary had finally $m = 129$ endmembers.

The reconstruction of abundances by means of NNLS, OMP with $\gamma = 10$; nLASSO with $\gamma = 0.5$; TSGU; TSGU-OMPd; SUnSAL-TV with $\gamma = e^{-3}$ and $\lambda_{\text{TV}} = e^{-3}$ (Iordache et al., 2012b); and MLJSR with $\gamma = 1.5$ and $J = 9$ has been performed. Again, the regularization parameters have been chosen so as to favor each particular algorithm and thus allow for a fair comparison. All unmixing results have been overlaid on a high-resolution image (see Figure 6.18 and Figure 6.19), henceforth employed as a pseudo-ground truth. NNLS, nLASSO, SUnSAL-TV, and MLJSR, OMP, OMPd,TSGU, TSGU-OMPd have detected, respectively, 107, 22, 98, 38 114, 103, 32, 71 active materials. Fig. Figure 6.18(a)–(d), Figure 6.18(e)–(g), and Figure 6.18(h)–(k) show the estimated abundances for red roof shielding, lawn grass, and trees.

When compared with pixel based methods, the MLJSR algorithm leads to smoother transitions from one material to another, which is consistent with the assumption of localized spatial homogeneity. For example, Figure 6.18(d) shows a gradual decrease of the roof abundance from the middle of the roof towards the edges. Noticeably, this is not the case for SUnSAL-TV [Figure 6.18(d)], which tends to exhibit very similar neighboring abundances. Also, whereas nLASSO [Fig. 6.18(b)] is unable to detect the roof edges, NNLS and both versions of OMP miss a great deal of roof endmembers [Figure 6.18 and [Figure 6.19]. Moreover, they seem to provide reliable results only for abundances associated with tree spectrum [Figure 6.18(g) and Figure 6.19 (g), (h)]. Both, TSGU and TSGU-OMPd were able to detect roof endmembers and seem to provide more consistant abundance maps comparing to nLASSO and NNLS. Finally, note that, while NNLS [Fig. 6.18(i)] and nLASSO [Figure 6.18(j)] fail for grass detection, MLJSR provides satisfactory results [Figure 6.18(k)].

6.4.2 AVIRIS

As second real data set image taken over Cuprite hills in Nevada, USA acquired by the AVIRIS sensor has been used (JPL, 1997). From this image we have selected a region of 364×364 pixels with 154 out of 224 spectral bands [see Figure 6.20 (a)]. Like in experiment 6.2.1, the spectral dictionary was created using 432 selected spectra from the USGS spectral library (Clark et al., 2007). The complete list of used spectra is presented in Appendix B. For comparison the image has been unmixed using algorithms OMP, OMPd, TSGU-OMPd, nLASSO, TSGU, NNLS, MLJSM with $j = 5$ and $J = 9$.

The hyperspectral image of Cuprite hills has been studied by many researchers and therefore the geological composition is well understood. In this experiment the abundance maps of alunite (sample name 'Alunite+Dickite, MV99-6-26b, s06av95a=c'), buddingstone (sample name 'Buddingtonite, NHB2301, s06av95a=b'), kaolinite (sample name 'Kaolin/Smect, KLF511, .12Kaol, s06av95a=b') and playa (sample name 'Stonewall_ Playa, CU93-52A, a11, s06av95a=a') are investigated. The presence of these materials has been confirmed by researchers (Clark et al., 2003; Swayze et al., 2014) and is marked in Figure 6.20 (b).

Figure 6.21 presents resulting abundance maps of alunnotite for all tested algorithms. The area in which the alunite is reported to occur is zoomed in. All algorithms except OMP detect abundance of alunite. The algorithms nLASSO, TSGU, NNLS the results in very similar abundance maps. MLJSM in both settings results in significantly smoother transitions between abundance values and appears to be less noisy. The derivative method OMPd has improved the abundance detection when compared to OMP. However, the abundance map appears to be incomplete when compared to results of other algorithms. As a result of the pour results of OMPd, the TSGU-OMPd also seems to perform worse but the detected pixels have more similar abundance

values to other algorithms.

Buddingstone has been reported to be present in the image in the highest concentration in the center of the image east from the route 95 [see Figure 6.20 (b)]. The results of abundance estimation for this mineral are shown in Figure 6.22. The OMP algorithm detects only one pixel containing buddingstone while OMPd shows more abundance of buddingstone for some pixels. Comparing to both OMP and OMPd, TSGU-OMPd seems to improve the detection of pixels with lower buddingstone abundance. All other algorithms result in very similar abundances, where again MLJSM results in more smooth i.e. less noisy abundance maps.

All algorithms were able to detect kaolinite in the expected area. However the values of the abundance vary strongly. The OMP reports the highest values with many abundances over 1. Additionally, the abundances differ significantly to all other algorithms. The OMPd algorithm and TSGU-OMPd have lover abundances and are more comparable to results of other algorithms. The abundance of kaolinite recovered by the MLJSM with $J = 9$ reports more pixels in which kaolinite has been found comparing to the $J = 5$ version. Both versions of the algorithms have less variations in neighbouring bixels than other algorithms.

In Figure 6.24 the result for the playa is shown. Out of all tested algorithms only OMPd and TSGU-OMPd exibit abundance for this mineral in the area where it has been reported to occur. semilogy

6.5 Execution Time

To perform execution time comparison the simulated hyperspectral image from section 6.3.1 with SNR of 30dB is used. The tested algorithms were

executed with settings resulting in lowest A-MSE. To allow fair comparison all algorithms were run in Matlab 7b on Intel(R) Core(TM) i5-2520M CPU @ 2.50GHz processor with 8GB of RAM using algorithms reported in (Bioucas-Dias, 2012; Mairal et al., 2010) as well as Matlab build in functions.

The results of the execution time comparison is shown in Figure 6.25. All pixel based sparse regularised methods converge significantly faster than the NNLS. The FCLS performs worst out of all algorithms needing over 20000 seconds. The ℓ_0 regularized method NOMP and NOMPd performed the fastest with 0.01 second for the whole dataset. nLASSOd was the fastest out of all ℓ_1 regularised algorithms, 0.09 seconds followed by the nLASSO algorithm, 0.53 seconds. Both algorithms with preselection step TSGU and TSGU-OMP performed slower than NOMP or nLASSO but were still significantly faster than conventional approaches. SUnSAL was the slowest algorithm out of the pixel based sparse regularized methods.

The spatial spectral unmixing methods are generally slower than the pixel based unmixing. However, MLJSR with $J = 5$ outperforms some pixel based sparse unmixing methods like TSGU-OMPd or SUnSAL. Both settings of MLJSR converge significantly faster than SUnSAL-TV, FCLS or NNLS.

6.6 Summary

This chapter provided critical evaluation of the traditional, state-of-the-art and proposed methods to perform spectral unmixing using large spectral dictionaries. Following is the summary of results presented in this chapter:

- **Pixel-based unmixing**
  It has been shown that sparse spectral unmixing exhibit better results than the standard NNLS approach using different performance measures. Also, it exhibit similar results to FCLS with the execution time reduced by several orders of magnitude. It is important to note that

the LASSO algorithm provides similar results to the SUnSAL algorithm which has been dedicated for spectral unmixing. Additionally the application of the derivative method significantly decreases errors in unmixing when using OMP or FISTA algorithms which are known to be sensitive to correlations in the dictionary. The proposed TSGU algorithm was able to achieve better results than the LASSO while TSGU-OMPd is of advantage over the OMP algorithm. When looking at real data both versions of TSGU algorithms provide reasonable results abd qualitatively detect endmembers more correctly than others. Moreover, TSGU and TSGU-OMPd where the only of the tested algorithms to recover the playa abundance in the Cuprite image.

- **Spatial-Spectral unmixing**
  The use of spatial information for unmixing significantly increases the quality of unmixing results. Compared to the standard sparse nLASSO or NNLS methods, experiments with simulated data demonstrate that the proposed method restores abundances for pixels sharing common endmembers more accurately in terms of the SRE measure and overall MAE. Compared to the SUnSAL method the proposed approach exhibited higher SRE for SNR equal 20 and 30 dB. The fact that the MLJSR method requires only one regularization parameter, shows it is easier to use compared to SUnSAL-TV. Additionally MLJSR in both settings performs faster than SUnSAL-TV, FCLS or NNLS. The outcome of MAE comparison shows that the MLJSR approach recovers endmembers with similar accuracy as state of the art algorithms with low detection of non-present endmembers. The qualitative analysis of the results for the HyMAP image shows the MLJSR approach to be competitive with respect to nLASSO and NNLS or SUnSAL-TV methods and provides visually more consistent results.

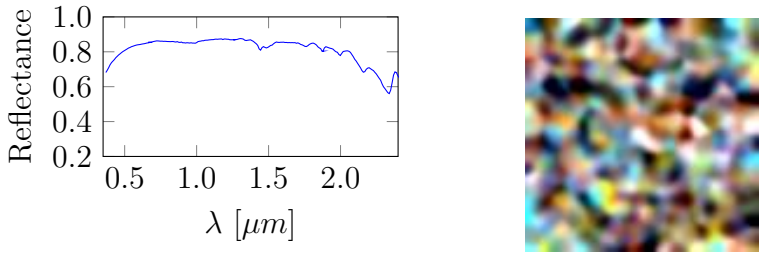

(a) no noise

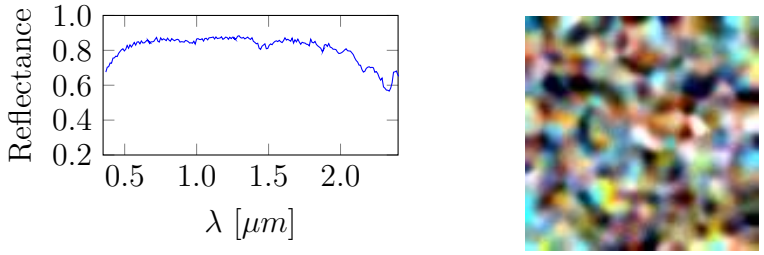

(b) 40dB

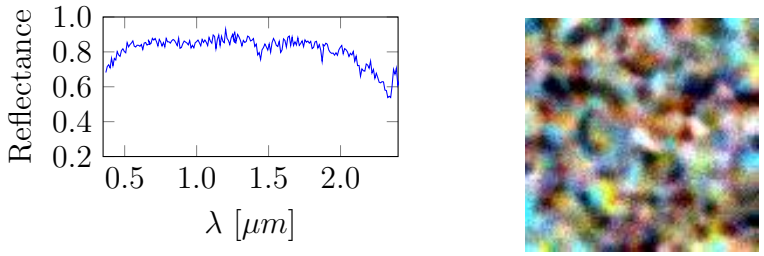

(c) 30dB

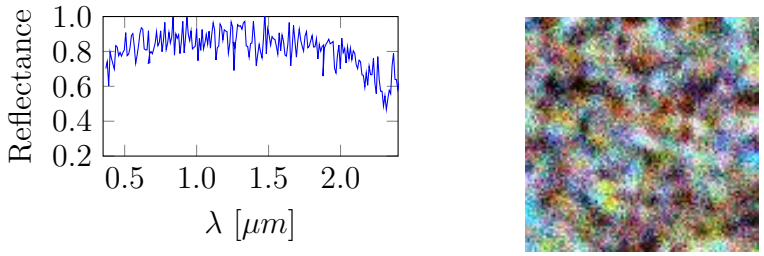

(d) 20dB

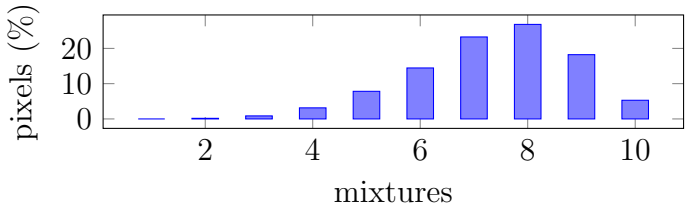

(e)

Figure 6.7: Simulated data. Subfigures (a)-(d) present a central pixel spectrum from the simulated image (left plot) and the false color composition of bands 50, 100, 150 (on the right) with no noise (a) and with SNR of 40dB (b), 30dB (c) and 20dB (d). The bar plot (e) shows the distribution of pixels according to the number of endmembers mixed in it.

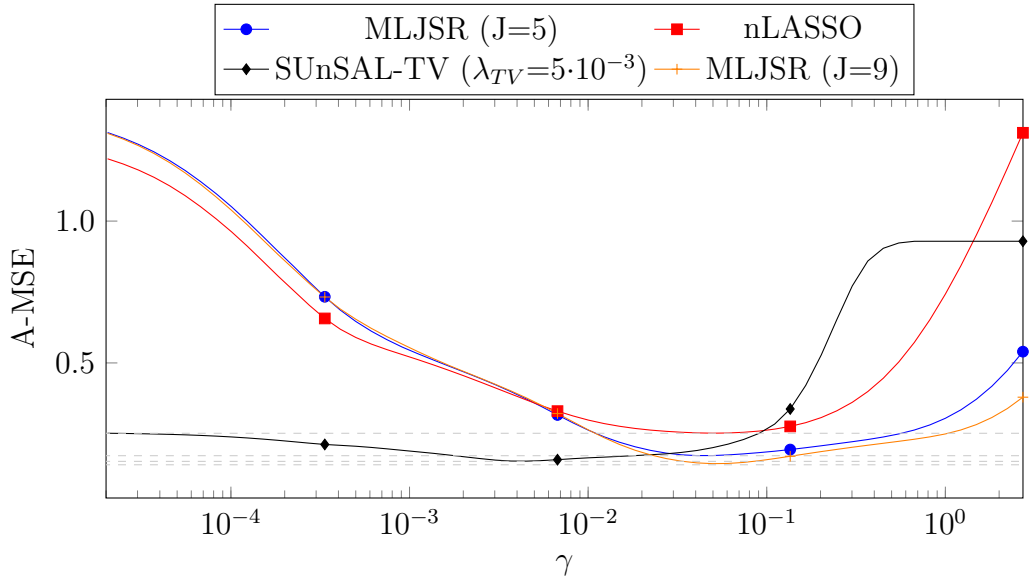

Figure 6.8: Plot of the A-MSE values as a function of γ regularization parameter. Results for SNR = 30 dB using nLASSO, SUnSAL-TV and MLJSR methods.

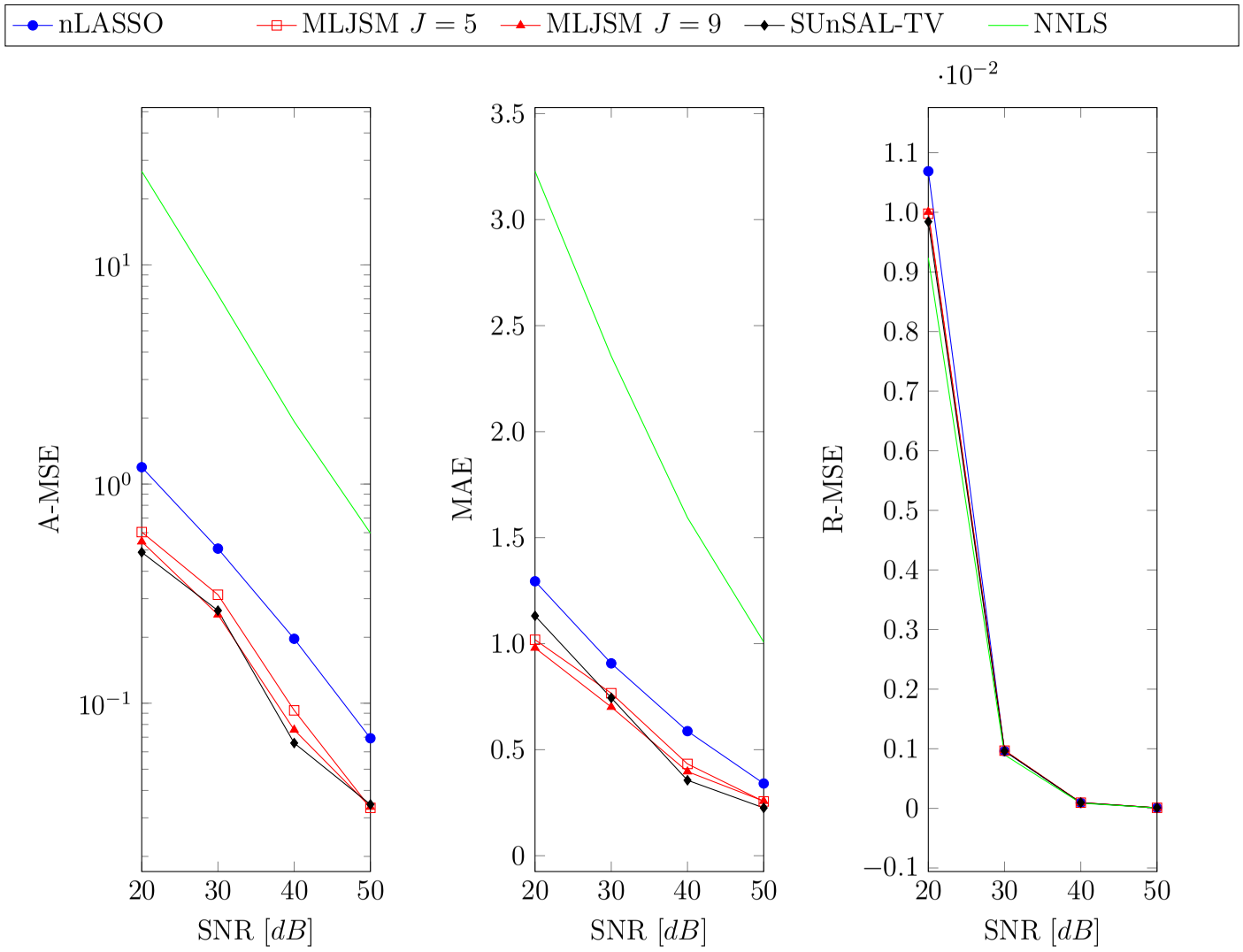

Figure 6.9: Plots of mean errors for datasets witch different SNR. From left to right A-MSE, MAE and R-MSE.

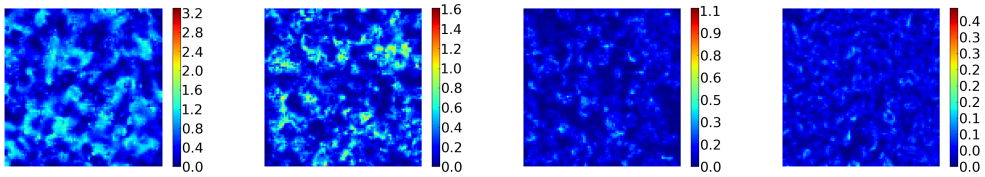

(a) MLJSR (J=9) SNR = 20 dB (b) MLJSR (J=9) SNR = 30 dB (c) MLJSR (J=9) SNR = 40 dB (d) MLJSR (J=9) SNR = 50 dB

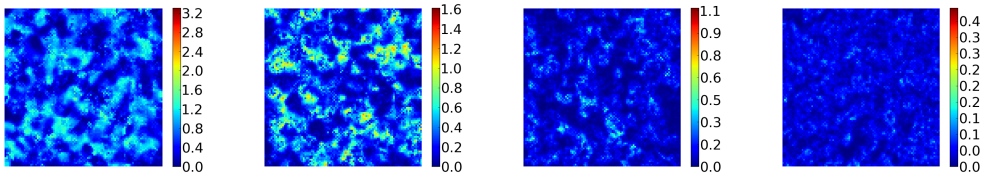

(e) MLJSR (J=5) SNR = 20 dB (f) MLJSR (J=5) SNR = 30 dB (g) MLJSR (J=5) SNR = 40 dB (h) MLJSR (J=5) SNR = 50 dB

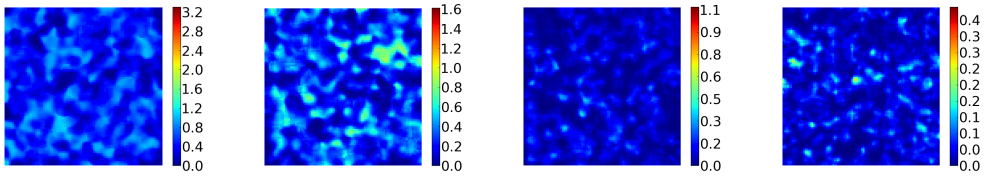

(i) SUnSAL-TV SNR = 20 dB (j) SUnSAL-TV SNR = 30 dB (k) SUnSAL-TV SNR = 40 dB (l) SUnSAL-TV SNR = 50 dB

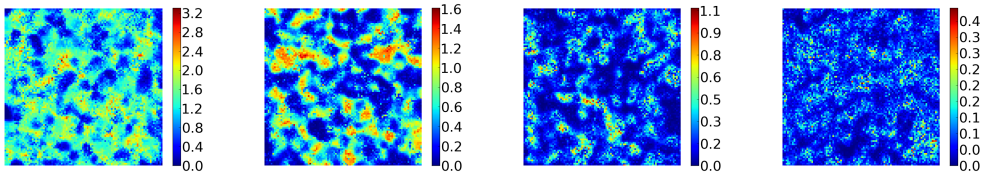

(m)nLASSO SNR = 20 dB (n)nLASSO SNR = 30 dB (o) nLASSO SNR = 40 dB (p) nLASSO SNR = 50 dB

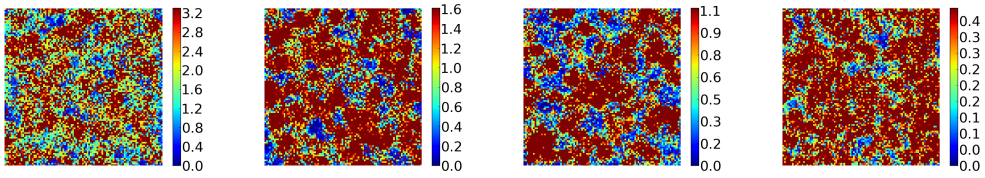

(r) NNLS SNR = 20 dB (s) NNLS SNR = 30 dB (t) NNLS SNR = 40 dB (u) NNLS SNR = 50 dB

Figure 6.10: Comparison of MLJSR(J = 9), MLJSR(J = 5), SUnSAL-TV, nLASSO and NNLS algorithms (from top to bottom respectively) using the A-MSE measure for all endmembers. Results for SNR 20dB, 30dB, 40dB and 50dB are shown from left row right. The colorbar range, for all subfigures in a row, has been set at maximum A-MSE of one of the ℓ_1 regularized methods.

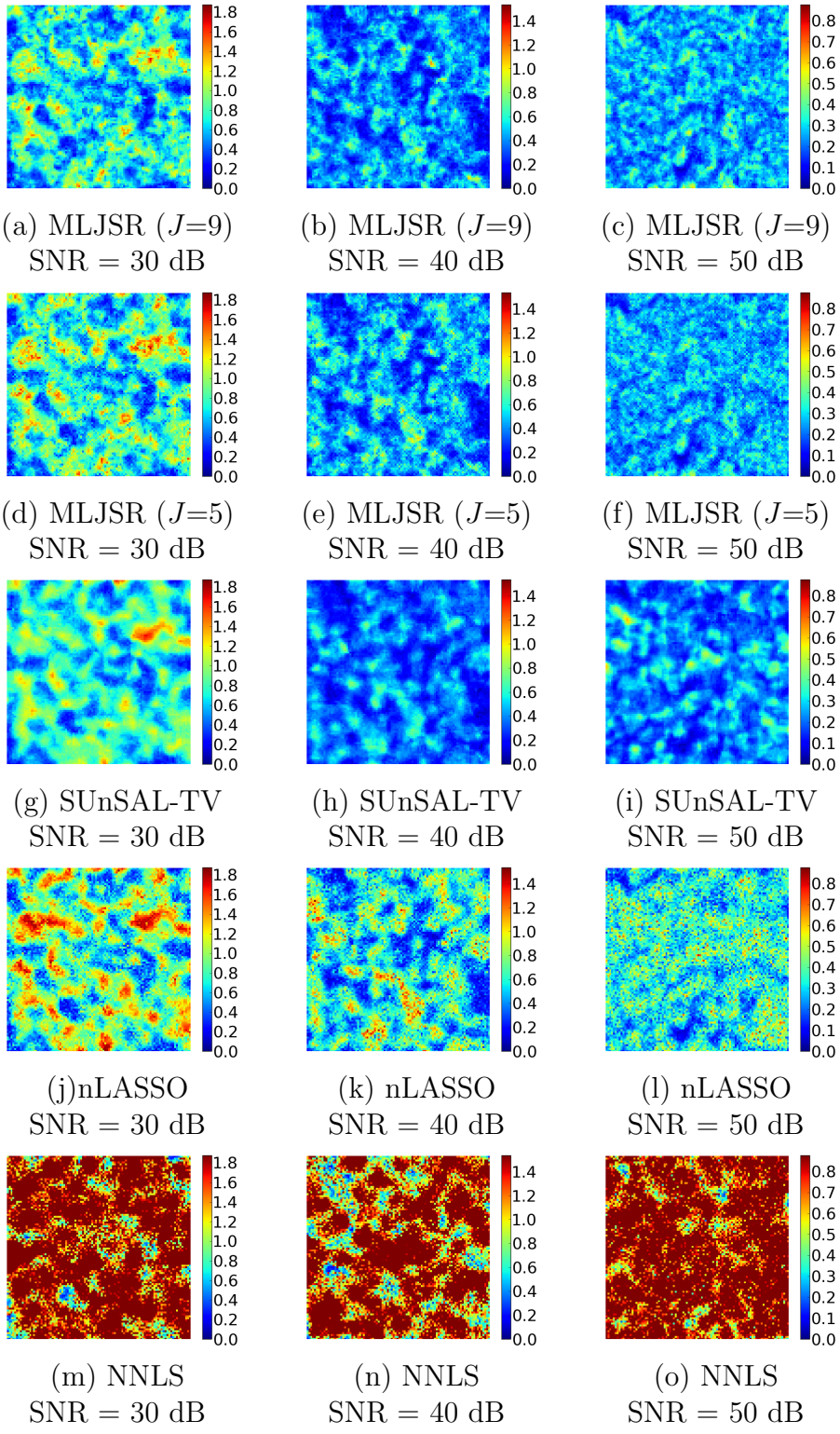

(a) MLJSR (J=9) SNR = 30 dB
(b) MLJSR (J=9) SNR = 40 dB
(c) MLJSR (J=9) SNR = 50 dB
(d) MLJSR (J=5) SNR = 30 dB
(e) MLJSR (J=5) SNR = 40 dB
(f) MLJSR (J=5) SNR = 50 dB
(g) SUnSAL-TV SNR = 30 dB
(h) SUnSAL-TV SNR = 40 dB
(i) SUnSAL-TV SNR = 50 dB
(j)nLASSO SNR = 30 dB
(k) nLASSO SNR = 40 dB
(l) nLASSO SNR = 50 dB
(m) NNLS SNR = 30 dB
(n) NNLS SNR = 40 dB
(o) NNLS SNR = 50 dB

Figure 6.11: Comparison of MLJSR(J = 9), MLJSR(J = 5), SUnSAL-TV, nLASSO and NNLS algorithms (from top to bottom respectively) using the MAE measure for all endmembers. Results for SNR 20dB, 30dB, 40dB and 50dB are shown from left ro right. The colorbar range, for all subfigures in a row, has been set at maximum mse of one of the ℓ_1 regularized methods.

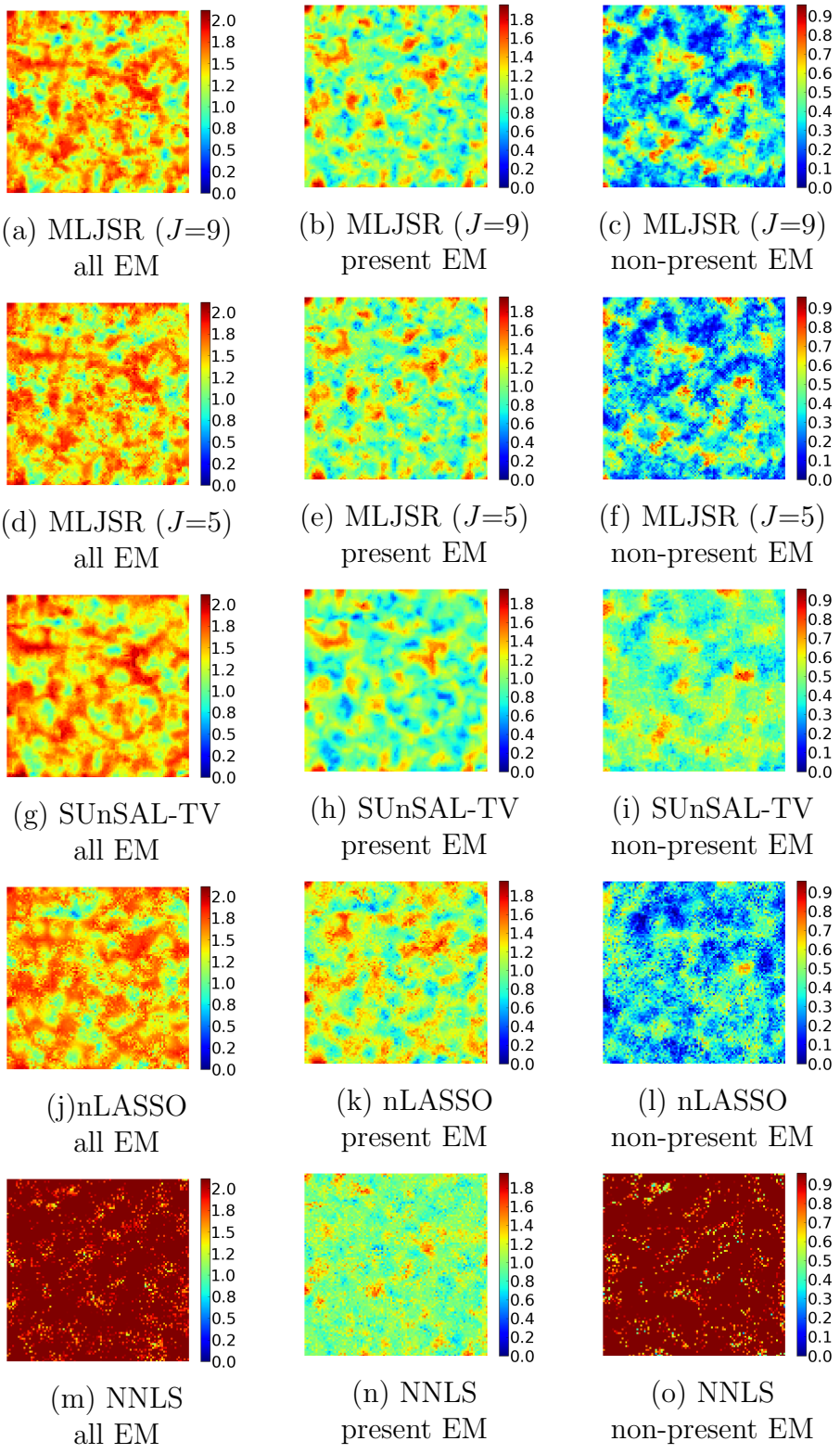

(a) MLJSR (J=9) all EM

(b) MLJSR (J=9) present EM

(c) MLJSR (J=9) non-present EM

(d) MLJSR (J=5) all EM

(e) MLJSR (J=5) present EM

(f) MLJSR (J=5) non-present EM

(g) SUnSAL-TV all EM

(h) SUnSAL-TV present EM

(i) SUnSAL-TV non-present EM

(j)nLASSO all EM

(k) nLASSO present EM

(l) nLASSO non-present EM

(m) NNLS all EM

(n) NNLS present EM

(o) NNLS non-present EM

Figure 6.12: Comparison of NNLS, nLASSO, SUnSAL-TV and MLJSR algorithms using the SRE=20 dB test case and the MAE measure for all endmembers (left column), endmembers present in the image only (middle column) and endmembers not present in the image i.e. false abundance recovery (right column). The colorbar range, for all subfigures in a row, has been set at maximum MAE of one of the ℓ_1 regularized methods.

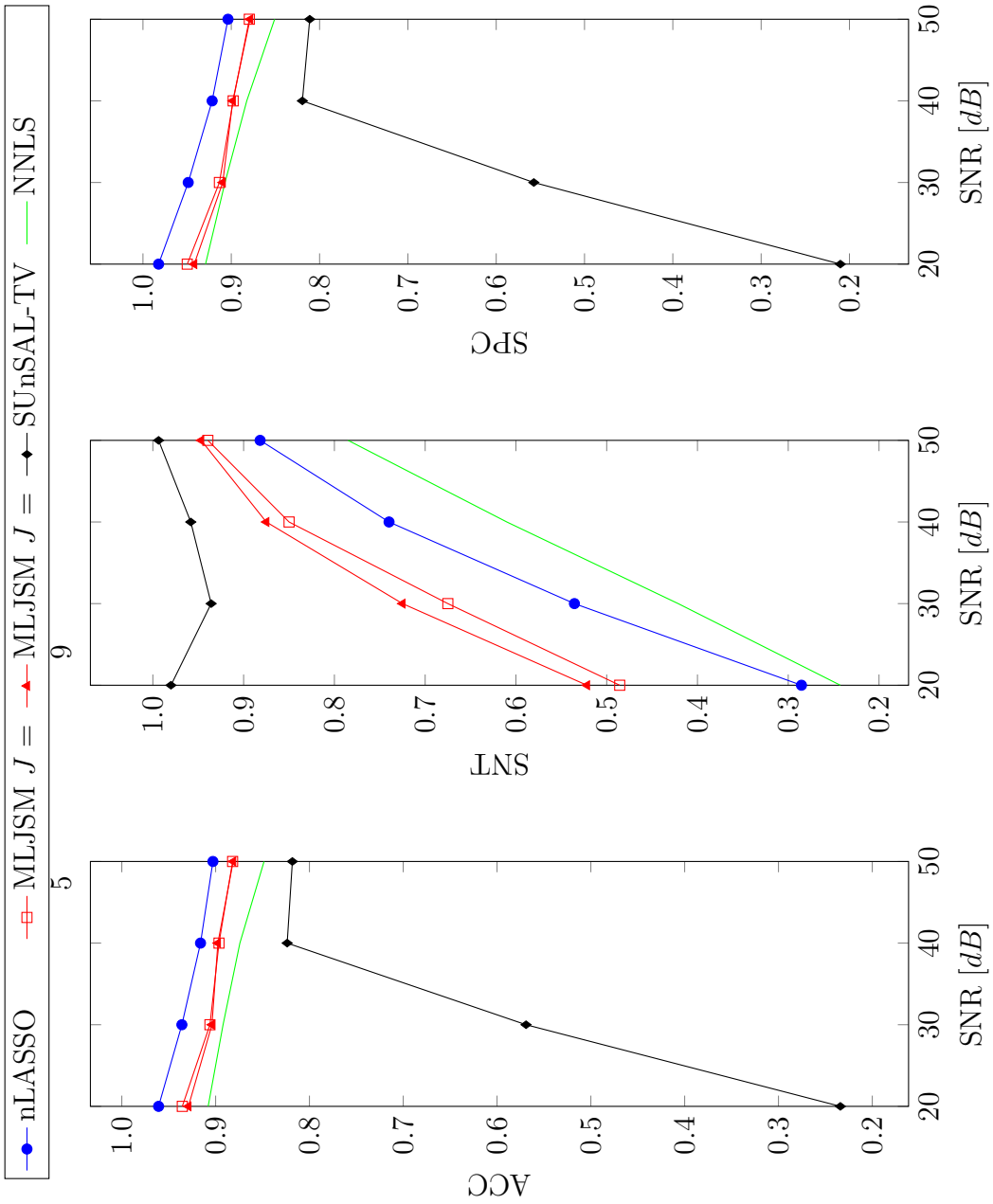

Figure 6.13: Plots of mean ACC, SNT and SPC for datasets witch different SNR.

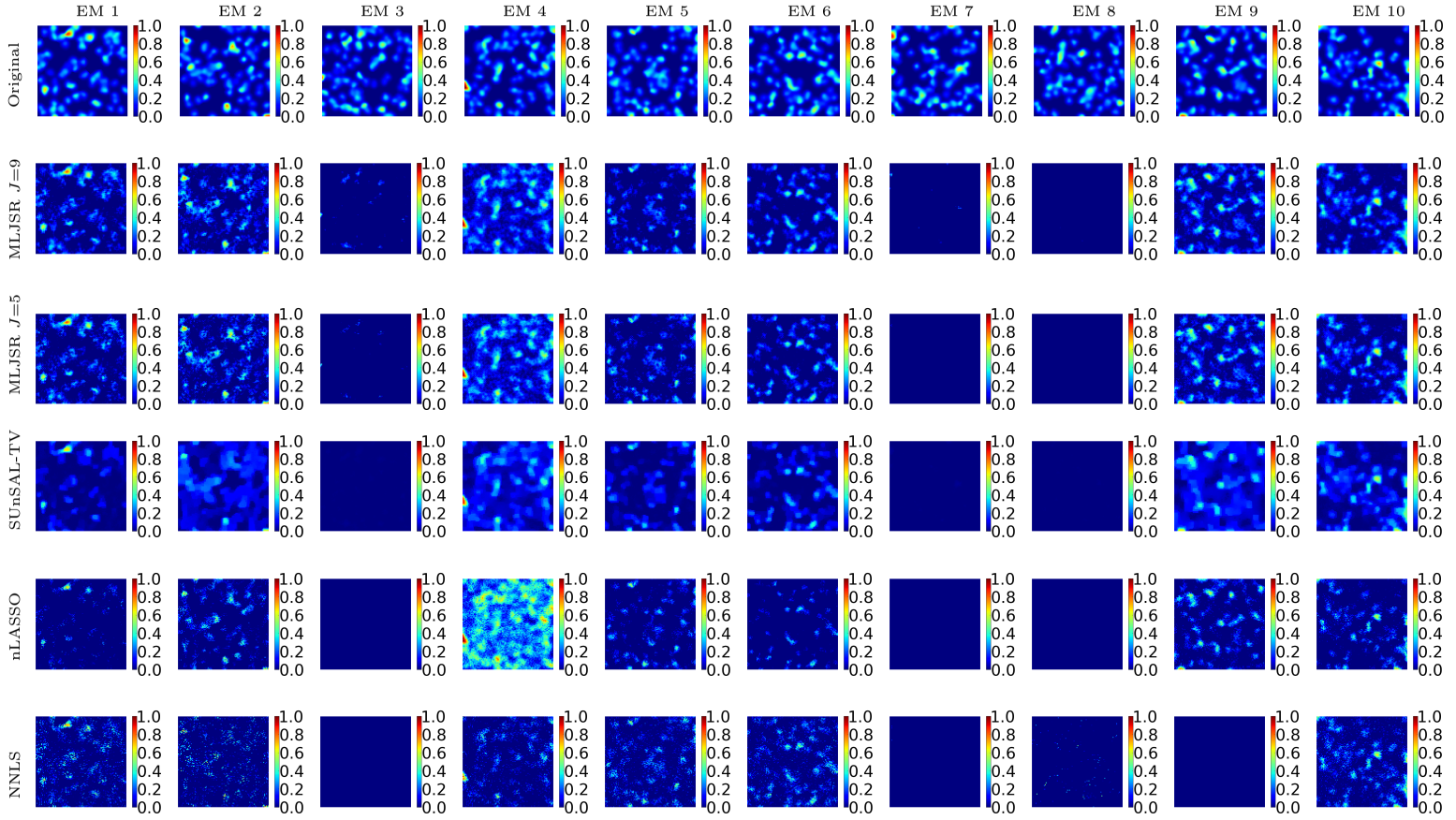

Figure 6.14: Original endmember abundances compared with estimated abundances using NNLS, nLASSO, SUnSAL-TV and MLJSR algorithms. Test case with the SNR=20dB.

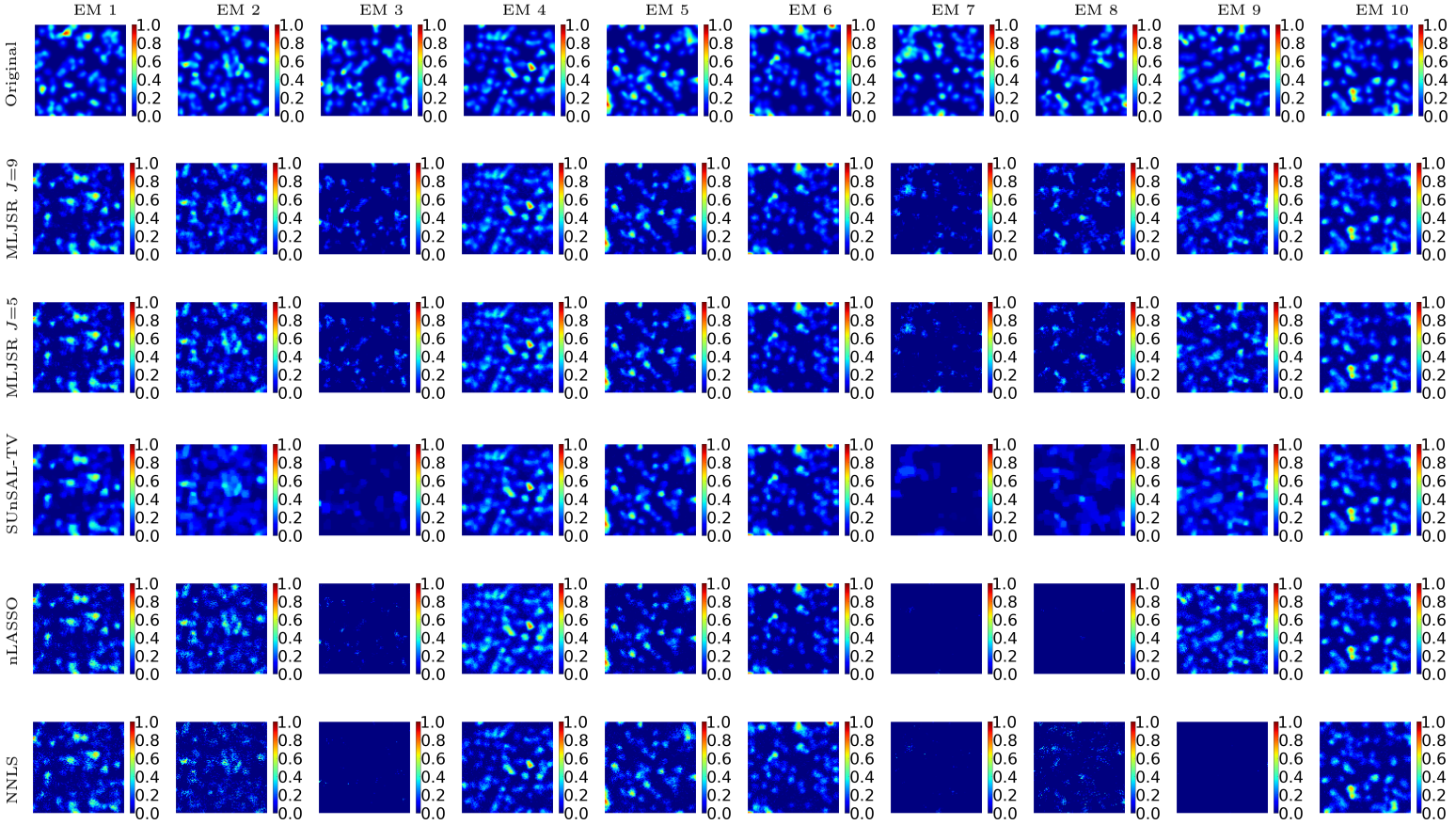

Figure 6.15: Original endmember abundances compared with estimated abundances using NNLS, nLASSO, SUnSAL-TV and MLJSR algorithms. Test case with the SNR=30dB.

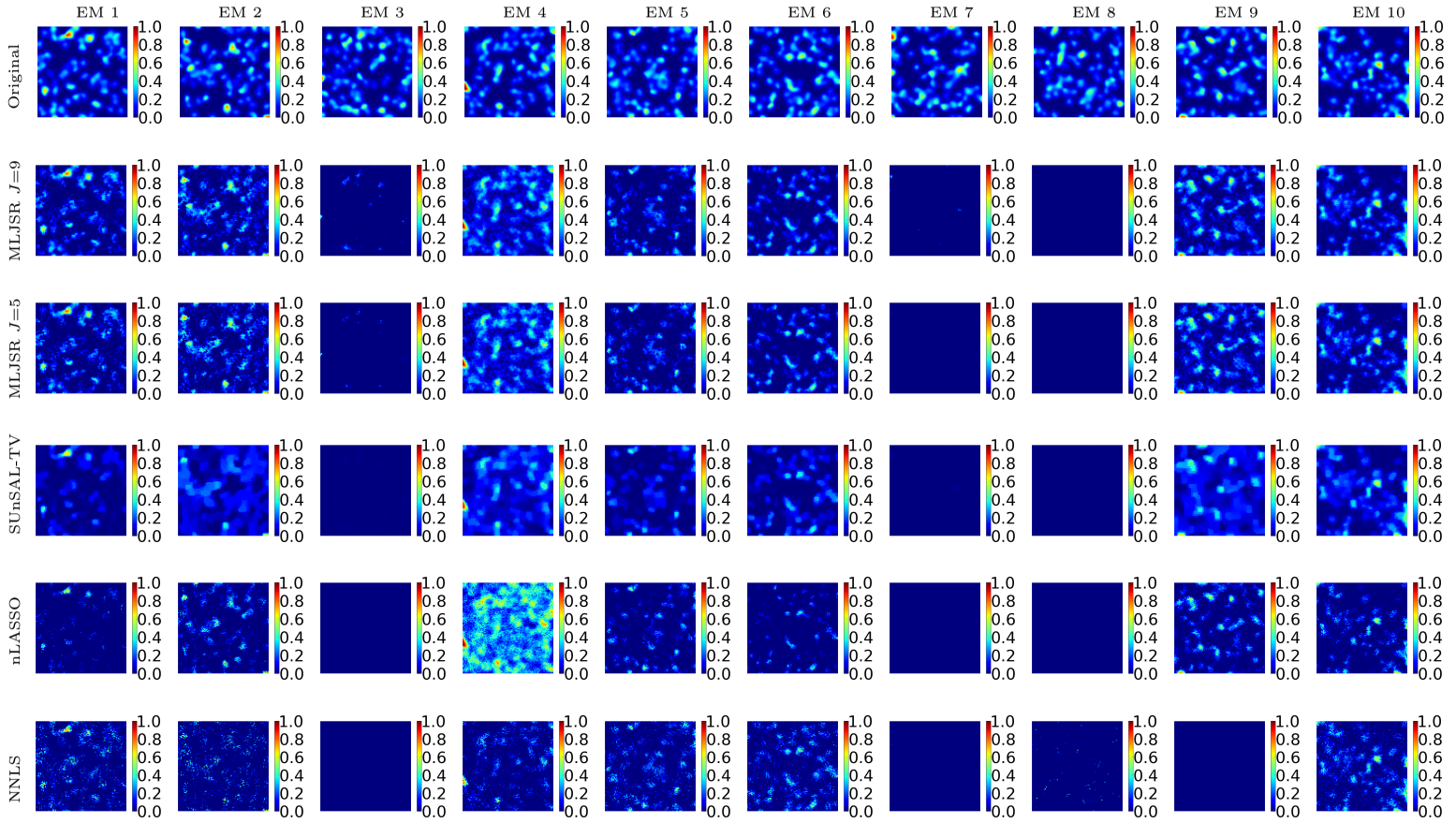

Figure 6.16: Original endmember abundances compared with estimated abundances using NNLS, nLASSO, SUnSAL-TV and MLJSR algorithms. Test case with the SNR=40dB.

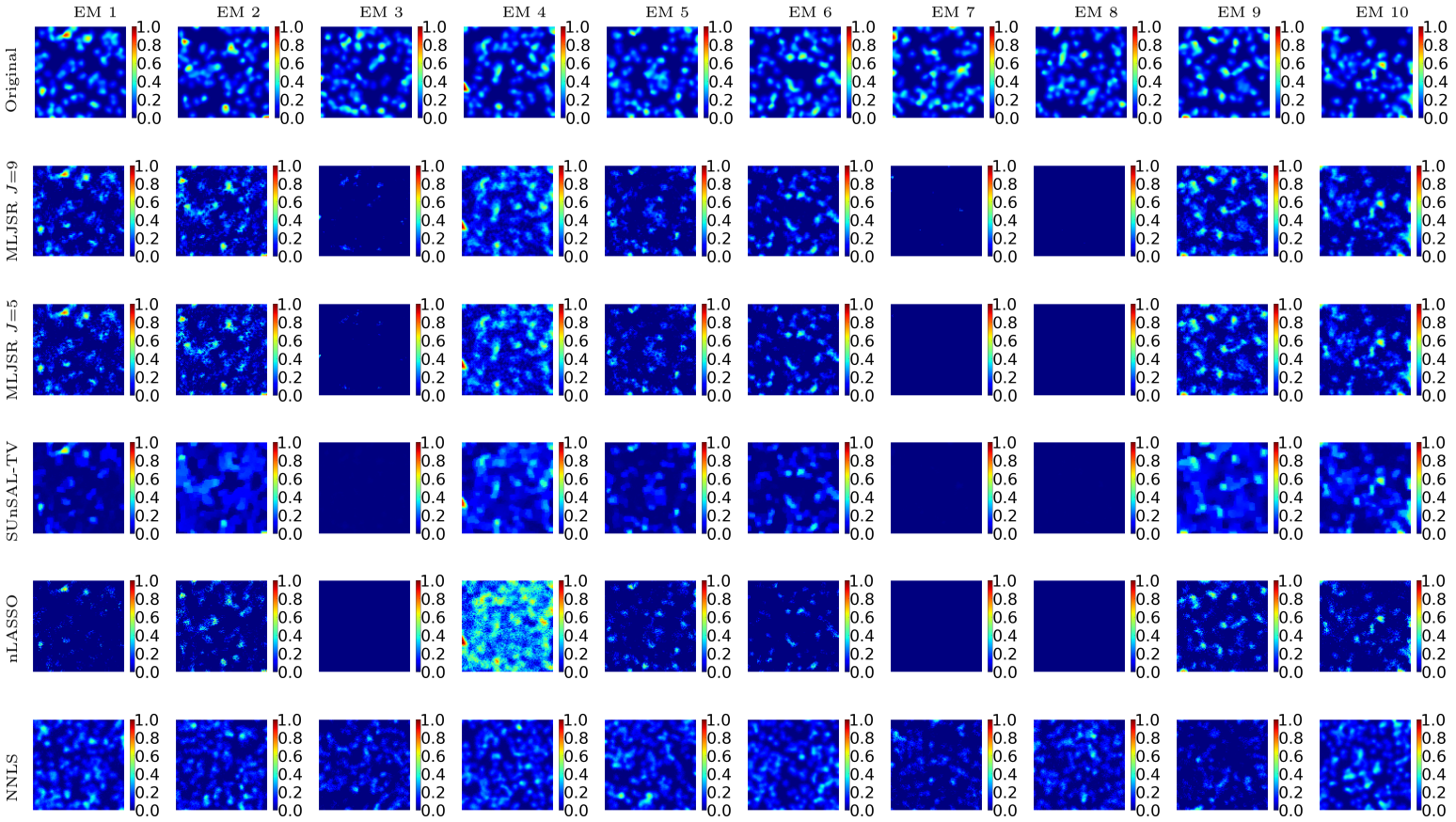

Figure 6.17: Original endmember abundances compared with estimated abundances using NNLS, nLASSO, SUnSAL-TV and MLJSR algorithms. Test case with the SNR=50dB.

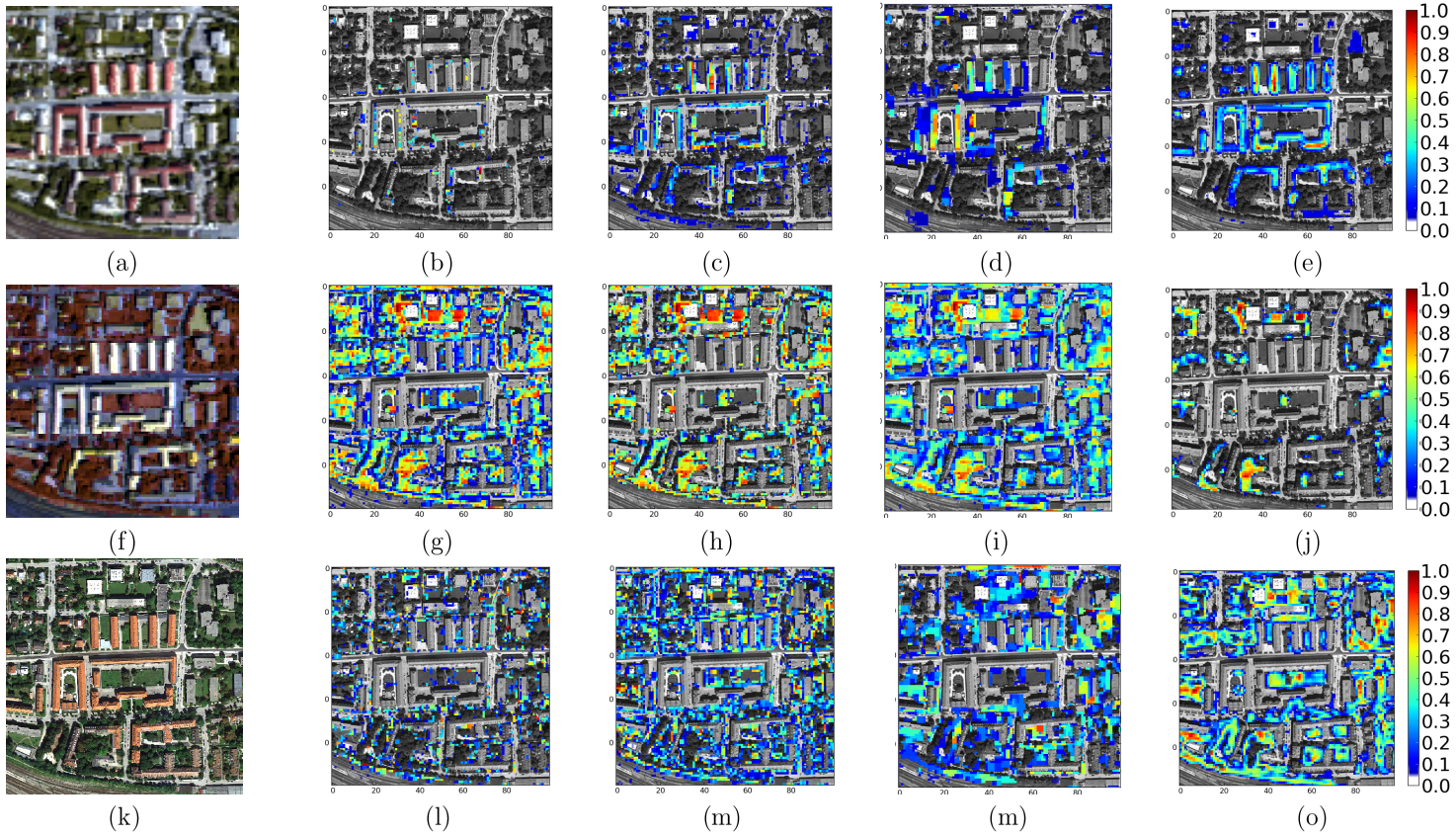

Figure 6.18: Unmixing results using NNLS [(b),(g),(l)], nLASSO [(c),(h),(m)], SUnSAL-TV [(d),(i),(m)] and MLJSR [(e),(j),(o)], respectively. First row of images presents abundance map for red roof shielding. In the second row are the abundances for tree spectrum and in third for lawn grass. (a) RGB composition (channels 7,5,3) from HyMAP image, (f) false RGB composition (channels 96,60,16), (k) high resolution ©Google Earth Image of the corresponding area.

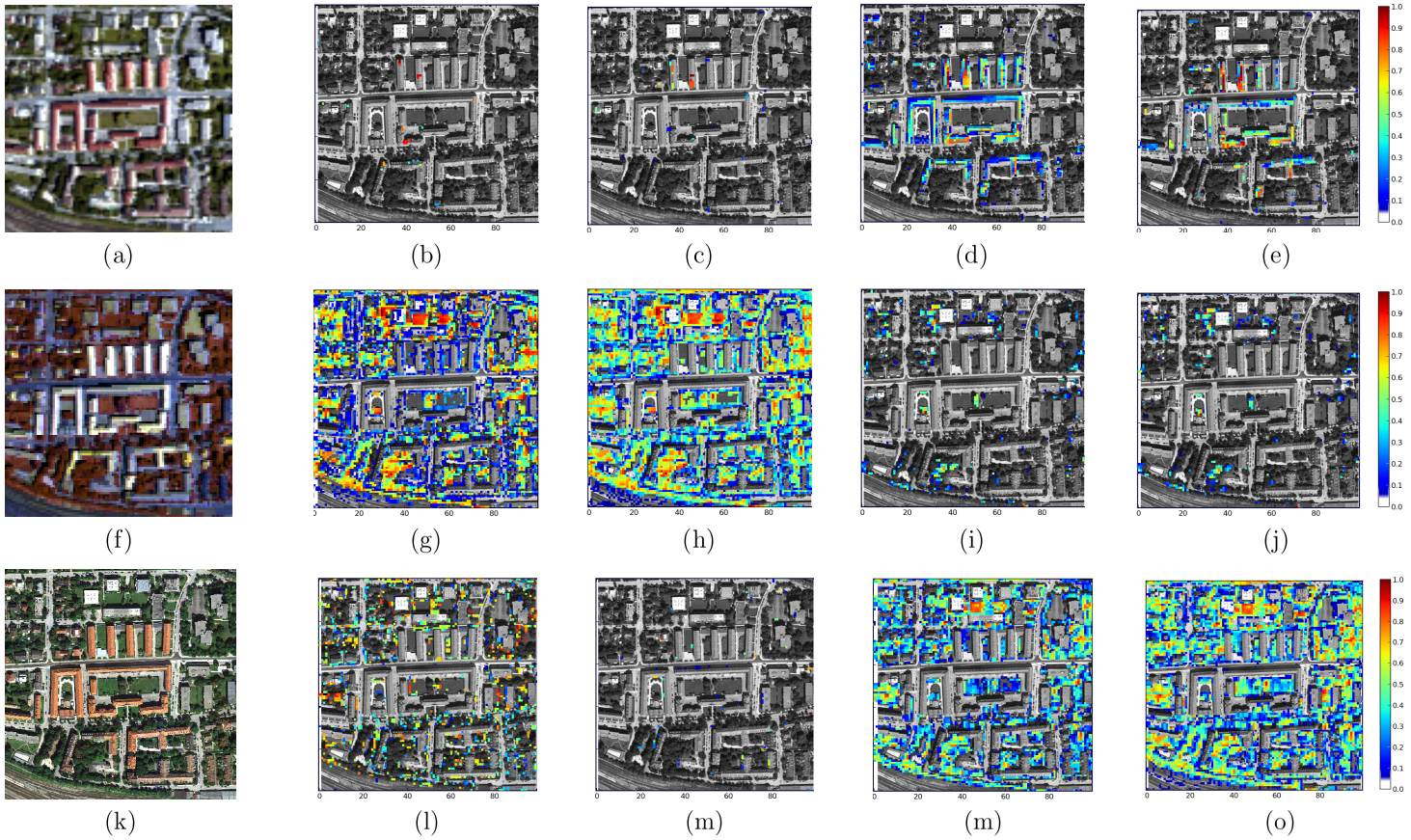

Figure 6.19: Unmixing results using OMP [(b),(g),(l)], OMPd [(c),(h),(m)], TSGU [(d),(i),(m)] and TSGU-OMPd [(e),(j),(o)], respectively. First row of images presents abundance map for red roof shielding. In the second row are the abundances for tree spectrum and in third for lawn grass. (a) RGB composition (channels 7,5,3) from HyMAP image, (f) false RGB composition (channels 96,60,16), (k) high resolution ©Google Earth Image of the corresponding area.

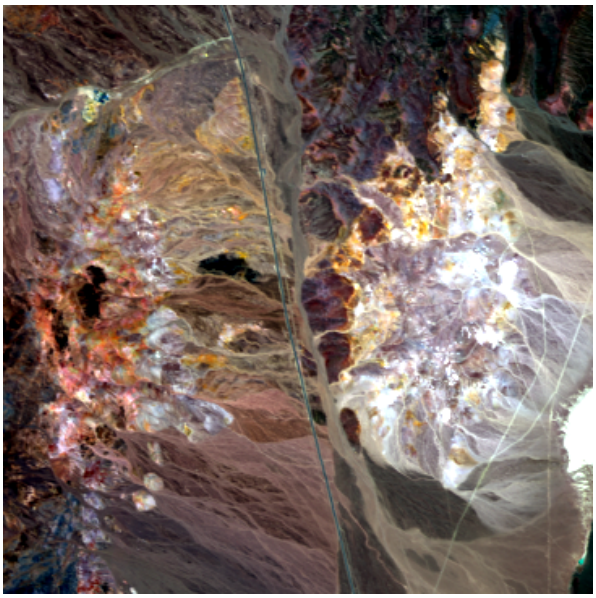

(a)

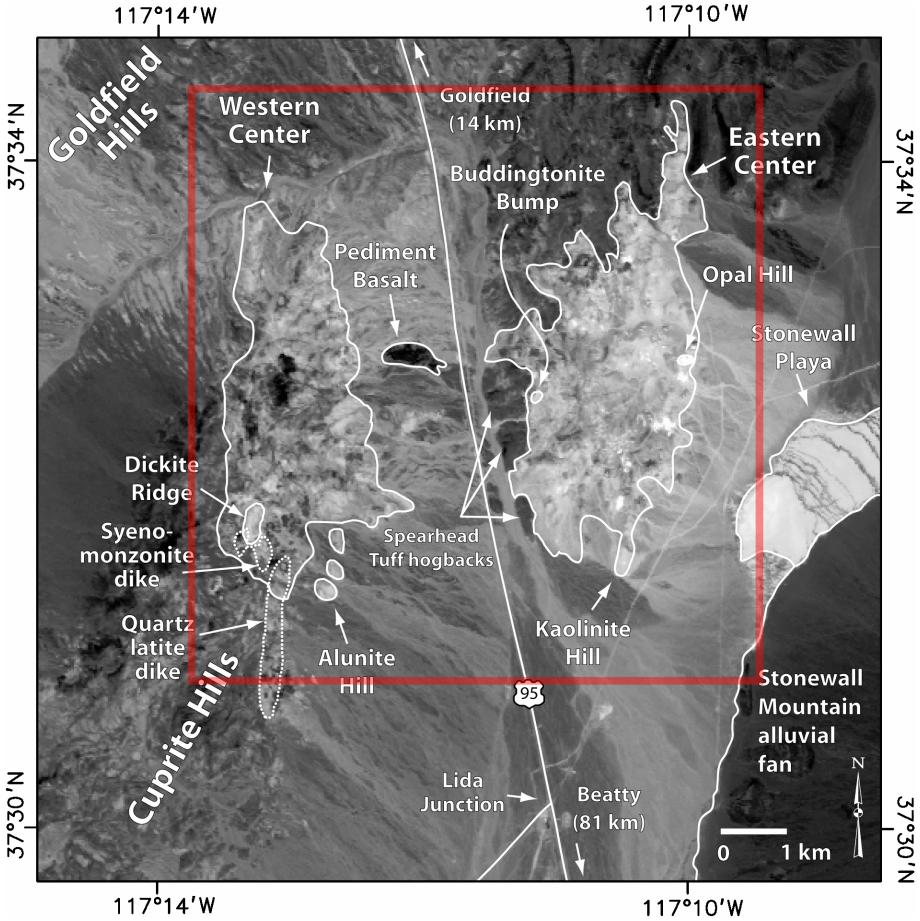

(b)

Figure 6.20: (a) AVIRIS image of the selected region. Composition of bands 96, 36, 16. (b) AVIRIS image with points of interests modified from Swayze et al. (2014). The area of the selected region is marked with the red rectangle.

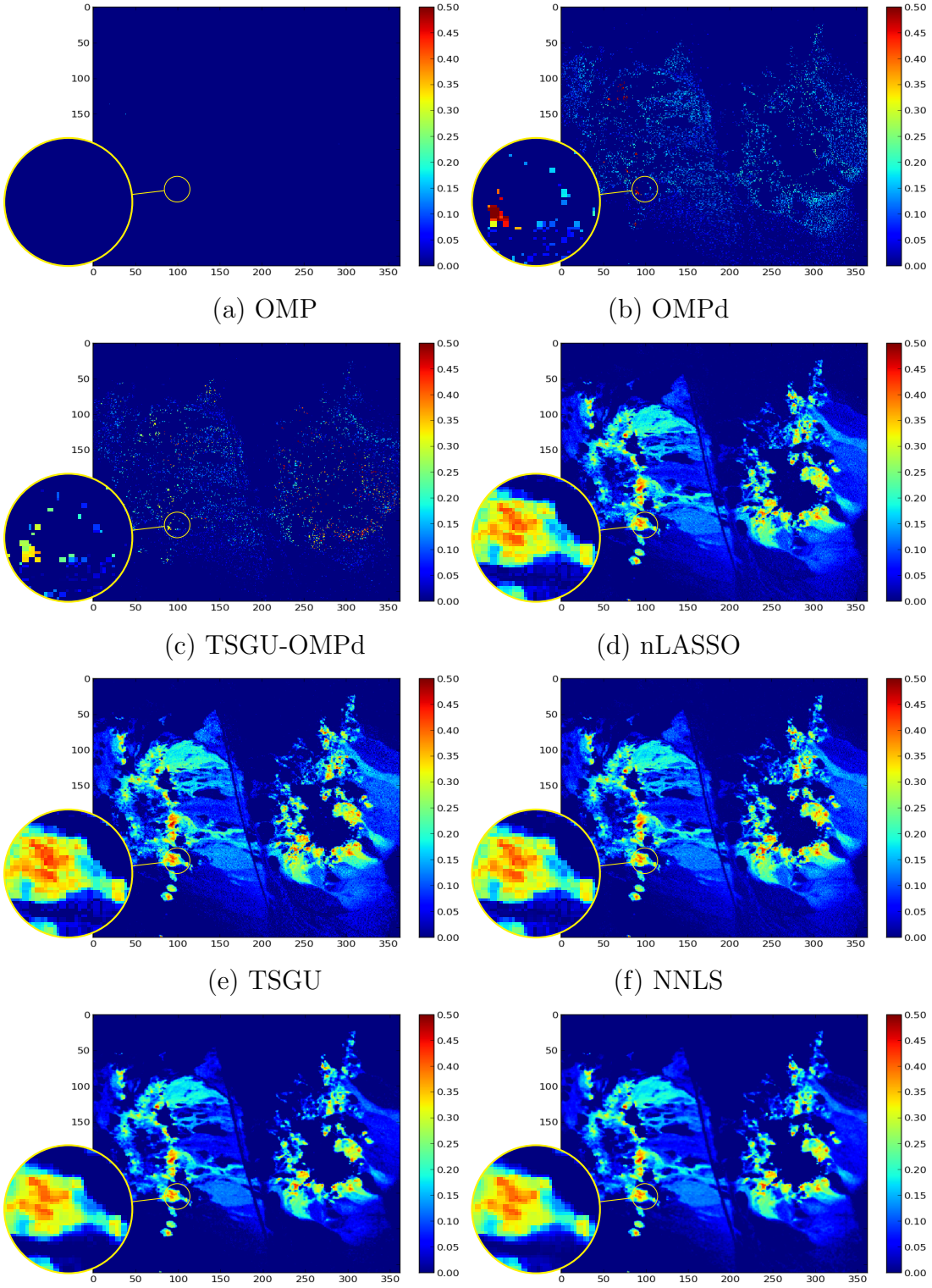

(a) OMP (b) OMPd

(c) TSGU-OMPd (d) nLASSO

(e) TSGU (f) NNLS

(g) MLJSM $J = 5$ (f)MLJSM $J = 9$

Figure 6.21: Unmixing results using tested algorithms for the alunite spectrum.

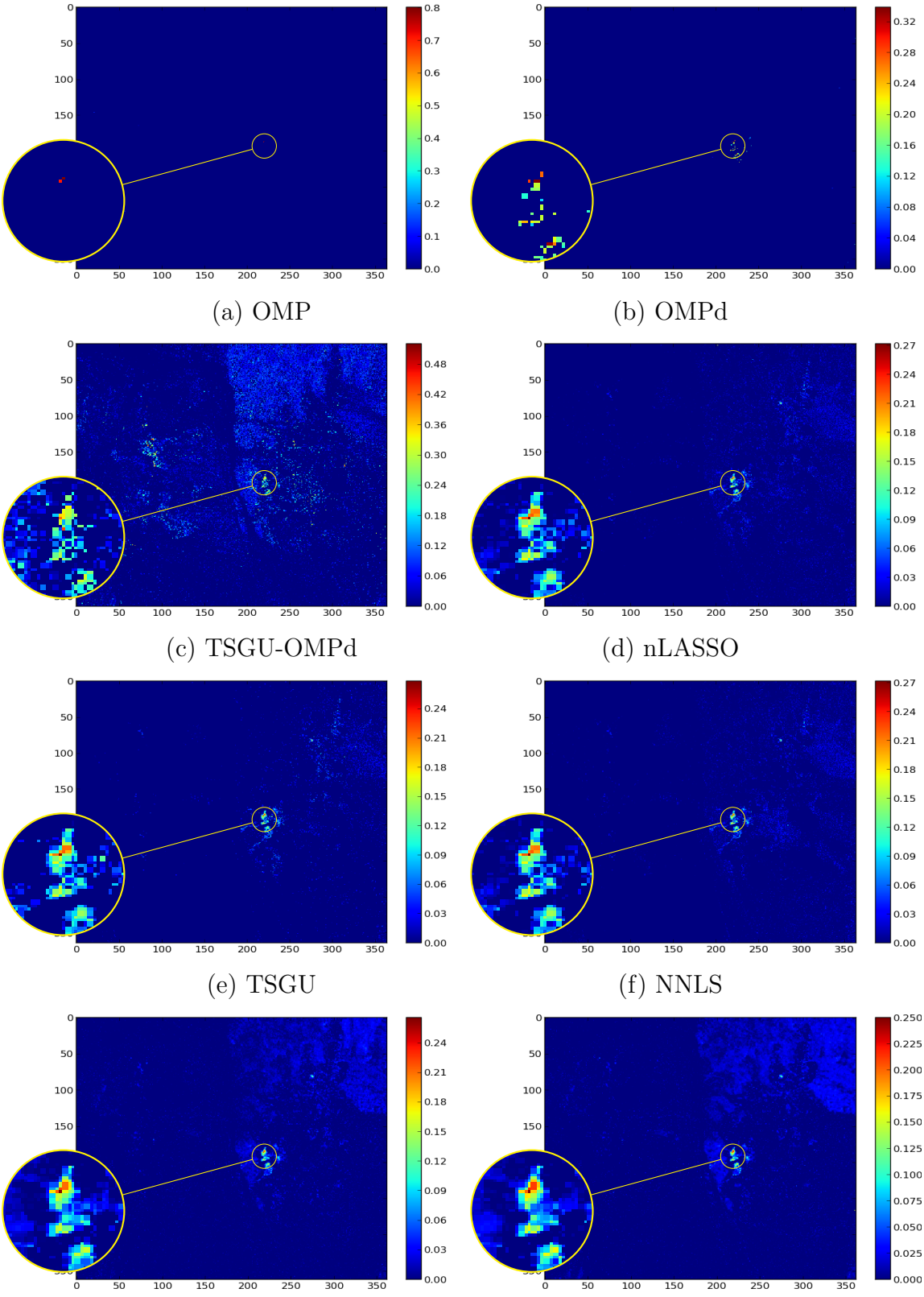

(a) OMP (b) OMPd

(c) TSGU-OMPd (d) nLASSO

(e) TSGU (f) NNLS

(g) MLJSM $J = 5$ (h) MLJSM $J = 9$

Figure 6.22: Unmixing results using tested algorithms for the buddingstone spectrum.

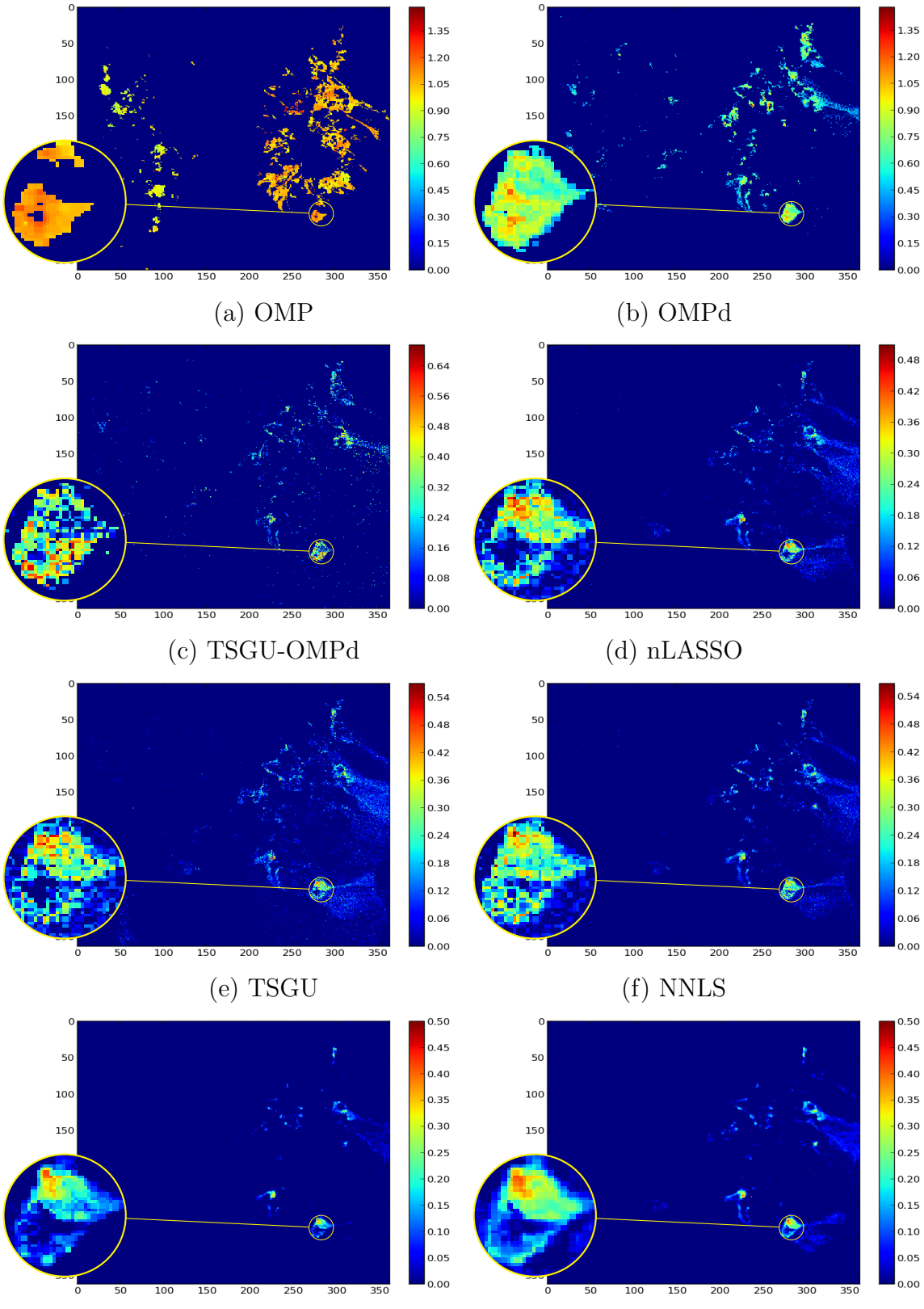

(a) OMP (b) OMPd

(c) TSGU-OMPd (d) nLASSO

(e) TSGU (f) NNLS

(g) MLJSM $J = 5$ (h) MLJSM $J = 9$

Figure 6.23: Unmixing results using tested algorithms for the kaolinite spectrum.

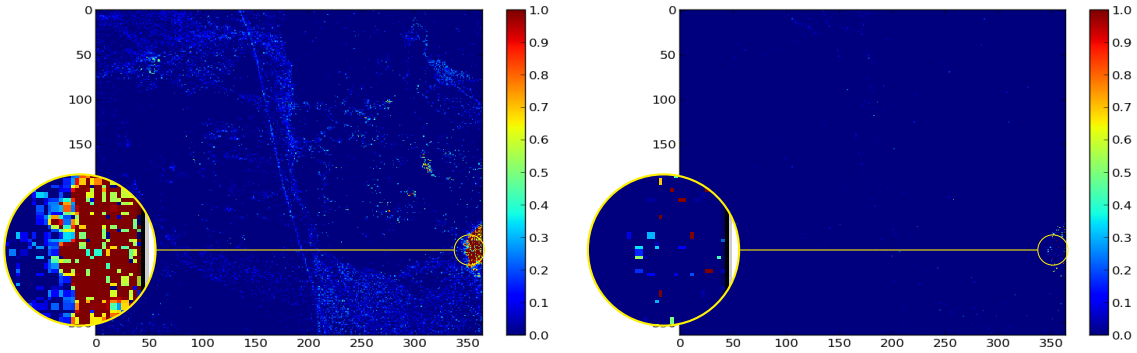

(a)TSGU-OMPd (b)TSGU

Figure 6.24: Unmixing results using TSGU-OMPd and TSGU algorithms for the playa spectrum. Other tested algorithms did not detect any abundance of this mineral.

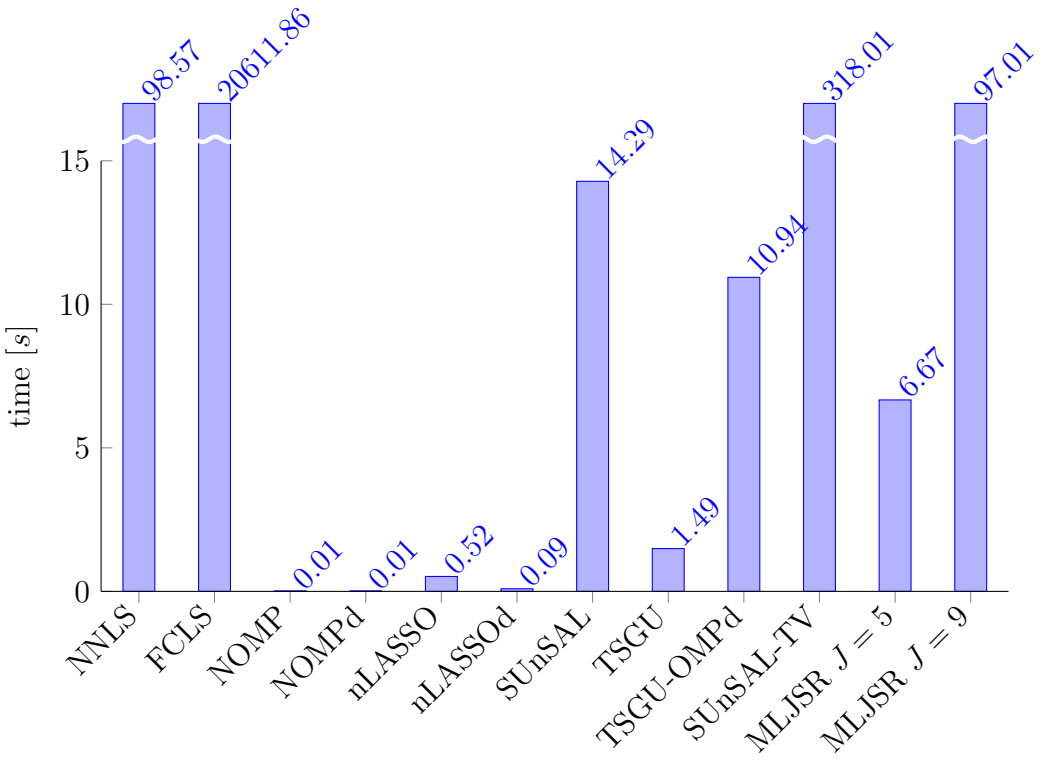

Figure 6.25: Execution time of tested algorithms for dataset with 10000 pixels, 224 channels and SNR = 30dB.

7

Multi-Look Joint Sparsity Fusion - Experiments

In this chapter the proposed resolution enhancement method will be tested and compared to the state-of-the-art methods. First, the experiment with simulated data will be performed to asses the proposed resolution enhancement algorithm . Then, the algorithms are assessed using low spatial resolution Hyperion hyperspectral image and high resolution AISA hyperspectral image. Finally the proposed algorithms are tested using data from sensors of the Mars Reconnaissance Orbiter (MRO), HiRISE and CRISM.

7.1 Evaluation Criterion

The goal of the resolution enhancement is to increase the amount of spatial information of the hyperspectral image preserving the spectral information. Therefore, in order to evaluate the results, both the spectral and spatial domain have to be investigated. If the ground truth image, i.e., high spatial resolution hyperspectral image, is available the resulting enhanced hyperspectral image is compared to that image. Otherwise, the improvement of the quality or preservation of information of the image after applying resolution enhancement methods is examined.

7.1.1 Spectral Information Evaluation - Spectral Angle Distance

The SAD is one of the most commonly used similarity measure in hyperspectral applications. It has been introduced in Kruse et al. (1993). SAD measures the angle between two spectra

$$\text{SAD} = cos^{-1} \frac{\sum_{i=1}^{m} y_{oi} y_{ri}}{\sqrt{\sum_{i=1}^{m} {y_{oi}}^2} \sqrt{\sum_{i=1}^{m} {y_{ri}}^2}} \tag{7.1}$$

where, m denotes the number of spectral bands, y_o is the original high resolution hyperspectral spectrum and y_r is the spectrum of the corresponding reconstructed high resolution hyperspectral pixel. The smaller the SAD is the more similar the spectra are.

7.1.2 Spatial Information Evaluation

To evaluate the spatial information three measures are applied. First, the SSIM is defined as

$$\mathrm{SSIM}(a,b) = \frac{(2\mu_a\mu_b + C_1)(2\sigma_{ab} + C_2)}{(\mu_a^2 + \mu_b^2 + C_1)(\sigma_a^2 + \sigma_b^2 + C_2)} \tag{7.2}$$

is used, where a denotes a window in a band of the reference image, b is a corresponding window in a corresponding band of the reconstructed image, σ_a^2, σ_b^2 and σ_{ab}, μ_a, μ_b denote respectively the variance of a, variance of b, the covariance between a and b, mean value of a and mean value of b, C_1 and C_2 denote the variables stabilising the division. The SSIM has been proposed in Wang et al. (2004) as a method more consistent with the human eye as the standard methods for the image similarity measure e.g. peak signal-to-noise ratio or MSE. The SSIM assesses the quality of the image by the degradation of structural information. This is done by comparing the luminescence and structure at the same time; for more details refer to Wang et al. (2004).

Second, the normalised cross correlation (NCC) measure is used and defined as

$$\mathrm{NCC}(i) = \frac{1}{p}\sum_{i=1}^{p} \frac{(y_{oj} - \overline{y_o})(y_{rj} - \overline{y_r})}{\sigma_{y_o}\sigma_{y_r}} \tag{7.3}$$

where σ is the standard deviation and p is the number of pixels. The NCC gives the values in the interval [0, 1] where 0 means no correlation and 1 the perfect match between images. The normalisation makes the NCC invariant to the constant change in brightness in the whole spectral band. This measure is pixel based and it is calculated at each spectral band i separately. Thus the mean NCC provides a good feeling how well the complete reconstructed hyperspectral image matches the reference image.

As a third measure the Normalised Root Mean Squared Error (NRMSE)

is used,

$$\text{NRMSE} = \frac{1}{m}\sum_{i=1}^{m}\sqrt{\frac{1}{p}\frac{\sum_{j=1}^{p}(y_{i,j}^{o} - y_{i,j}^{r})^2}{\sum_{j=1}^{p} {y_{i,j}^{o}}^2}} \tag{7.4}$$

It is calculated over the complete image and can have values ranging form 0 to infinity where 0 means no error. However, NRMSE with values larger than one mean that the difference between reconstructed and original image of band i is larger the the original image from the same band.

7.2 Simulated Image Pair

7.2.1 Experiment Settings

In this experiments the AVIRIS hyperspectral image taken over Cuprite, Nevada, USA (JPL, 1997), with originally 224 spectral channels in the range of 0.4 to 2.4 μm was used. From this scene a region of size 198×300 pixels [Figure 7.1(b)] have been selected and the noisy and water absorption bands have been discarded, so as the final test scene had 184 spectral channels. To produce a spectral dictionary, 240 spectra were selected from the USGS Digital Spectral Library (Clark et al., 2007). The low resolution hyperspectral image was simulated by down-sampling the spatial resolution of the original image from 5 m (Figure 7.1(b)) to 30 m (Fig. 7.1(a)) using a Gaussian filter as PSF. Because the spatial down-sampling reduces noise in the image, the zero-mean Gaussian noise has been added to the low resolution hyperspectral image. The sigma has been chosen to

$$\sigma = \sqrt{\frac{1}{1000}\frac{1}{p \cdot m}\sum_{i=1}^{p}\sum_{j=1}^{m}(y_j^2)} \tag{7.5}$$

where y_j is jth hyperspectral pixel, p is the number of pixels in the image and m is the number of spectral channels. This resulted in the decrease of SNR

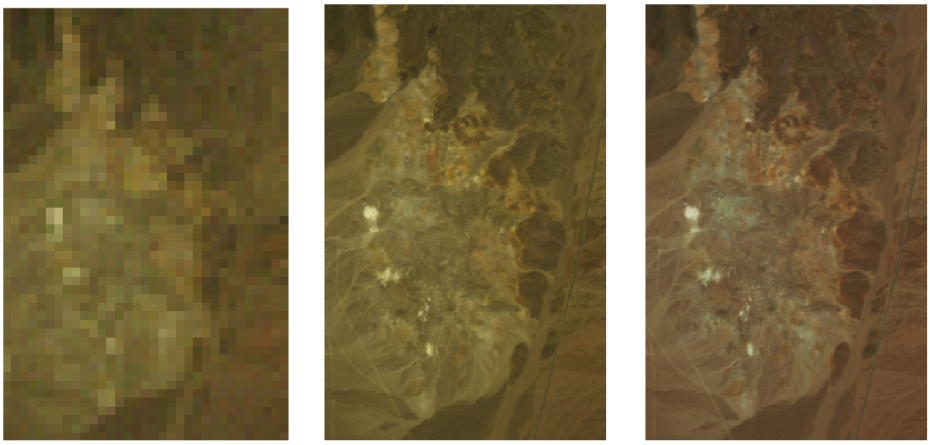

(a) Low resolution AVIRIS image (b) original high resolution AVIRIS image (c) high resolution LANDSAT image

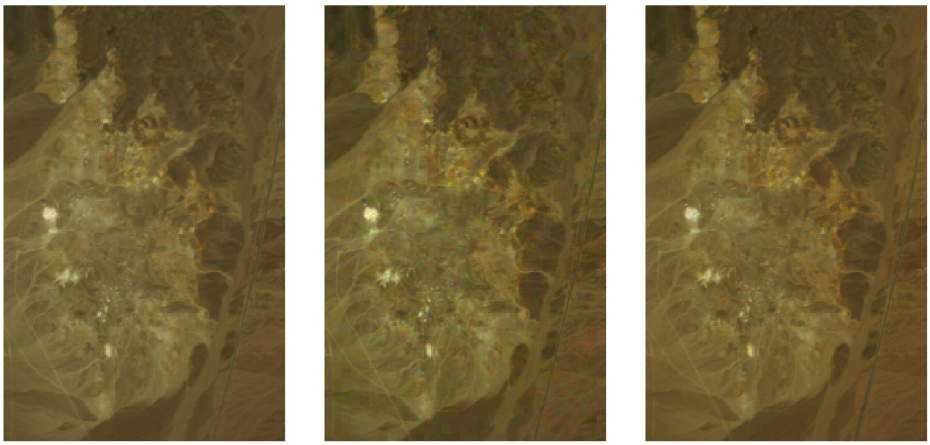

(d) CNMF result (e) MAP/SMM result (f) MLJSF result

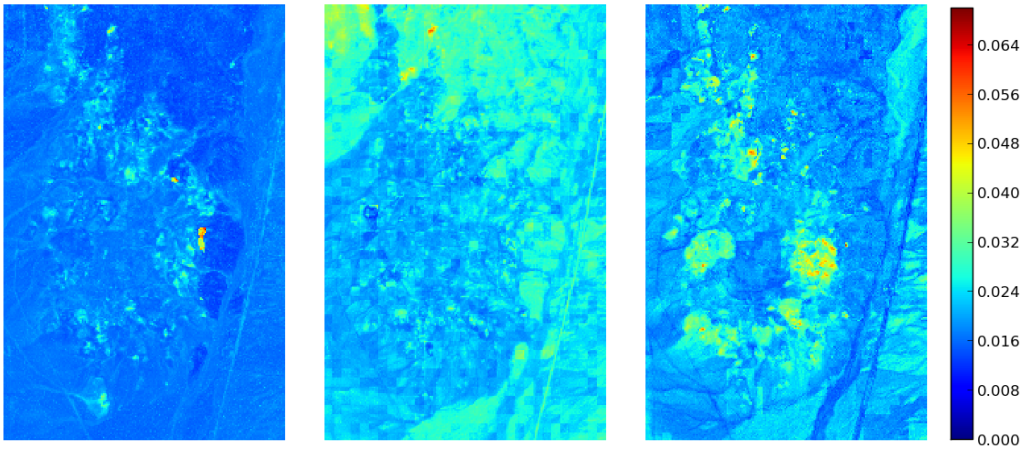

(g) SA for CNMF (h) SA for MAP/SMM (i) SA for MLJSF

Figure 7.1: Comparison of original [(a)-(c)] and reconstructed images [(d)-(f) (RGB from channels 96, 36 and 16 respectively). (g)-(i) presents SA between original and reconstructed images scaled from 0 to the maximum value from the three results.

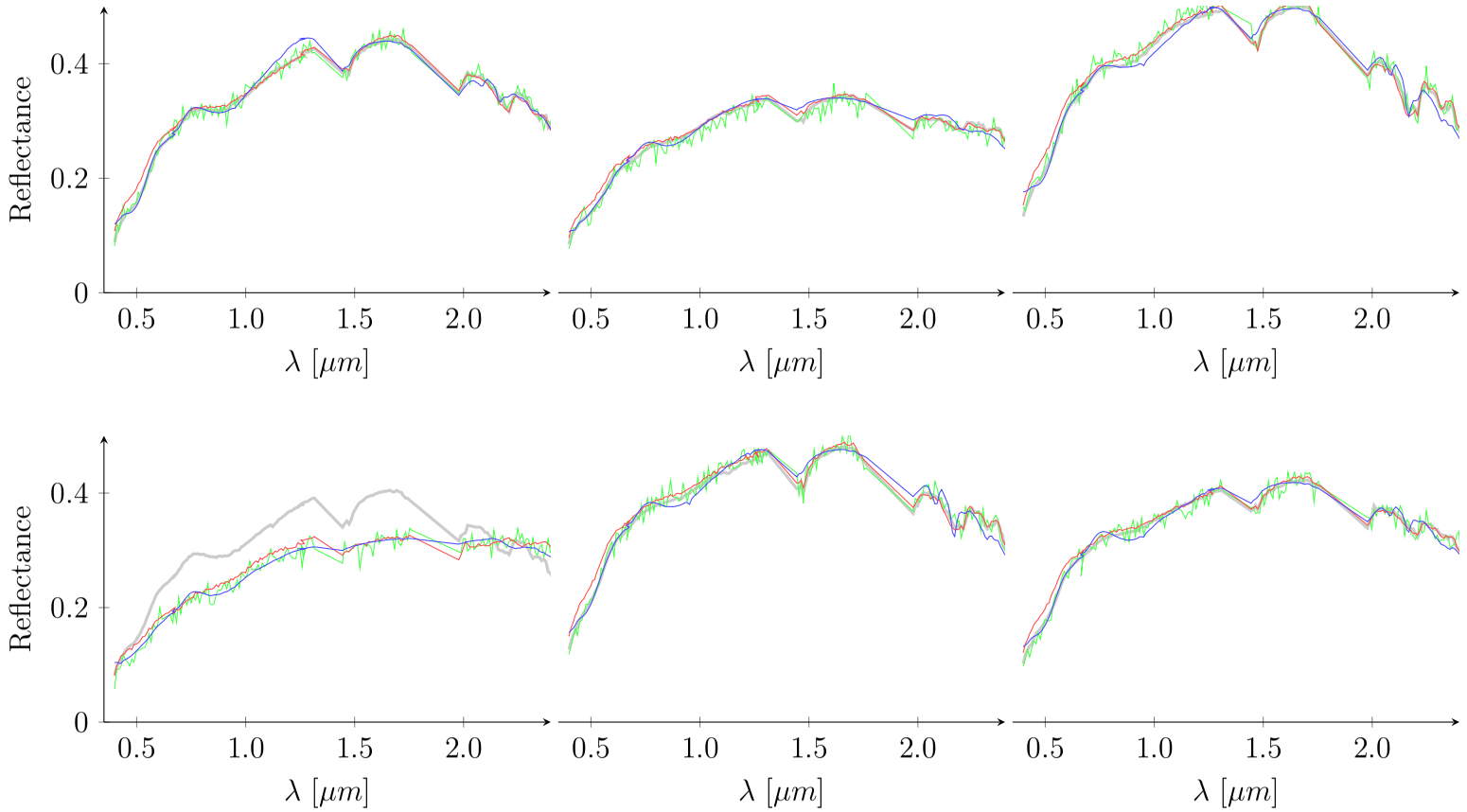

Figure 7.2: Spectra selected from random positions of the original high resolution HSI (——) and results of the resolution enhancement algorithms MLJSF (——), CNMF (——) and MAP/SMM (——).

by 30 dB. A multispectral image of 5 m spatial resolution and 6 bands with signal response function of LANDSAT (Figure 7.1(f)) has been simulated as described in section 2.2.5.

7.2.2 Results and Discussion

The MLJSF algorithm was compared with the state of the art maximum a posteriori stochastic mixing model (MAP/SMM) and the CNMF methods. The parameters for all algorithms were set so to result in the best performance. For more details please refer to Yokoya et al. (2011) and Eismann and Hardie (2005b).

Table 7.1: Comparison of the resolution enhancement algorithms.

	NRMSE [%]	NCC	SSIM	SAD [rad]	Time [s]
CNMF	3.3%	0.99	0.98	0.024	277.25
MAP/SMM	4.1%	0.97	0.91	0.034	56.43
MLJSF	3.2%	0.98	0.98	0.030	17.16

Table 7.2: Comparison of the resolution enhancement algorithms with coregistration error of one pixel.

	nRMSE [%]	NCC	SSIM	SADrad
CNMF	3.6%	0.98	0.984	0.030
MAP/SMM	15.1%	0.61	0.510	0.059
MLJSF	3.3%	0.98	0.987	0.030

The results of NRMSE, NCC, SSIM and SAD analysis are shown in Table 7.3. The MLJSF method outperforms CNMF and MAP/SMM in the sense of

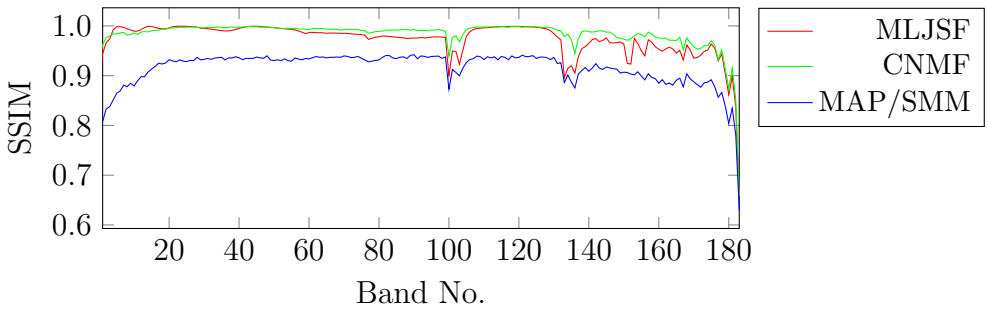

Figure 7.3: Comparison of the SSIM values across the spectral bands of tested algorithms.

R-MSE with 3.2%. When comparing NCC all methods performed similarly with the best result of 0.99 for CNMF. All methods have very high SSIM indices which indicates very good reconstruction of the spatial domain. A detailed plot of the SSIM across all bands is shown in Figure 7.3. Figure 7.1 shows the results of each method (c)-(e) compared to the original high resolution AVIRIS image (b). All algorithms were able to fairly recover spatial details with very little change in the intensity values. Square artefacts visible in the bottom of the MAP/SMM reconstructed image [Figure 7.1(d)] indicate the transmission of noise from the low resolution hyperspectral image. Figure 7.1(g)-(i) show the SAD evaluation. Examples of reconstructed spectra compared to the original ones are shown in Figure 7.7. The use of external noise free spectra from the dictionary the MLJSF method results in smoother spectra when compared to other methods. This also confirms the denoising property of the MLJSF (Cerra et al., 2014). Again, MAP/SMM transmitted most of the noise from the low resolution image. Additionally, the algorithms were tested for their performance when the coregistration error is present. All algorithms were run on the same dataset with a vertical shift of one hyperspectral pixel. The comparison results are reported in Table 7.2. Both algorithms MLJSF and CNMF are relatively robust to small coregistation errors when compared to MAP/SMM. The quality of reconstruction for the MLJSF algorithm did not change when considering NCC, SSIM and SAD. The quality of the CNMF reconstruction decreased considering all measures. The MAP/SMM method performed the worst and the

quality decreased drastically.

7.3 Real Image Pair - Germany

7.3.1 Experiment Settings

To test the MLJSF algorithm with real data a pair of coregistered images was used. A space borne Hyperion hyperspectral image (Ungar et al., 2003) [Figure 7.5 b)] and an airborne AISA hyperspectral image [Figure 7.5 a)]. After band selection the Hyperion image was of a size 80× 70 pixels and 152 spectral channels. The AISA image had 774×684 pixels and 100 spectral bands. Both datasets were geometrically as well as atmospherically corrected. Both datasets were acquired the same day 10 km north west from Köthen in Sachen-Anhalt, Germany. The high resolution multispectral image has been simulated from the AISA image using the signal response function of the LANDSAT 7 sensor. The resulting image had a 3m GSD and 6 spectral channels. The GSD of the Hyperion image is of 30m. Additionally, for the MLJSF algorithm a spectral dictionary containing 177 spectra was provided. The dictionary was combined from 110 materials from the USGS spectral library and 67 measurements of the wheat fields. The MLJSF algorithm was run with $\lambda_1 = 2.24 \times 10^{-4}$ and $\lambda_2 = 1.6710^{-5}$. The CNMF algorithm has been run with 40 endmembers and parameter settings yielding the best possible results (Yokoya et al., 2011).

7.3.2 Results and Discussion

Unlike in data simulated from one hyperspectral image like in the previous section or in Bieniarz et al. (2011, 2014); Eismann and Hardie (2005b); Grohnfeldt et al. (2014); Robinson et al. (2000); Yokoya et al. (2012), an *ideal-case* reference image is not available. Therefore, a direct comparison

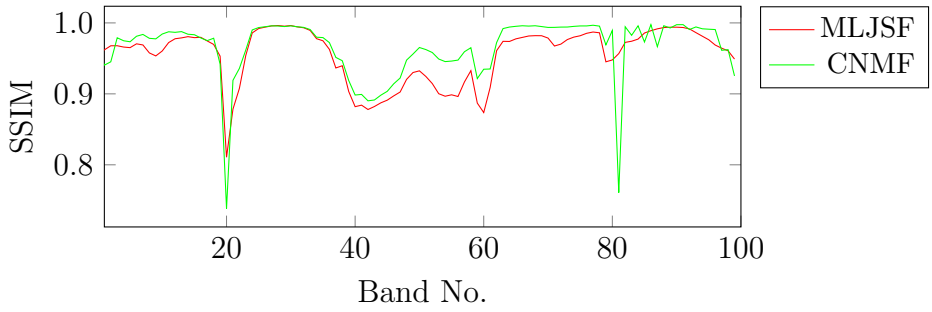

Figure 7.4: Comparison of the SSIM values across the spectral bands of tested algorithms.

with a reference image is not possible. To assess the results of the resolution enhancement we performed a classification of all datasets and compared the results with the classification of the high resolution original AISA image. The evaluation set-up has been designed as follows: at first, the location of 12 classes was defined with one training sample for each class. Next, the training samples were collected for all datasets i.e. AISA, Hyperion, MLJSF result and CNMF result. Finally, a Spectral Angle Mapper (SAM) classification (Kruse et al., 1993) was run for all datasets using these training samples. The resulting classification was compared to the classification of the AISA image. The classification results are shown in Fig. 7.6. Both methods CNMF [Fig. 7.6 d)] as well as MLJSF [Fig. 7.6 c)] significantly improved the classification performance when compared to the classification performed on the original Hyperion image [7.6 b)]. The CNMF was able to improve the classification overall accuracy (OA) by 22.16% and MLJSF by 36.87% when compared to the Hyperion classification results. Also, the Cohen's Kappa (κ) has been improved from 0.36 for Hyperion to 0.59 for CNMF and to 0.76 for MLJSF (for more details see Table 7.3). Fig. 7.7 shows the selected spectra from the original AISA image, the Hyperion image and the reconstructed spectra from the same locations. The identification of different materials is easier in AISA as well as in images produced by MLJSF or CNMF. The MLJSF results in smoother spectra when compared to CNMF results or to the original Hyperion image, which is reasonable considering the use of the a priori given

spectral dictionary.

To measure the quality of reconstruction relative to the AISA image, we resample the resulting images from CNMF and MLJSF to match the spectral channels of the AISA sensor. For comparison we use the SSIM, SAD, NCC and NRMSE measures. The results are presented as the average values for the whole image and are shown in the Table 7.3. The plot showing the SSIM of every band image is shown in Figure 7.4. Both methods exhibit very high SSIM with a slight drop of value for band no. 20. Both algorithms significantly improved the quality in both spatial as well as in spectral domain when compared with the AISA reference image. Considering the execution time the MLJSF algorithm was also much faster (46.87 s) when compared to CNMF (388.62 s).

Table 7.3: Results of the comparison. As reference the measures for low resolution Hyperion image are provided. The Hyperion image has been resampled to AISA spectral and spatial resolution.

	OA [%]	κ	SSIM	SADrad	NCC	NRMSE [%]	Time [s]
Hyperion	42.08	0.36	0.16	0.121	0.82	91.6	-
CNMF	64.27	0.59	0.95	0.061	0.98	6.8	388.62
MLJSF	78.95	0.76	0.96	0.067	0.97	7.8	46.87

7.4 Real Image Pair - Mawrth Vallis, Mars

7.4.1 Experiment Settings

In this experiment the data from the Mars Reconnaissance Orbiter sensors, namely HiRISE and CRISM are used. The HiRISE sensor is capable of

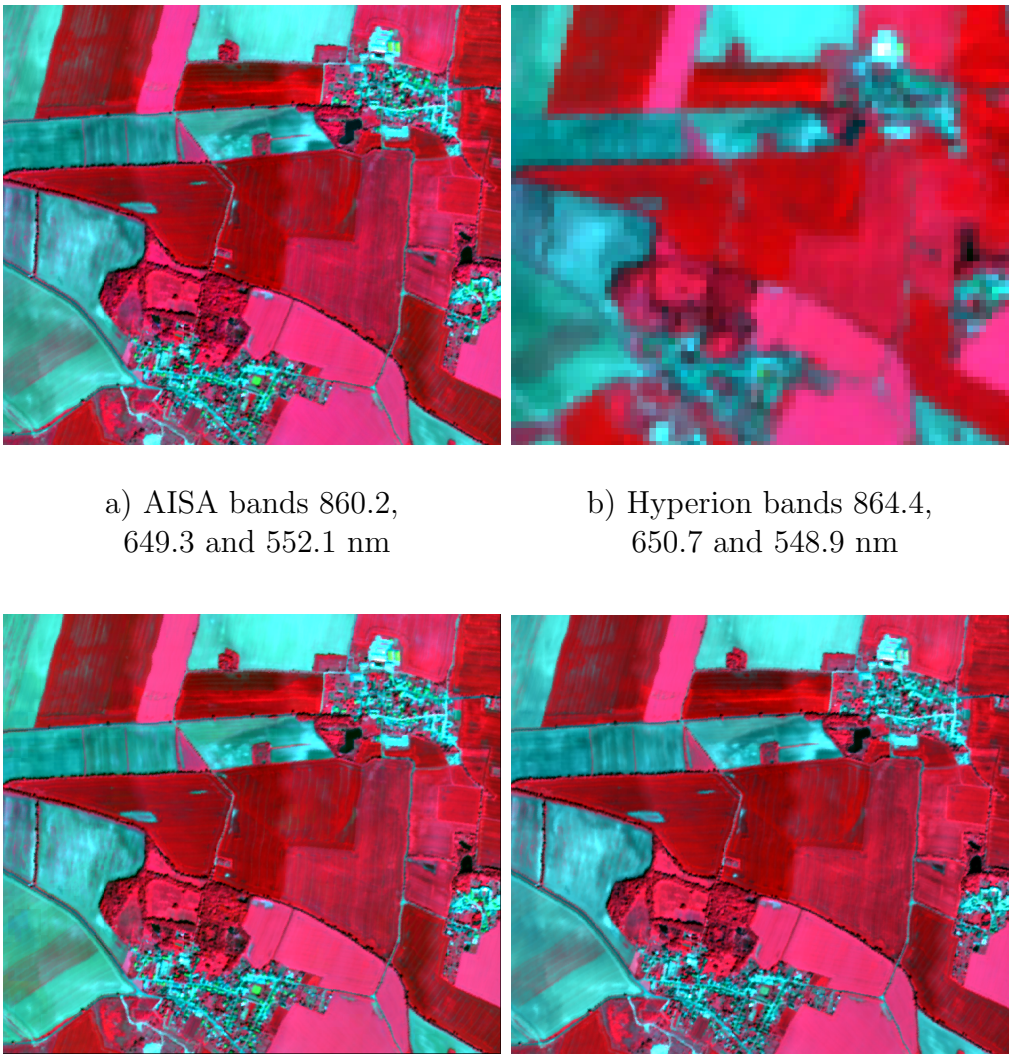

a) AISA bands 860.2, 649.3 and 552.1 nm

b) Hyperion bands 864.4, 650.7 and 548.9 nm

c) MLJSMF bands 864.4, 650.7 and 548.9 nm

d) CNMF bands 864.4 nm, 650.7 nm and 548.9 nm

Figure 7.5: False RGB composition of input Hyperion and AISA images and resulting high spectral and spatial resolution images.

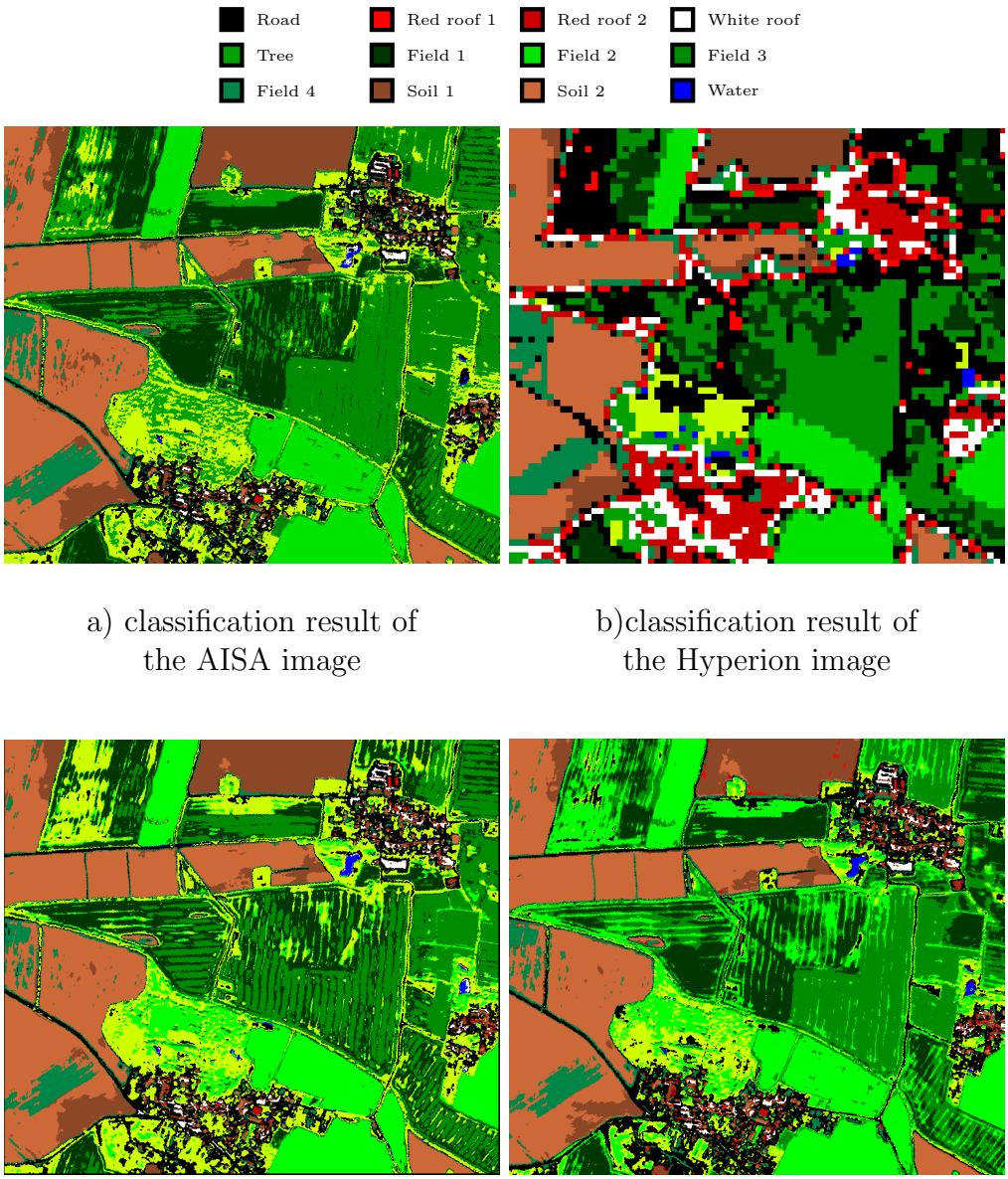

a) classification result of the AISA image

b)classification result of the Hyperion image

c) classification result of the MLJSMF image

d) classification result of the CNMF image

Figure 7.6: Result of the SAM classification using original AISA, Hyperion and fusion results of MLJSF and CNMF.

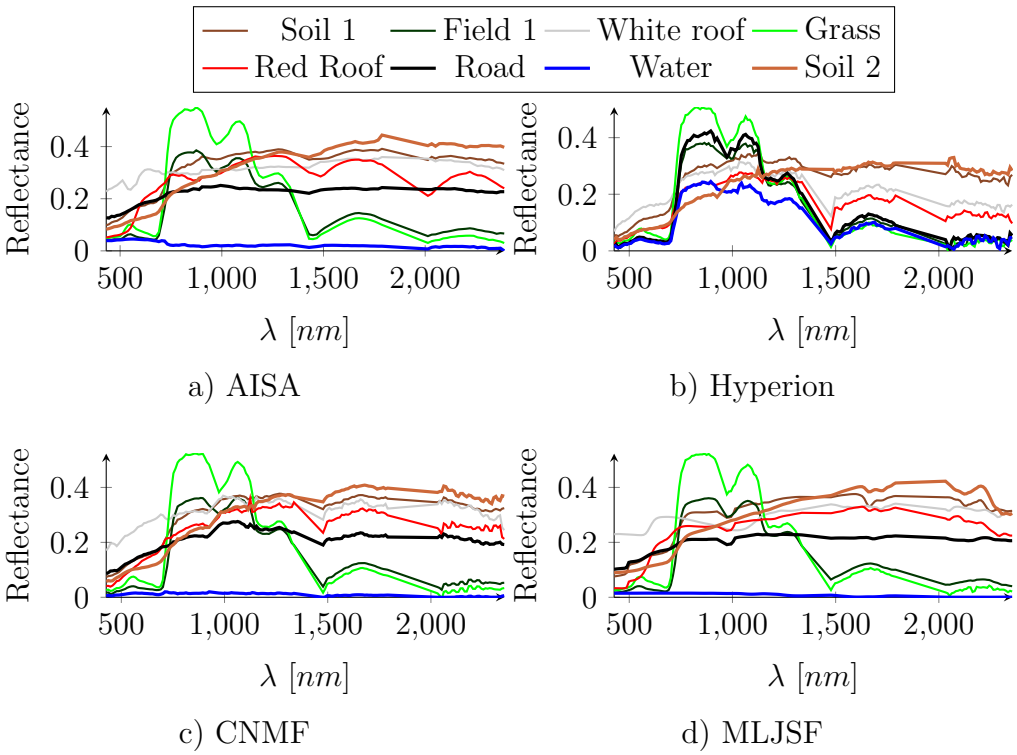

Figure 7.7: Comparison of selected spectra from the AISA image, Hyperion image and results of the resolution enhancement algorithms CNMF and MLJSF.

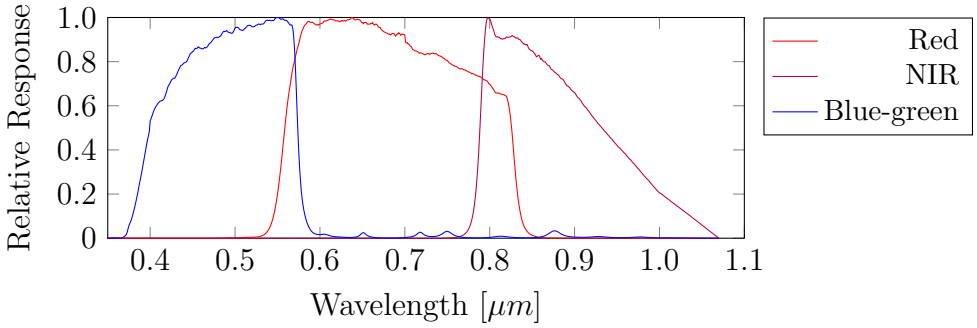

Figure 7.8: Measured SRF of each HiRISE spectral band.

imaging with spatial resolution of 0.3 m at an altitude of 300 km. It has three spectral bands available, at blue-green (400 - 600 nm), red (550 - 850 nm) and near-infrared (NIR) (800 - 1000 nm) (McEwen et al., 2007). The SRF of these bands are shown in Figure 7.8. The hyperspectral sensor CRISM has 544 spectral bands ranging from 370 to 3920 nm and spatial resolution of 18.4 m at 300 km in targeted mode (Murchie et al., 2007).

The region of Mawrth Vallis on Mars has been selected as the test area. The Mawrth Vallis was selected as one of the possible landing sides of the Mars Science Laboratory (MSL) (Michalski et al., 2010). A pair of images has been selected from, the HiRISE image (ESP_012873_2045), and the CRISM image (FRT000094F6). The images were co-registered using the XDibias software (Müller et al., 1993) by manually selecting 9 ground control points. The selected region and correspondences between the images are shown in Figure 7.9 In order to reduce the resolution ratio between the images the HiRISE has been down-sampled by the factor of 10 to a spatial resolution of 3 m using the method described in section 2.2.5 using a Gaussian filter as the PSF of the lower resolution image.

Here, unlike in previous experiments, the two images are not georeferenced. Therefore, in order to avoid interpolation of the images in the co-registration process, the fusion is done on the original images using the affine transfor-

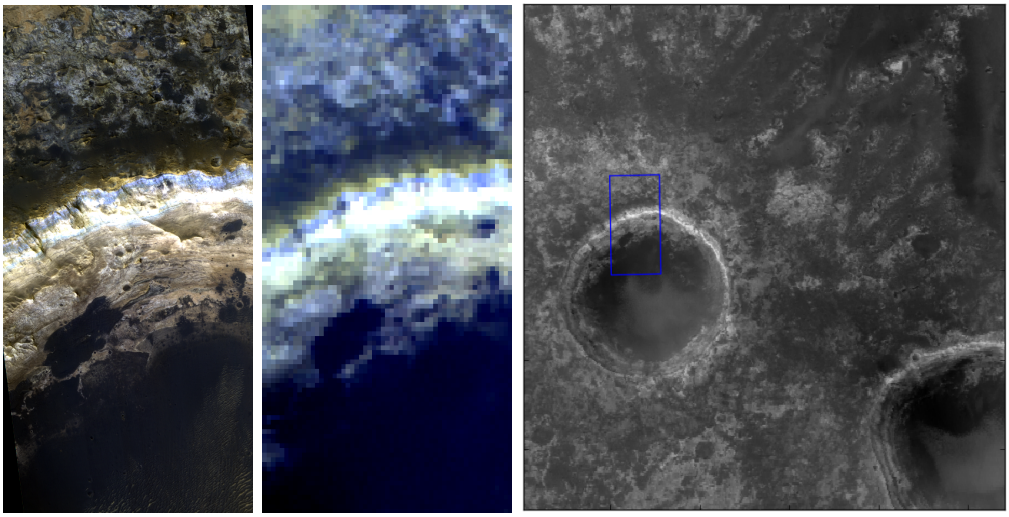

a) HiRISE b) CRISM c) CRISM selected region

Figure 7.9: Images used in the resolution enhancement experiment. Subfigures show the HiRISE ESP_012873_2045 image in a), the coregistered part of the CRISM FRT000094F6 image in b) and the complete CRISM scene with the coregistered region marked by a blue rectangle.

mation matrix computed in the co-registration process.

7.4.2 Results and Discussion

A dictionary with 9 endmembers extracted from the hyperspectral scene was used. For the endmembers estimation the N-FINDR algorithm (Winter, 1999) was applied. The MLJSF algorithm has been applied to the HiRISE and CRISM image pair with following settings $\lambda_1 = 4.53 \cdot 10^{-}5$ and $\lambda_2 = 9.11 \cdot 10^{-}4$. Selected bands and band compositions of the resulting image is shown in Figure 7.10. Comparing the CIR HiRISE image and CIR composition of the MLJSF image the spatial structures are well preserved including the color composition. However it should be noted that the width of the bands are much different, very broad for HiRISE and narrow for CRISM, therefore color comparison should be performed with caution. The zoomed area has been described in Saper and Bishop (2011) as the region containing significant

minerals as nontronite, altered volcanic glass and ferrous materials. The geometrical resolution of this region is significantly improved. Figure 7.10 (c-e) shows the comparison of MLJSF result with the CRISM image. Note that the bands at 1.43 μm and 1.91 μm are far beyond the HiRISE spectral range and since the MLJSF algorithm was able to provide reasonable results when compared to CRISM or spatial features in HiRISE image. Figure 7.11 shows comparison of the spectra of the MLJSF result with spectra from the corresponding pixel in CRISM image. The upper three spectra were picked from the regions indicated in Saper and Bishop (2011) while lower three spectra were selected from regions where the SAD between CRISM and HiRISE was relatively high.

To quantitatively analyse the preservation of the spatial features of the MLJSF method the NCC has been calculated between the HiRISE image and MLJSF image re-sampled to match the HiRISE SRF. Likewise, the NCC was computed for the original CRISM image which was up-sampled using nearest-neighbours interpolation and re-sampled to match the HiRISE SRF. The NCC has been significantly improved using the MLJSM method from 0.04 for CRISM to 0.98 for HiRISE.

Similarly, the spectral preservation has been checked comparing the SAD between the spatially up-sampled version of the CRISM image and the result of the SSIM method. The low SAD value of 0.0576 indicates that the the spectral information has been preserved in the reconstructed MLJSF image. This value however, should be interpreted with caution because of the large resolution difference and can be interpreted only as proof of the spectral similarity between the MLJSF product to the original image.

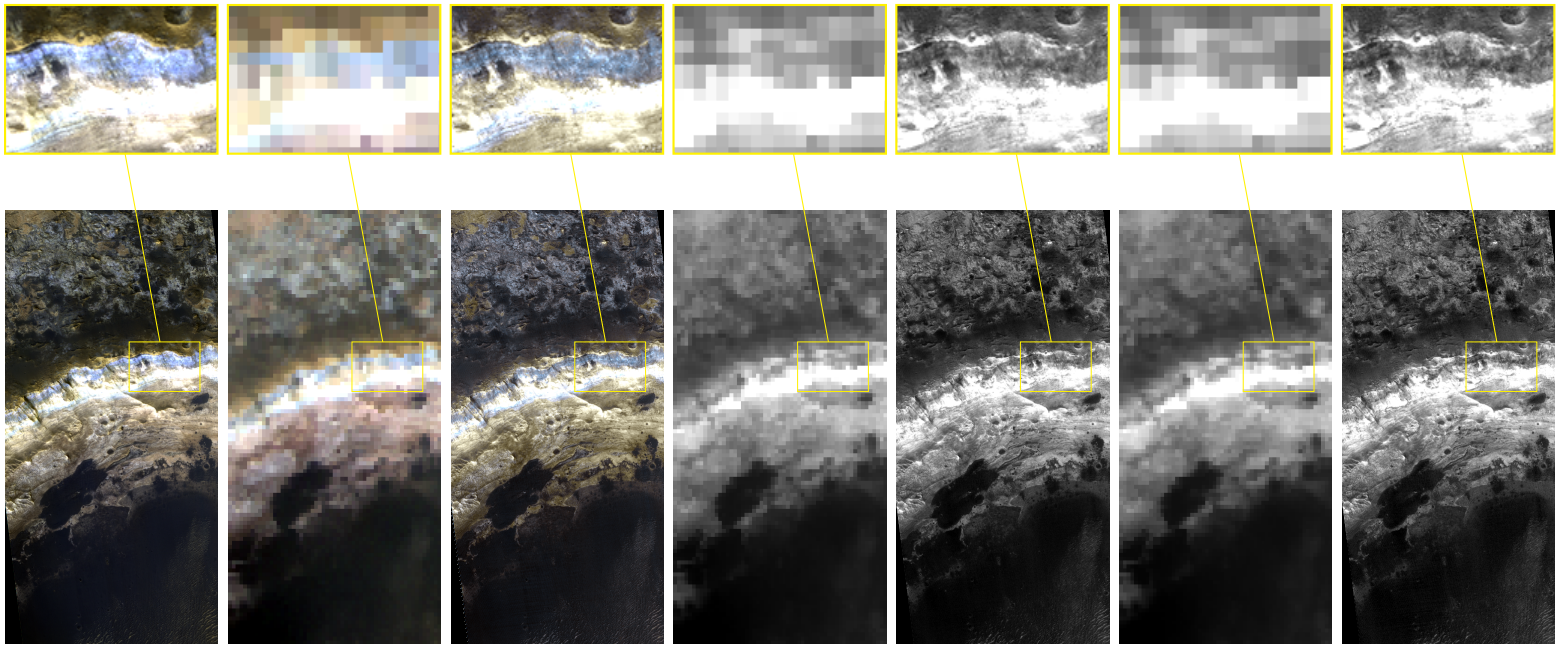

a) HiRISE CIR image | b) CRISM CIR image | c) MLJSF image bands at 0.86, 0.65, 0.55 μm | c) CRISM band 1.43 μm | d) MLJSF band 1.43 μm | e) CRISM band 1.91 μm | e) MLJSF band 1.91 μm

Figure 7.10: Images used in the resolution enhancement experiment. Sub-figures show the HiRISE ESP_012873_2045 image in a), the coregistered part of the CRISM FRT000094F6 image in b) and the complete CRISM scene with the co-registered region marked by a yellow rectangle.

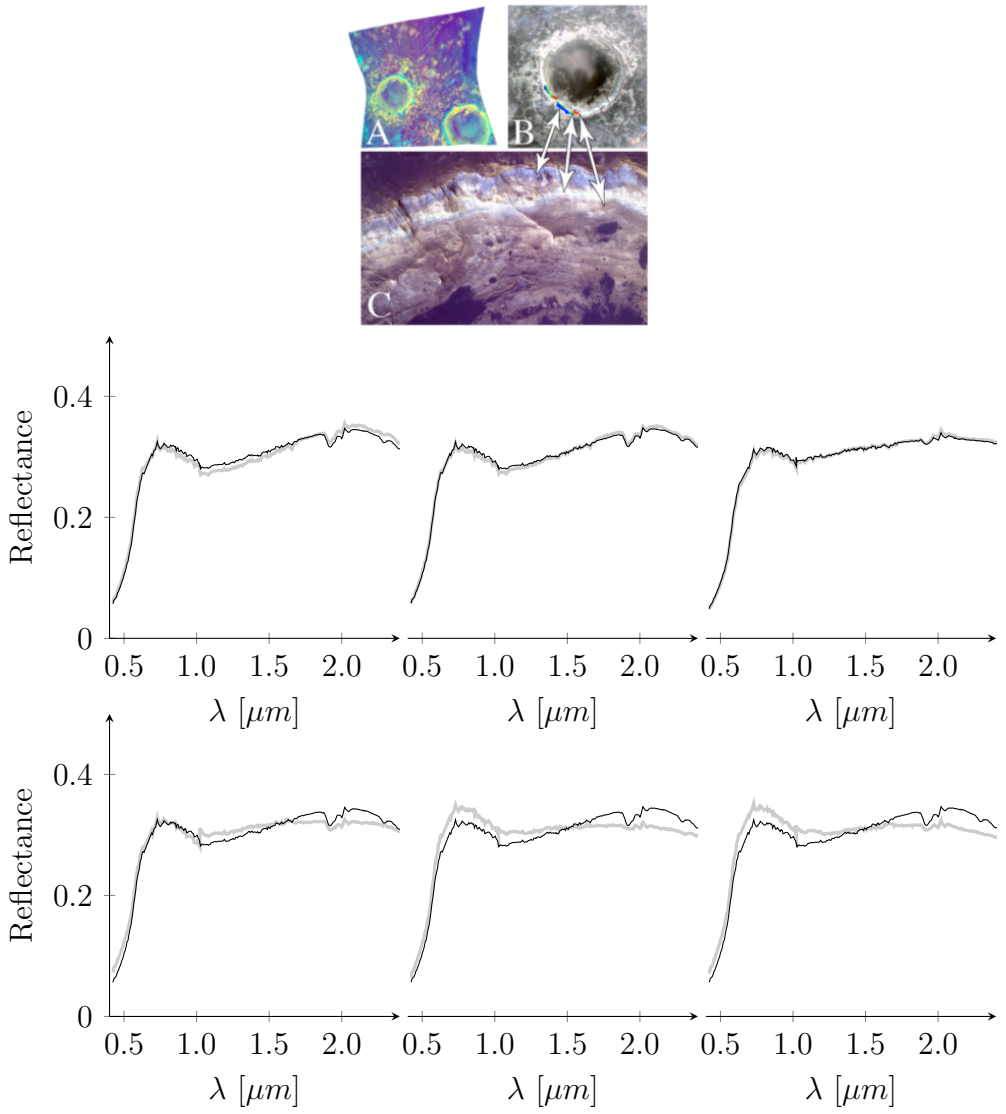

Figure 7.11: Upper three spectra from the top were selected from positions indicated in the figure above (the figure is from Saper and Bishop (2011)). Lower three spectra were selected from regions where the SAD was higher. The gray line (——) indicates the spectrum from the corresponding region in CRISM. The black spectra (——) are from the fusion resulting image.

7.5 Summary

In this chapter the new method MLJSF for hyperspectral image resolution enhancement utilising sparse unmixing models has been presented. The method was critically analysed and compared to the state of the art methods using datasets from various sensors. The summary of the results presented in this chapter is stated as follows:

- Using simulated data sets the performance of the MLJSF method has been tested. The proposed algorithm performed similarly to the state of the art methods exhibiting better reconstruction when the SSIM or NRMSE methods are considered. For the tests with coregistration error MLJSF showed the lowest decrease in the quality for NRMSE and no loss in quality considering NCC, SSIM and SAD measures. Also, it is important to note that unlike the competitors methods the MLJSF used external spectral libraries resulting in an additional products, i.e., low resolution and high resolution unmixing maps of materials.

- Another evaluation has been done using a real spaceborne Hyperion image and a simulated multispectral image from the airborne hyperspectral AISA sensor. Here, the classification has been applied to the resolution enhancement products and original Hyperion image and compared to the classification of the reference image. The MLJSF outperformed the CNMF algorithm and significantly improved the classification accuracy of the Hyperion image.

- Finally, the proposed algorithm has been tested using images of the Martian surface from the 'same-platform' satellite sensors of the MRO. The MLJSF was able to increase the spatial resolution of the 544-band hyperspectral CRISM image using the 3-band multispectral HiRISE image by a factor of 6. The numerical and qualitative assessment of the results show good results and the applicability of MLJSF to this type of data.

8

Conclusions and Future Work

This thesis was motivated by the main shortcoming of hyperspectral data, namely the decreased spatial resolution resulting from the physical properties of the sensor. Lower spatial resolution often limits the applicability of these data especially in regions with smaller objects, whose spectral responses are mixed within one pixel. These limitations are tackled by resolution enhancement techniques and spectral unmixing methods. Both are developed and discussed in this thesis.

The standard approach to spectral unmixing consists of two steps. At first, the spectra of pure materials from a hyperspectral image are recovered by manual selection or using expensive geometrical or statistical approaches to estimate or extract the endmembers. Then, their fractional abundances in every pixel are computed. Recently, more robust sparse approximation methods for hyperspectral unmixing have been proposed. They allow skipping the step of recovery of pure spectra and directly computing the fractional abundances, using a large spectral dictionary containing a set of known measured spectra. However, it has been shown that these methods suffer from several shortcomings: they are sensitive to correlation in the spectral dictionary, do not provide spatially consistent results and are often relatively slow.

The first aim of this thesis was to address the above problems. The main conclusions can be stated in the following points.

- The spectral mixing problem has been targeted by proposing MLJSR a new robust method for sparse spectral unmixing incorporating spatial information and correlations from neighbouring pixels Ṫhe method uses a specially designed dictionary that incorporates the joint recovery of common endmembers but also accounts for the approximation of non-common abundances. MLJSR, unlike most other spatial-spectral unmixing methods, operates in a window what does not enforce common endmembers in the whole scene. The MLJSR algorithm has been evaluated using real and simulated data exhibiting similar performance to other spatial-spectral unmixing method with significantly shorter

execution time and much better performance when compared to pixel-based methods. The presented findings confirm that the inclusion of the neighbouring information improves results of spectral unmixing. In addition, because the spatial correlations are exploited only in the direct neighbourhood, the endmembers are not enforced in the whole image. This therefore indicates the advantage of using MLJSR in images in which the same endmember occurs in a neighbouring group of pixels. Most notably, this is the first study to our knowledge to investigate the joint sparsity of endmember abundances in a window based manner.

- In this thesis the performance of existing methods for sparse regression was evaluated on hyperspectral data. The main focus here has been to improve these algorithms by a prior transformation or preselection within the spectral dictionary. In virtually all cases, the ℓ_1 minimisation methods perform significantly better than the OMP or NNLS. However, it has been shown that the performance of OMP or FISTA algorithms can be improved by application of the derivative transform for data with high SNR. The proposed derivative transform for sparse unmixing can be used in applications requiring very fast processing times, as the OMP was the fastest of all tested algorithms.

- It has also been shown that the preselection of the dictionary and particular use of the proposed TSGU algorithm can improve the results of sparse spectral unmixing. Unlike in state-of-the-art methods, the preselection is not done for the whole image, but it is performed in a pixel wise manner using clustered dictionaries. This fact ensures that rarely appearing endmembers will not be removed from the dictionary. This is especially important with scenes containing many endmembers and when using very large spectral dictionaries.

The second subject discussed in this thesis was the spatial resolution enhancement of hyperspectral images by means of fusion with multispectral

images. Based on the findings from chapter 4 considering sparse spectral unmixing a new fusion algorithm (MLJSF) has been proposed, which operates on external spectral dictionaries. The main findings can be summarised in the following points:

- The use of external dictionaries makes the MLJSF algorithm more robust for cases in which the hyperspectral pixels are highly mixed. This can be especially useful when considering hyperspecral images of urban areas with lower resolution (e.g. Environmental Mapping and Analysis Program (EnMAP) sensor with 30 m GSD).
- It has been shown that the MLJSF method is robust to small co-registration errors. This fact makes the presented algorithm useful when the hyperspectral and multispectral image are taken from different platforms and a perfect co-registration is not possible.
- Because MLJSF algorithm has been shown to be the significantly faster than other tested algorithms, this can be used in applications dependent on the computational time e.g. crisis management.
- The spatial resolution of a hyperspectral image acquired by CRISM has been enhanced by a factor of six. Such improvement can help the mineralogical studies of the surface of Mars with better understanding of spatial structures.

The evaluation presented in this thesis provides a baseline study for the sparse unixing approaches as well as sparse unmixing based image fusion. As an outlook the following future work is proposed:

- The potential of the MLJSM should be further developed by incorporating given different window shapes, and also by introducing weights for the pixels in window according to e.g. the PSF of the hyperspectral sensor.

- The MLJSR builds ensemble vectors of pixels in the window and then each one is separately processed. This makes the algorithm easily transferable for multithreading or GPU implementation which could yet significantly improve the performance.

- On the one hand, it has been shown that the derivative transform applied to sparse spectral unmixing improves the detection of endmembers, but is highly sensitive to noise. On the other hand, the MLJSM has been proven to be very robust to noise. These two properties can be combined by incorporating the derivative in the joint model for the abundance recovery.

- The presented TSGU algorithm has been tested with OMP and LASSO algorithms. However, it can work with different approximation methods as well as different mixing models (e.g. MLJSM). Additionally, it should be tested using other dictionary clustering methods and cluster sizes.

- As the spectral dictionary and image data are usually collected under different conditions and might not contain exactly the same endmembers as those in the image (this can be caused by e.g material age), it might be of importance to perform update of the endmembers selected in the first step in the TSGU accounting for this effects and differences.

- The PSF of both multispectral and hyperspectral sensors can be easily included in the mixing models used in MLJSF. This should improve both, the spatial performance by incorporation of the neighbouring information as well as the spectral performance by more accurate unmixing results.

Appendices

A

List of Spectra Names Used in AVIRIS Dictionary

Actinolite, HS116.3B, s06av95a=b,
Adularia, GDS57, Orthoclase, s06av95a=b,
Albite, GDS30, 74-250um, Plag, s06av95a=b,
Allanite, HS293.3B, s06av95a=b,
Almandine, HS114.3B, Garnet, s06av95a=b,
Alunite, AL706, Na__, s06av95a=b,
Ammonio-Illite/Smectit, GDS87, s06av95a=b,
Ammonio-Jarosite, SCR-NHJ, s06av95a=a,
Ammonio-Smectite, GDS86, s06av95a=b,
Amphibole, NMNH78662, s06av95a=b,
Analcime, GDS1, Zeolite, s06av95a=a,
Andalusite, NMNHR17898, s06av95a=c,
Andesine, HS142.3B, s06av95a=c,
Andradite, GDS12, Garnet, s06av95a=c,
Anhydrite, GDS42, <250um, s06av95a=a,
Annite, WS661, Biotite, s06av95a=b,
Anorthite, GDS28, Syn, <74um, s06av95a=a,
Anthophyllite, HS286.3B, s06av95a=c,
Antigorite, NMNH17958, s06av95a=b,
Arsenopyrite, HS262.3B, s06av95a=c,
Augite, NMNH120049, s06av95a=b,
Axinite, HS342.3B, s06av95a=b,
Azurite, WS316, s06av95a=a,
Barite, HS79.3B, s06av95a=b,
Bassanite, GDS145, (syn), s06av95a=a,
Beryl, GDS9, <150um, gs, s06av95a=b,
Biotite, HS28.3B, s06av95a=b,
Bloedite, GDS147, s06av95a=a,
Bronzite, HS9.3B, Pyroxene, s06av95a=c,
Brookite, HS443.2B, s06av95a=b,
Brucite, HS247.3B, s06av95a=c,
Buddingtonite, GDS85, D-206, s06av95a=b,
Buddingtonite, NHB2301, s06av95a=b,
Bytownite, HS105.3B, Plagio, s06av95a=b,
Calcite, CO2004, s06av95a=b,
Carbon_Black, GDS68, sm.ap., s06av95a=a,
Carnallite, HS430.3B, s06av95a=a,
Cassiterite, HS279.3B, s06av95a=c,
Celestite, HS251.3B, Barite, s06av95a=b,
Celsian, HS200.3B, s06av95a=d,
Chalcedony, CU91-6A, s06av95a=a,
Chalcopyrite, HS431.3B, s06av95a=b,
Chert, ANP90-6D, (White), s06av95a=?,
Chlorapatite, WS423, s06av95a=b,
Chlorite, HS179.3B, s06av95a=b,
Chromite, HS281.3B, s06av95a=b,
Chrysocolla, HS297.3B, s06av95a=b,
Chrysotile, HS323.1B, s06av95a=a,
Cinnabar, HS133.3B, s06av95a=c,
Clinochlore, GDS158, Flagst, s06av95a=b,
Clinochlore_Fe, GDS157, s06av95a=a,
Clinoptilolite, GDS152, Zeolit, s06av95a=b,
Clinozoisite, HS299.2B, s06av95a=d,
Clintonite, NMNH126553, s06av95a=c,
Colemanite, GDS143, s06av95a=b,
Cookeite, CAr-1.a, 104-150um, s06av95a=b,
Copiapite, GDS21, s06av95a=b,
Coquimbite, GDS22, s06av95a=c,
Cordierite, HS346.3B, s06av95a=d,
Corrensite, CorWa-1, s06av95a=b,
Corundum, HS283.3B, s06av95a=c,
Covellite, HS477.2B, s06av95a=b,
Cronstedtite, M3542, s06av95a=b,
Cummingtonite, HS294.3B, s06av95a=c,
Cuprite, HS127.3B, s06av95a=b,
Datolite, HS442.3B, s06av95a=b,
Diaspore, HS416.3B, s06av95a=b,
Dickite, NMNH106242, s06av95a=b,
Diopside, HS15.3B, Pyroxene, s06av95a=c,
Dipyre, BM1959;505.HLsp, s06av95a=c,
Dolomite, COD2005, s06av95a=b,
Dumortierite, HS190.3B, s06av95a=c,
Elbaite, NMNH94217-1.a, 659, s06av95a=b,
Endellite, GDS16, s06av95a=b,
Enstatite, NMNH128288, s06av95a=c,
Epidote, BR93-33a, s06av95a=b,
Epsomite, GDS149, s06av95a=c,
Eugsterite, GDS140, Syn, s06av95a=b,
Europium_Oxide, GDS33, s06av95a=a,
Fassaite, HS118.3B, s06av95a=c,
Ferrihydrite, GDS75, Syn;, F6, s06av95a=b,
Fluorapatite, WS416, s06av95a=a,
Galena, HS37.3, s06av95a=b,
Gaylussite, NMNH102876-2, s06av95a=b,
Gibbsite, HS423.3B, s06av95a=b,
Glauconite, HS313.3B, s06av95a=c,
Glaucophane, HS426.3B, s06av95a=c,
Goethite, GDS134, s06av95a=b,
Grossular, HS113.3B-HCL, Garnt, s06av95a=d,
Gypsum, HS333.3B, (Selenite), s06av95a=a,
Halite, HS433.3B, s06av95a=a,
Halloysite, CM13, s06av95a=b,
Hectorite, SHCa-1, s06av95a=c,
Hedenbergite, HS10.3B, s06av95a=c,
Hematite, FE2602, s06av95a=b,
Heulandite, GDS3, s06av95a=a,
Holmquistite, HS291.3B, s06av95a=d,
Hornblende, HS16.3B, s06av95a=b,
Hornblende_Fe, HS115.3B, s06av95a=c,
Hornblende_Mg, NMNH117329, s06av95a=b,
Howlite, GDS155, s06av95a=a,

Hydrogrossular, NMNH120555, s06av95a=b,
Hydroxyl-Apatite, WS425, s06av95a=b,
Hypersthene, NMNHC2368, s06av95a=b,
Illite, GDS4, (Marblehead), s06av95a=b,
Ilmenite, HS231.3B, s06av95a=b,
Jadeite, HS343.3B, s06av95a=b,
Jarosite, GDS100, Na;Sy, 90C, s06av95a=a,
Kainite, NMNH83904, s06av95a=a,
Kaolinite, CM3, s06av95a=a,
Kieserite, KIEDE1.a, coarse, gr, s06av95a=c,
Knebelite, HS419.3B, s06av95a=b,
Labradorite, HS17.3B, s06av95a=b,
Laumontite, GDS5, Zeolite, s06av95a=b,
Lazurite, HS418.3B, s06av95a=b,
Lepidocrosite, GDS80, (Syn), s06av95a=b,
Lepidolite, HS167.3B, s06av95a=b,
Limonite, HS41.3, s06av95a=b,
Lizardite, NMNHR4687.a, 280, s06av95a=a,
Maghemite, GDS81, Syn, (M-3), s06av95a=b,
Magnetite, HS195.3B, s06av95a=b,
Malachite, HS254.3B, s06av95a=b,
Margarite, GDS106, s06av95a=c,
Marialite, NMNH126018-2, s06av95a=b,
Mascagnite, GDS65.a, (coar), s06av95a=a,
Meionite, WS700.HLsp, s06av95a=b,
Microcline, HS103.3B, Feldspar, s06av95a=c,
Mirabilite, GDS150, Na2SO4, s06av95a=a,
Mizzonite, BM1931;12, Scapolte, s06av95a=c,
Monazite, HS255.3B, s06av95a=c,
Monticellite, HS339.3B, s06av95a=b,
Montmorillonite, CM20, s06av95a=b,
Mordenite, GDS18, s06av95a=b,
Mordenite+Clinopt., GDS151, s06av95a=b,
Muscovite, GDS107, s06av95a=a,
Nacrite, GDS88, s06av95a=c,
Nanohematite, BR93-34B2, s06av95a=b,
Natrolite, HS169.3B, Zeolite, s06av95a=b,
Neodymium_Oxide, GDS34, s06av95a=a,
Nepheline, HS19.3, s06av95a=c,
Nephrite, HS296.3B, s06av95a=c,
Nickeline, HS264.3B, s06av95a=c,
Niter, GDS43, (K-Saltpeter), s06av95a=a,
Nontronite, NG-1.a, s06av95a=b,
Oligoclase, HS110.3B, s06av95a=c,
Olivine, GDS70.a, Fo89, 165um, s06av95a=b,
Opal, TM8896, (Hyalite), s06av95a=a,
Orthoclase, HS13.3B, s06av95a=c,
Palygorskite, CM46a, Attapulg, s06av95a=b,
Paragonite, GDS109, s06av95a=a,
Pectolite, NMNH94865.a, s06av95a=b,
Perthite, HS415.3B, s06av95a=c,
Phlogopite, GDS20, fine, fr, s06av95a=b,
Pigeonite, HS199.3B, s06av95a=b,
Pinnoite, NMNH123943, s06av95a=a,
Pitch_Limonite, GDS104, Cu, s06av95a=?,
Polyhalite, NMNH92669-4, s06av95a=a,
Portlandite, GDS525, Ca(OH)2, s06av95a=a,
Praseodymium_Oxide, GDS35, s06av95a=b,
Prehnite, GDS613.a, <60um, s06av95a=a,
Prochlorite, SMR-14.a, 115um, s06av95a=a,
Psilomelane, HS139.3B, s06av95a=b,
Pyrite, HS35.3, s06av95a=b,
Pyrolusite, HS138.3B, s06av95a=b,
Pyrophyllite, PYS1A, <850um, s06av95a=a,
Pyroxene, HS119.3B, s06av95a=c,
Pyrrhotite, HS269.3B, s06av95a=b,
Quartz, GDS31, 0-74um, fr, s06av95a=a,
Rectorite, ISR202, (RAr-1), s06av95a=?,
Rhodochrosite, HS338.3B, s06av95a=b,
Rhodonite, HS325.3B, s06av95a=c,
Richterite, HS336.3B, Amphibol, s06av95a=c,
Riebeckite, HS326.3B, Amphibol, s06av95a=d,
Rivadavite, NMNH170164, Amph, s06av95a=a,
Roscoelite, EN124, s06av95a=b,
Rutile, HS126.3B, s06av95a=c,
Samarium_Oxide, GDS36, s06av95a=a,
Sanidine, GDS19, Feldspar, s06av95a=a,
Saponite, SapCa-1, s06av95a=b,
Sauconite, GDS135, s06av95a=b,
Schwertmannite, BZ93-1, s06av95a=b,
Scolecite, GDS7, Zeolite, s06av95a=b,
Sepiolite, SepNev-1, s06av95a=b,
Serpentine, HS318.4B, s06av95a=c,
Siderite, HS271.3B, s06av95a=a,
Siderophyllite, NMNH104998, s06av95a=b,
Sillimanite, HS186.3B, s06av95a=c,
Smaragdite, HS290.3B, Amphibol, s06av95a=b,
Sodium_Bicarbonate, GDS55, s06av95a=a,
Spessartine, HS112.3B, Garnet, s06av95a=b,
Sphalerite, HS136.3B, s06av95a=b,
Sphene, HS189.3B, s06av95a=b,
Spodumene, HS210.3B, s06av95a=c,
Staurolite, HS188.3B, s06av95a=b,
Stilbite, GDS8, Zeolite, s06av95a=b,
Strontianite, HS272.3B, s06av95a=b,
Sulfur, GDS94, Reagent, s06av95a=a,
Syngenite, GDS139, s06av95a=a,
Talc, GDS23, 74-250um, fr, s06av95a=a,
Thenardite, GDS146, s06av95a=c,
Thuringite, SMR-15.a, 115um, s06av95a=b,
Tincalconite, GDS142, s06av95a=a,
Topaz, Cameron_Cone_# 42, s06av95a=b,
Tourmaline, HS282.2B, s06av95a=c,
Tremolite, HS18.3, s06av95a=c,
Trona, GDS148, s06av95a=a,
Ulexite, GDS138, Boron;, CA, s06av95a=a,
Uralite, HS345.3B, s06av95a=b,
Uvarovite, NMNH106661, Garnet, s06av95a=b,
Vermiculite, GDS13, Llano, s06av95a=a,
Vesuvianite, HS446.3B, Idocras, s06av95a=a,
Witherite, HS273.3B, s06av95a=a,
Wollastonite, HS348.3B, s06av95a=b,
Zircon, WS522, s06av95a=a,
Zoisite, HS347.3B, s06av95a=b,
Zunyite, GDS-241B, <150um, s06av95a=?,
Acid_Mine_Dr, Assemb2-Fe3+, s06av95a=b,
Actinolite-Hornfels, BR93-5a, s06av95a=c,
Actinolite-Tremolit, BR93-22C, s06av95a=b,
Actinolite_Dolomit, BR93-60B, s06av95a=b,
Alun.33+Kaol.33+Musc.33, AMX2, s06av95a=a,
Alun0.3+Musc0.4+Pyro0.3, AMX1, s06av95a=a,
Alun366+.50PyroPYS1A, GDS222, s06av95a=b,
Alun_Na+Kaol+Hemat, MV00-11a, s06av95a=c,
Alunite+Pyrophyl, SD1093A, s06av95a=b,
Alunite-K, CU91-217G1, HiTemp, s06av95a=b,
Alunite+Dickite, MV99-6-26b, s06av95a=c,
Alunite.5+MuscCU91-250A, AMX4, s06av95a=a,
Alunite0.35K+.65Na, CU91-217H, s06av95a=b,
Alunite0.5+Kaol_KGa-1, AMX3, s06av95a=b,
Alunite_K, CU98-5C, MedTemp, s06av95a=b,
Alunite_K-Na, CU91-217H1, LowT, s06av95a=b,
Alunite_NH4+Jaro, NMNH145596A, s06av95a=b,
Basalt_fresh, BR93-46B, s06av95a=b,
Basalt_weathered, BR93-43, s06av95a=b,
Beidellite+Montmor, GDS123, s06av95a=b,
Biotite-Chlorite_Mx, BR93-36A, s06av95a=b,
Blue_Efflorscnt_Min, SU93-300, s06av95a=b,
Calc.25+Dolo.25+Ca-Mon, AMX7, s06av95a=b,
Calc.25+dolo.25+mont.5, AMX18, s06av95a=b,
Calcite+.33Muscov, AMX5, Ruby, s06av95a=a,
Calcite+.50Ca-Mont, AMX6, s06av95a=b,
Calcite+Dolomite.5, AMX8, s06av95a=b,
Calcite+Talc, PC99-1G, s06av95a=c,
Calcite.33+Ca-mont.67, AMX19, s06av95a=b,
Calcite.33+Epidote.67, GDS311, s06av95a=a,
Calcite.67+Epidote.33, GDS310, s06av95a=a,
Calcite.7+Kaolwxl.3, AMX9, s06av95a=a,
Calcite.8+Ca-Montmor.2, AMX15, s06av95a=b,
Calcite.80+Mont_Swy-1, GDS212, s06av95a=a,
Calcite.80wt+Kaol_CM9, GDS213, s06av95a=a,
Chabazite+Thom+Wair, HS193.3B, s06av95a=b,
Chl.33+Epid.33+Cal.33, GDS319, s06av95a=a,
Chlor+Goethite, CU93-4B, Phyl, s06av95a=a,
Chlor.2+Epid.2+Calc.6, GDS314, s06av95a=a,
Chlor.2+Epid.6+Calc.2, GDS312, s06av95a=a,
Chlor.6+Epid.2+Calc.2, GDS313, s06av95a=a,
Chlorit.33+Calcite.67, GDS315, s06av95a=a,
Chlorite+Muscovite, CU93-65A, s06av95a=a,
Chlorite.33+Epidot.67, GDS318, s06av95a=a,
Chlorite.67+Calcit.33, GDS316, s06av95a=a,
Chlorite.67+Epidot.33, GDS317, s06av95a=a,
Chlorite_Phyllite, CU91-238A, s06av95a=b,
Chlorite_Serpentine, BR93-22B, s06av95a=b,
Dic.4+msc.3+gyp.2+jr.1, AMX20, s06av95a=a,
Dolomit+Calcite+Talc, PC99-1E, s06av95a=c,
Dolomite.5+Na-mont.5, AMX21, s06av95a=b,
Dolomite.50+Ca-Montmor, AMX10, s06av95a=b,
Erionite+Merlinoite, GDS144, s06av95a=c,
Erionite+Offretite, GDS72, s06av95a=b,
Fe-Hydroxide, SU93-106, amorph, s06av95a=b,
Goeth+qtz.5+Jarosite.5, AMX11, s06av95a=b,
Goethite0.02+Quartz, GDS240, s06av95a=a,
Goethite_Phyllite, CU91-236A, s06av95a=b,
Gyp+jar+ill, BRCM1, Marysvale, s06av95a=b,
Gyp.3+jr.1+msc.4+dic.2, AMX22, s06av95a=a,
Gyp.4+jr20+msc.2+dic.2, AMX23, s06av95a=a,
Gyp.5+Kjar.3+hAlmsc.2, AMX24, s06av95a=a,
Halloysite, CU91-242D, s06av95a=b,
Halloysite+Kaolinite, CM29, s06av95a=a,
Hematite.02+Quartz.98, GDS76, s06av95a=a,
Hematitic_Alt._Tuff, CU91-223, s06av95a=b,
Hydrated_Volc_Tuff, CU01-4A, s06av95a=c,
Illite, CU00-5B, Hi-Al+Quartz, s06av95a=a,
Jarosite_Rhyolite, CU91-20A, s06av95a=a,
Kalun+kaol+gth, mv2-ar3, s06av95a=b,
Kaol+Musc_intimate, CU93-5C, s06av95a=a,
Kaol.5+MuscCU91-250A, AMX13, s06av95a=b,
Kaol_Wxl+0.5Musc_Ruby, AMX12, s06av95a=a,
Kaol_wxl+others, CU00-19A, s06av95a=b,
Kaolin/Smect, KLF511, .12Kaol, s06av95a=b,
Kaolin_Smect, H89-FR-2, .5Kaol, s06av95a=b,
Kaolwxl.75+Alun_HS295, AMX14, s06av95a=b,
Limestone, CU02-11A, s06av95a=a,
Magnesite+Hydroma, HS47.3B, s06av95a=a,
Magnetite_skarn, BR93-5B, s06av95a=b,
Mesolite+Hydroxyapop, GDS6, s06av95a=b,
Montmorillonite+Illite, CM37, s06av95a=b,
Montmorillonite-Na, CU93-52A, s06av95a=c,
Muscov+Jaros, CU93-314, coatng, s06av95a=b,
Muscovite+Pyrophyl, JH_PYRP1, s06av95a=b,
Muscovite-low-Al, CU98-8H, s06av95a=b,
Muscovite-medhi-Al, CU91-252D, s06av95a=c,
Muscovite-medlowAl, CU91-250A, s06av95a=b,
Nontronite+others, CU00-13A, s06av95a=b,
Natrolite+Zeolite, HS168.3B, s06av95a=b,
Opalized, Tuff, CU00-15E, s06av95a=b,
Phlogopite_Sand_Mix, BR93-20, s06av95a=a,
Pyrite, LV95-6A, Weath, on, Tail, s06av95a=b,
Pyrophyl+Muscovite, JH_PYRM1, s06av95a=b,
Pyrophyl.25+wxlKaol.75, AMX17,

s06av95a=b,
Pyrophyl.50+Ca-Mont.50, AMX16, s06av95a=a,
Pyroxene_Basalt, CU01-20A, s06av95a=a,
Stonewall_Playa_Dry_Mud, 2001, s06av95a=a,
Stonewall_Playa, CU93-52A, a11, s06av95a=a,
Talc+Clinochlore, HS327.3B, s06av95a=a,
Teepleite+Trona, NMNH102798, s06av95a=a,
White_Crust, LV30, starkeyite, s06av95a=c,
Zincite+Franklin, HS147.3B, s06av95a=b,
Blck_Mn_Coat_Tailngs, LV95-3, s06av95a=b,
Desert_Varnish, ANP90-14, s06av95a=a,
Goethite_Thin_Film, WS222, s06av95a=a,
Hematite_Coatd_Qtz, BR93-25B, s06av95a=b,
Hematite_Coatd_Qtzt, BR93-25A, s06av95a=b,
Hematite_Thin_Film, GDS27, s06av95a=a,
Jarosite_Thin_Film, GDS243, s06av95a=b,
Jarosite_on_Qtzite, BR93-34A2, s06av95a=b,
H2O-Ice, GDS136, 77K, s06av95a=a,
Melting_snow, mSnw16+0.25_veg, s06av95a=a,
Seawater_Coast_Chl, SW1, s06av95a=a,
Seawater_Open_Ocean, SW2, lwch, s06av95a=a,
Water+Montmor, SWy-2+1.67g/l, s06av95a=a,
Ammonium_Chloride, GDS77, s06av95a=a,
Asphalt, GDS376, Blck_Road, old, s06av95a=a,
Asphalt_Shingle, GDS366, Tan, s06av95a=a,
Brick, GDS347, Paving, Tan, s06av95a=a,
Burlap_Fabric, GDS430, Brown, s06av95a=a,
Cardboard, GDS371, Brn, Corgted, s06av95a=a,
Nylon_Carpet, GDS535, LtBrown, s06av95a=a,
Cedar_Shake, GDS357, Fresh, s06av95a=a,
Cinder_Block, GDS356, Lg, Grey, s06av95a=a,
Coated_Steel_Girder, WTC01-8, s06av95a=a,
Concrete, GDS375, Lt, Gry, Road, s06av95a=a,
Cotton_Fabric, GDS437, White, s06av95a=a,
Cyanide_Trihydrate, CT1, s06av95a=a,
Cyanide_Zinc_Potassium, s06av95a=a,
Cyanide_Potassium_Ferro, s06av95a=a,
Fiberglass, GDS337, Grn, Roofng, s06av95a=a,
GalvanizedSheetMetal, GDS334, s06av95a=a,
Green_Slime, SM93-14A, Summitv, s06av95a=a,
Kerogen, BK-Cornell, s06av95a=a,
Montmorill+Benzene, SWy, 1ml, s06av95a=a,
Montmorill+TCE, SWy, saturated, s06av95a=a,
Montmorill+Toluene, SWy, .5ml, s06av95a=a,
Montmorill+Trichlor, SWy, 1ml, s06av95a=a,
Montmorill+Unleaded_Gas, SWy, s06av95a=a,
Nylon_Fabric, GDS431, Red, RpSt, s06av95a=a,
Nylon_Webbing, GDS428, OlvDrab, s06av95a=a,
Painted_Aluminum, GDS333, LgGr, s06av95a=a,
Particle_Board, GDS364, Fn, Gr, s06av95a=a,
Plastic, GGA-54, Grnhouse, Roof, s06av95a=a,
Plastic_HDPE, GDS351, BlkSheet, s06av95a=a,
Plastic_LDPE, GDS402, Clr, film, s06av95a=a,
Plastic_PETE, GDS379, TrnslBrn, s06av95a=a,
Plastic_PVC, GDS338, White, s06av95a=a,
Plastic_Pipe, GDS344, Blue, s06av95a=a,
Plastic_Tarp, GDS339, Green, s06av95a=a,
Plastic_Tyvek, GDS369, White, s06av95a=a,
Plastic_Vinyl, GDS372, White, s06av95a=a,
Plastic_Visqueen, GDS370, Clr, s06av95a=a,
Plywood, GDS365, Fresh, Pine, s06av95a=a,
Polyester_Pile, GDS434, Blk, s06av95a=a,
Polyester_Webbing, GDS429, Blk, s06av95a=a,
Polystyrene, GDS345, BluInsul, s06av95a=a,
Renyolds_TnlSldgWet, SM93-15w, s06av95a=a,
Renyolds_Tnl_Sludge, SM93-15, s06av95a=a,
Roofing_Felt, GDS377, Black, s06av95a=a,
Rusted_Tin_Can, GDS378, MV99-6, s06av95a=a,
Sheet_Metal, GDS352, crg, Galvn, s06av95a=a,
Strand_Board, GDS362, Oriented, s06av95a=a,
Tar_Paper, GDS285A, New, Blk, s06av95a=a,
Terrycloth_Fabric, GDS537, Yl, s06av95a=a,
Wood_Beam, GDS363, Nw, Pine, 2X4, s06av95a=a,
WTC_Dust_Debris, WTC01-2, s06av95a=a,
Aspen, YNP-AS-1, s06av95a=b,
Aspen_Leaf-A, DW92-2, s06av95a=a,
Aspen_Leaf-B, DW92-3, s06av95a=a,
Bacterial-Mat, YNP-B1, s06av95a=b,
Blackbrush, ANP92-9A, leaves, s06av95a=a,
Blue_Spruce, DW92-5, needle, s06av95a=a,
Cattail, YNP-CT-1, s06av95a=b,
Cheatgrass, ANP92-11A, s06av95a=a,
Conifer-Meadow-Mix, YNP-CM-1, s06av95a=b,
Douglas-Fir, YNP-DF-1, s06av95a=b,
Dry_Long_Grass, AV87-2, s06av95a=a,
Engelmann-Spruce, ES-Needls-1, s06av95a=a,
Espruce-Sfir, YNP-SF-1, s06av95a=b,
Fir_Tree, IH91-2, s06av95a=a,
Grass-Fescue-Wheatg, YNP-FW-1, s06av95a=b,
Grass-FescueNeedleg, YNP-FN-1, s06av95a=b,
Grass-Smoothbrome, YNP-SB-1, s06av95a=b,
Grass_Golden_Dry, GDS480, s06av95a=a,
Juniper_Bush, IH91-4B, s06av95a=a,
Lawn_Grass, GDS91, (Green), s06av95a=a,
Lodgepole-Pine, LP-Needles-1, s06av95a=a,
Maple_Leaves, DW92-1, s06av95a=a,
Oak, Oak-Leaf-1, fresh, s06av95a=a,
Pinon_Pine, ANP92-14A, needle, s06av95a=a,
Rabbitbrush, ANP92-27, s06av95a=a,
Russian_Olive, DW92-4, s06av95a=a,
Sage_Brush, IH91-1B, s06av95a=a,
Sagebrush, Sage-Leaves-1, dry, s06av95a=a,
Saltbrush, ANP92-31A, s06av95a=a,
Sedge, YNP-SE-1, s06av95a=b,
Tumbleweed, ANP92-2C, Dry, s06av95a=a,
Walnut_Leaf, SUN, (Green), s06av95a=a,
Wetland, YNP-WT-1, s06av95a=b,
Whitebark-Pine, YNP-WB-1, s06av95a=b,
Willow, Willow-Leaves-1, dry, s06av95a=a,
Willow-Sedge-Mix, YNP-WS-1, s06av95a=b,
Antigorite+.2DryGrass, AMX26, s06av95a=a,
Antigorite+.33DryGrass, AMX25, s06av95a=a,
Grass_dry.4+.6green, AMX27, s06av95a=a,
Grass_dry.5+.5green, AMX28, s06av95a=a,
Grass_dry.6+.4green, AMX29, s06av95a=a,
Grass_dry.7+.3green, AMX30, s06av95a=a,
Grass_dry.8+.2green, AMX31, s06av95a=a,
Grass_dry.9+.1green, AMX32, s06av95a=a,
Lawn_Grass, GDS91, shifted, 3nm, s06av95a=a,
Stonwll_Ply+.1grnGrass, AMX33, s06av95a=a,
Stonwll_Ply+.2grnGrass, AMX34, s06av95a=a,
Willow_Dead, FluvTailSite_A, s06av95a=a

B

List of Spectra Names Used in HyMAP Dictionary

10a-o	6	White rubberized coating
10a-u	7	Olive green gloss paint
10b-o	8	Copper Metal
10b-u	9-o	Cinders ashen
11	9-u	White Marble
12	Black tar paper	Reddish asphalt Shingle
13	Black gloss paint	Construction Asphalt
14	Plate Window Glass	Black tar paper
15	Construction Concrete	Construction Concrete
16	Asphalt roofing shingle	Olive green paint
17	Bare Red Brick	Olive green gloss paint
18	Olive green paint	Galvanized Steel Metal
19-o	Construction Concrete	Construction Concrete
19-u	Pine Wood	Construction Concrete
1	Red smooth-faced Brick	Slate stone Shingle
20	Terra cotta Tiles	Black unspecified rubber
21	Asphaltic concrete	Dry grass
22	Aluminum Metal	Grass
23	Asphalt Shingle	Conifer
24	White fiberglass unspecified rubber	Decidous
25	Construction Tar	Dark grayish brown silty loam
26	Black gloss paint	Brown to dark brown sand
2a	Construction Asphalt	Very dark grayish brown loam
2b	Copper Metal	Gray silty clay
2c-o	Copper Metal	Dark reddish brown organic-rich silty loam
2c-u	Construction Asphalt	Black loam
30-alc	Black paint	Dark brown interior moist clay loam
31-alc	Black gloss paint	Brown sandy loam
40	Oxidized Galvanized Steel Metal	Brown to dark brown sandy loam
4a	Weathered Red Brick	Dark reddish brown fine sandy loam
4b-o	Galvanized Steel Metal	Brown to dark brown clay
4b-u	Construction Tar	Reddish brown fine sandy loam
5-o	Pine Wood	Brown loamy fine sand
5-u	Reddish Asphalt roofing shingle	Pale brown dry silty clay loam

Dark yellowish brown micaceous loam
Brown to dark brown silt loam
Brown to dark brown loamy sand
Brown sandy loam
Very dark grayish brown silty loam
White gypsum dune sand
Brown fine sandy loam
Dark brown fine sandy loam
Vary dark grayish brown loam

Brown gravelly sandy loam
Reddish brown fine sandy loam
Light yellowish brown interior dry gravelly loam
Very pale brown to brownish yellow interior dry gravelly silt loam
Light yellowish brown loamy sand
Brown to dark brown gravelly loam
Very dark grayish brown loam
Brown to dark brown gravelly fine sandy loam
Grayish brown loam
Very dark grayish brown silty loam

Very dark grayish brown loamy sand
Pale brown silty loam
Dark yellowish brown silty clay
Light yellowish brown loam
Light yellowish brown clay
Brown fine sandy loam
Brown silty loam
Gray/dark brown extremely stoney coarse sandy

Bibliography

Alparone, L., Wald, L., Chanussot, J., Thomas, C., Gamba, P., and Bruce, L. (2007). Comparison of pansharpening algorithms: Outcome of the 2006 grs-s data-fusion contest. *Geoscience and Remote Sensing, IEEE Transactions on*, 45(10):3012–3021.

Bach, F., Jenatton, R., Mairal, J., Obozinski, G., et al. (2011). Convex optimization with sparsity-inducing norms. *Optimization for Machine Learning*, pages 19–53.

Bachmann, M. U. (2007). *Automatisierte Ableitung von Bodenbedeckungsgraden durch MESMA-Entmischung*. PhD thesis, Bayerische Julius-Maximilians-Universität Würzburg.

Baraniuk, R. (2007). Compressive sensing. *IEEE Signal Processing Mag*, 24:118–120.

Baraniuk, R., Candes, E., Nowak, R., and Vetterli, M. (2008). Compressive sampling. *Signal Processing Magazine, IEEE*, 25(2):12–13.

Baron, D., Duarte, M. F., Sarvotham, S., Wakin, M. B., and Baraniuk, R. G. (2005). An information theoretic approach to distributed compressed sensing. In *Allerton Conference on Communication, Control, and Computing*.

Baron, D., Duarte, M. F., Wakin, M. B., Sarvotham, S., and Baraniuk, R. G. (2009). Distributed compressive sensing. *CoRR*, abs/0901.3403.

Ben-Haim, Z., Eldar, Y.C., and Elad, M. (2010). Coherence-based performance guarantees for estimating a sparse vector under random noise. *Signal Processing, IEEE Transactions on*, 58:5030–5043.

Bendoumi, M., He, M., and Mei, S. (2014). Hyperspectral image resolution enhancement using high-resolution multispectral image based on spectral unmixing. *Geoscience and Remote Sensing, IEEE Transactions on*, 52(10):6574–6583.

Bieniarz, J., Aguilera, E., Zhu, X., Müller, R., and Reinartz, P. (2015). Joint sparsity model for multilook hyperspectral image unmixing. *Geoscience and Remote Sensing Letters, IEEE*, 12(4):696–700.

Bieniarz, J., D.Cerra, Avbelj, J., Reinartz, P., and Müller, R. (2011). Hyperspectral image resolution enhancement based on spectral unmixing and information fusion. In *ISPRS Hannover Workshop 2011*.

Bieniarz, J., Müller, R., Zhu, X. X., Heiden, U., and Reinartz, P. (2014). Hyperspectral image resolution enhancement based on jointly sparse spectral unmixing. In *Geoscience and Remote Sensing Symposium (IGARSS), 2014 IEEE International*.

Bieniarz, J., Müller, R., Zhu, X. X., and Reinartz, P. (2012). On the use of overcomplete dictionaries for spectral unmixing. In *4th Workshop on Hyperspectral Image and Signal Processing. WHISPERS 2012*.

Bioucas-Dias, J. (2009). A variable splitting augmented lagrangian approach to linear spectral unmixing. pages 1 –4.

Bioucas-Dias, J. (2012). MATLAB code for SUnSAL-TV.

Bioucas-Dias, J. and Nascimento, J. (2008). Hyperspectral subspace identification. *Geoscience and Remote Sensing, IEEE Transactions on*, 46(8):2435–2445.

Bioucas-Dias, J. and Plaza, A. (2011). An overview on hyperspectral unmixing: Geometrical, statistical, and sparse regression based approaches. In *Geoscience and Remote Sensing Symposium (IGARSS), 2011 IEEE International*, pages 1135 –1138.

Bioucas-Dias, J., Plaza, A., Camps-Valls, G., Scheunders, P., Nasrabadi, N., and Chanussot, J. (2013). Hyperspectral remote sensing data analysis and future challenges. *IEEE Geoscience and Remote Sensing Magazine*, 1:6–36.

Bioucas-Dias, J., Plaza, A., Dobigeon, N., Parente, M., Du, Q., Gader, P., and Chanussot, J. (2012). Hyperspectral unmixing overview: Geometrical, statistical, and sparse regression-based approaches. *Selected Topics in Applied Earth Observations and Remote Sensing, IEEE Journal of*, 5(2):354 –379.

Bro, R. and De Jong, S. (1997). A fast non-negativity-constrained least squares algorithm. *Journal of Chemometrics*, 11:393–401.

Bruckstein, A. M., Elad, M., and Zibulevsky, M. (2008). Sparse non-negative solution of a linear system of equations is unique. In *Proc. 3rd Int. Symp. Communications, Control and Signal Processing ISCCSP 2008*, pages 762–767.

Candes, E. and Wakin, M. (2008). An introduction to compressive sampling. *Signal Processing Magazine, IEEE*, 25(2):21–30.

Cands, E. J. and Romberg, J. (2006). Sparsity and incoherence in compressive sampling. *Inverse Problems*, 23:969–985.

Canham, K., Schlamm, A., Ziemann, A., Basener, B., and Messinger, D. (2011). Spatially adaptive hyperspectral unmixing. *Geoscience and Remote Sensing, IEEE Transactions on*, 49(11):4248–4262.

Capobianco, L., Garzelli, A., Nencini, F., Alparone, L., and Baronti, S. (2007). Spatial enhancement of hyperion hyperspectral data through ali panchromatic image. In *Geoscience and Remote Sensing Symposium, 2007. IGARSS 2007. IEEE International*, pages 5158–5161.

Cerra, D., Müller, R., and Reinartz, P. (2014). Noise reduction in hyperspectral images through spectral unmixing. *Geoscience and Remote Sensing Letters, IEEE*, 11(1):109–113.

Chang, C.-I. and Du, Q. (2004). Estimation of number of spectrally distinct signal sources in hyperspectral imagery. *Geoscience and Remote Sensing, IEEE Transactions on*, 42(3):608–619.

Chang, C.-I., Zhao, X.-L., Althouse, M., and Pan, J. J. (1998). Least squares subspace projection approach to mixed pixel classification for hyperspectral images. *Geoscience and Remote Sensing, IEEE Transactions on*, 36(3):898–912.

Chen, F. and Zhang, Y. (2013). Sparse hyperspectral unmixing based on constrained lp - l2 optimization. *Geoscience and Remote Sensing Letters, IEEE*, 10(5):1142–1146.

Chen, G. and Qian, S.-E. (2011). Denoising of hyperspectral imagery using principal component analysis and wavelet shrinkage. *Geoscience and Remote Sensing, IEEE Transactions on*, 49(3):973–980.

Chen, S. S., Donoho, D. L., Michael, and Saunders, A. (1998). Atomic decomposition by basis pursuit. *SIAM Journal on Scientific Computing*, 20:33–61.

Chen, Z., Pu, H., Wang, B., and Jiang, G.-M. (2014). Fusion of hyperspectral and multispectral images: A novel framework based on generalization of pan-sharpening methods. *Geoscience and Remote Sensing Letters, IEEE*, 11(8):1418–1422.

Clark, R., Swayze, G., Wise, R., Livo, E., Hoefen, T., R. Kok, R., and Sutley, S. (2007). Usgs digital spectral library splib06a. Digital Data Series 231.

Clark, R. N., Swayze, G. A., Livo, K. E., Kokaly, R. F., Sutley, S. J., Dalton, J. B., McDougal, R. R., and Gent., C. A. (2003). Imaging spectroscopy: Earth and planetary remote sensing with the usgs tetracorder and expert systems. *Journal of Geophysical Research*, 108:5131.

Cocks, T., Jenssen, R., Stewart, A., Wilson, I., and Shields, T. (1998). The hymap (tm) airborne hyperspectral sensor: the system, calibration and performance. In *1 st EARSeL Workshop on Imaging Spectroscopy. EARSeL*.

Datt, B., McVicar, T., Van Niel, T., Jupp, D. L. B., and Pearlman, J. (2003). Preprocessing eo-1 hyperion hyperspectral data to support the application of agricultural indexes. *Geoscience and Remote Sensing, IEEE Transactions on*, 41(6):1246–1259.

Debba, P., Carranza, E. J. M., van der Meer, F., and Stein, A. (2006). Abundance estimation of spectrally similar minerals by using derivative spectra in simulated annealing. *Geoscience and Remote Sensing, IEEE Transactions on*, 44(12):3649–3658.

Dobigeon, N., Moussaoui, S., Coulon, M., Tourneret, J.-Y., and Hero, A. (2009). Joint bayesian endmember extraction and linear unmixing for hyperspectral imagery. *Signal Processing, IEEE Transactions on*, 57(11):4355–4368.

Donoho, D. L. and Elad, M. (2003). Optimally sparse representation in general (nonorthogonal) dictionaries via 1 minimization. *Proceedings of the National Academy of Sciences of the United States of America*, 100:2197–2202.

Donoho, D. L., Elad, M., and Temlyakov, V. N. (2006). Stable recovery of sparse overcomplete representations in the presence of noise. *Information Theory, IEEE Transactions on*, 52(1):6–18.

Donoho, D. L. and Tanner, J. (2005). Sparse nonnegative solutions of underdetermined linear equations by linear programming. In *Proceedings of the National Academy of Sciences*, pages 9446–9451.

Drake, N. A., Mackin, S., and Settle, J. J. (1999). Mapping vegetation, soils, and geology in semiarid shrublands using spectral matching and mixture modeling of swir aviris imagery. *Remote Sensing of Environment*, 68:1225.

Efron, B., Hastie, T., Johnstone, I., and Tibshirani, R. (2004). Least angle regression. *Annals of statistics*, 32(2):407499.

Ehlers, M. (2008). Multi-image fusion in remote sensing: spatial enhancement vs. spectral characteristics preservation. In *Advances in Visual Computing*, pages 75–84. Springer.

Eismann, M. and Hardie, R. (2004). Application of the stochastic mixing model to hyperspectral resolution enhancement. *Geoscience and Remote Sensing, IEEE Transactions on*, 42(9):1924–1933.

Eismann, M. and Hardie, R. (2005a). Hyperspectral resolution enhancement using high-resolution multispectral imagery with arbitrary response functions. *Geoscience and Remote Sensing, IEEE Transactions on*, 43(3):455–465.

Eismann, M. and Hardie, R. (2005b). Hyperspectral resolution enhancement using high-resolution multispectral imagery with arbitrary response functions. *Geoscience and Remote Sensing, IEEE Transactions on*, 43(3):455 – 465.

Elad, M. (2007). Optimized projections for compressed sensing. *Signal Processing, IEEE Transactions on*, 55(12):5695–5702.

Elad, M. (2010). *Sparse and Redundant Representations: From Theory to Applications in Signal and Image Processing*. Springer Publishing Company, Incorporated.

Gonzalez, R. C. and Woods, R. E. (2001). *Digital Image Processing*. Addison-Wesley Longman Publishing Co., Inc.

Greer, J. B. (2012). Sparse demixing of hyperspectral images. 21(1):219–228.

Gribonval, R. and Nielsen, M. (2003). Sparse representations in unions of bases. *Information Theory, IEEE Transactions on*, 49:3320–3325.

Grohnfeldt, C., Zhu, X. X., and Bamler, R. (2013). Jointly sparse fusion of hyperspectral and multispectral imagery. In *Geoscience and Remote Sensing Symposium (IGARSS), 2013 IEEE International*. IEEE.

Grohnfeldt, C., Zhu, X. X., and Bamler, R. (2014). Hyperspectral resolution enhancement using high resolution multispectral data - a comparison of the state-of-the-art fusion methods. In *Geoscience and Remote Sensing Symposium (IGARSS), IEEE International*.

Guo, Z., Wittman, T., and Osher, S. (2009). L1 unmixing and its application to hyperspectral image enhancement. In *Society of Photo-Optical Instrumentation Engineers (SPIE) Conference Series*, volume 7334 of *Presented at the Society of Photo-Optical Instrumentation Engineers (SPIE) Conference*.

Halimi, A., Altmann, Y., Dobigeon, N., and Tourneret, J.-Y. (2011). Nonlinear unmixing of hyperspectral images using a generalized bilinear model. *Geoscience and Remote Sensing, IEEE Transactions on*, 49:4153–4162.

Hardie, R., Eismann, M., and Wilson, G. (2004a). Map estimation for hyperspectral image resolution enhancement using an auxiliary sensor. *Image Processing, IEEE Transactions on*, 13(9):1174–1184.

Hardie, R., Eismann, M., and Wilson, G. (2004b). Map estimation for hyperspectral image resolution enhancement using an auxiliary sensor. *Image Processing, IEEE Transactions on*, 13(9):1174 –1184.

Heiden, U., Segl, K., Roessner, S., and Kaufmann, H. (2005). Determination and verification of robust spectral features for an automated classification of sealed urban surfaces. In *Proceedings of the 4th EARSeL Workshop on Imaging Spectroscopy in Warsaw*.

Heinz, D. and Chein-I-Chang (2001). Fully constrained least squares linear spectral mixture analysis method for material quantification in hyperspectral imagery. *Geoscience and Remote Sensing, IEEE Transactions on*, 39(3):529 –545.

Heylen, R., Burazerovic, D., and Scheunders, P. (2011a). Fully constrained least squares spectral unmixing by simplex projection. *Geoscience and Remote Sensing, IEEE Transactions on*, 49(11):4112–4122.

Heylen, R., Burazerovic, D., and Scheunders, P. (2011b). Non-linear spectral unmixing by geodesic simplex volume maximization. *Selected Topics in Signal Processing, IEEE Journal of*, 5:534–542.

Hogan, R., Marzo, G., and Roush, T. (2009). A comparison of performance between two cluster algorithms applied to mineral spectra. In *Aerospace conference, 2009 IEEE*, pages 1–7.

Horwitz, H. M., Nalepka, R. F., Hyde, P. D., and Morgenstern, J. P. (1971). Estimating the proportions of objects within a single resolution element of a multispectral scanner. In *In Proceedings of the 7th International Symposium on Remote Sensing of Environment*.

Ifarraguerri, A. and Chang, C.-I. (1999). Multispectral and hyperspectral image analysis with convex cones. *Geoscience and Remote Sensing, IEEE Transactions on*, 37(2):756 –770.

Iordache, D. M., Bioucas-Dias, J., and Plaza, A. (2011). Sparse unmixing of hyperspectral data. *Geoscience and Remote Sensing, IEEE Transactions on*, 49(6):2014–2039.

Iordache, D. M., Bioucas-Dias, J., and Plaza, A. (2012a). Dictionary pruning in sparse unmixing of hyperspectral data. In *4th Workshop on Hyperspectral Image and Signal Processing. WHISPERS 2012*.

Iordache, M., Bioucas-Dias, J., and Plaza, A. (2010). Recent developments in sparse hyperspectral unmixing. In *IEEE International Geoscience and Remote Sensing Symposium IGARSS*.

Iordache, M.-D., Bioucas-Dias, J., and Plaza, A. (2009). Unmixing sparse hyperspectral mixtures. volume 4, pages IV–85 –IV–88.

Iordache, M.-D., Bioucas-Dias, J., and Plaza, A. (2012b). Total variation spatial regularization for sparse hyperspectral unmixing. *Geoscience and Remote Sensing, IEEE Transactions on*, 50(11):4484–4502.

Iordache, M.-D., Bioucas-Dias, J., and Plaza, A. (2013). Collaborative sparse regression for hyperspectral unmixing. *Geoscience and Remote Sensing, IEEE Transactions on*, PP(99):1–14.

Iordache, M.-D., Bioucas-Dias, J., Plaza, A., and Somers, B. (2014). Music-csr: Hyperspectral unmixing via multiple signal classification and collaborative sparse regression. *Geoscience and Remote Sensing, IEEE Transactions on*, 52(7):4364–4382.

Jenatton, R., Mairal, J., Obozinski, G., and Bach, F. (2010). Proximal Methods for Sparse Hierarchical Dictionary Learning. *ICML 2010: Proceedings of the 27th international conference on Machine learning*, pages 1–8.

Jia, S. and Qian, Y. (2007). Spectral and spatial complexity-based hyperspectral unmixing. *Geoscience and Remote Sensing, IEEE Transactions on*, 45(12):3867–3879.

Jia, S. and Qian, Y. (2009). Constrained nonnegative matrix factorization for hyperspectral unmixing. *Geoscience and Remote Sensing, IEEE Transactions on*, 47(1):161 –173.

JPL, A. (1997). http://aviris.jpl.nasa.gov/html/aviris.freedata.html.

Kawakami, R., Wright, J., Tai, Y.-W., Matsushita, Y., Ben-Ezra, M., and Ikeuchi, K. (2011). High-resolution hyperspectral imaging via matrix factorization. In *Computer Vision and Pattern Recognition (CVPR), 2011 IEEE Conference on*, pages 2329 – 2336.

Keshava, N. (2003). A survey of spectral unmixing algorithms a survey of spectral unmixing. *Lincoln Laboratory Jurnal*, 14:55–78.

Keshava, N. and Mustard, J. (2002). Spectral unmixing. *Signal Processing Magazine, IEEE*, 19(1):44 –57.

Kruse, F. A., Lefkoff, A. B., Boardman, J. B., Heidebrecht, K. B., Shapiro, A. T., Barloon, P. J., and Goetz, A. F. H. (1993). The Spectral Image Processing System (SIPS) - Interactive Visualization and Analysis of Imaging Spectrometer Data. *Remote Sensing of Environment*, 44:145–163.

Lawson, C. L. and Hanson, R. J. (1974). *Solving least squares problems*. 3 edition.

Licciardi, G., Khan, M., Chanussot, J., Montanvert, A., Condat, L., and Jutten, C. (2012). Fusion of hyperspectral and panchromatic images using multiresolution analysis and nonlinear pca band reduction. *EURASIP Journal on Advances in Signal Processing*, 2012(1):1–17.

Ma, W.-K., Bioucas-Dias, J., Chan, T.-H., Gillis, N., Gader, P., Plaza, A., Ambikapathi, A., and Chi, C.-Y. (2014). A signal processing perspective on hyperspectral unmixing: Insights from remote sensing. *Signal Processing Magazine, IEEE*, 31:67–81.

Mailhé, B., Gribonval, R., Vandergheynst, P., and Bimbot, F. (2011). Fast orthogonal sparse approximation algorithms over local dictionaries. *Signal Processing*, 91(12):2822–2835.

Mairal, J., Bach, F., Ponce, J., and Sapiro, G. (2010). Online learning for matrix factorization and sparse coding. *Journal of Machine Learning Research*, 11:19–60.

Mayumi, N. and Iwasaki, A. (2011). Image sharpening using hyperspectral and multispectral data. In *Geoscience and Remote Sensing Symposium (IGARSS), 2011 IEEE International*, pages 519–522. IEEE.

McEwen, A. S., Eliason, E. M., Bergstrom, J. W., Bridges, N. T., Hansen, C. J., Delamere, W. A., Grant, J. A., Gulick, V. C., Herkenhoff, K. E., Keszthelyi, L., et al. (2007). Mars reconnaissance orbiter's high resolution imaging science experiment (hirise). *Journal of Geophysical Research: Planets (1991–2012)*, 112(E5).

McKeown Jr, D. M., Cochran, S. D., Ford, S. J., McGlone, J. C., Shufelt, J. A., and Yocum, D. A. (1999). Fusion of hydice hyperspectral data with panchromatic imagery for cartographic feature extraction. *Geoscience and Remote Sensing, IEEE Transactions on*, 37(3):1261–1277.

Meinshausen, N. (2013). Sign-constrained least squares estimation for high-dimensional regression. *Electronic Journal of Statistics*, 7:1607–1631.

Michalski, J. R., Bibring, J.-P., Poulet, F., Loizeau, D., Mangold, N., Dobrea, E. N., Bishop, J. L., Wray, J. J., McKeown, N. K., Parente, M., et al. (2010). The mawrth vallis region of mars: A potential landing site for the mars science laboratory (msl) mission. *Astrobiology*, 10(7):687–703.

Müller, R., Lehner, M., Müller, R., Reinartz, P., Schroeder, M., and Vollmer, B. (2002). A program for direct georeferencing of airborne and spaceborne line scanner images. In *Proceedings of the ISPRS Commission I Symposium; Integrating Remote Sensing at the Global, Regional and Local Scale*, pages 148–153.

Müller, R., Reinartz, P., Kritikos, G., and Schroeder, M. (1993). Image processing in a network environment. *International Archives of Photogrammetry and Remote Sensing*, 29:1–5.

Murchie, S., Arvidson, R., Bedini, P., Beisser, K., Bibring, J.-P., Bishop, J., Boldt, J., Cavender, P., Choo, T., Clancy, R., et al. (2007). Compact reconnaissance imaging spectrometer for mars (crism) on mars reconnaissance orbiter (mro). *Journal of Geophysical Research: Planets (1991–2012)*, 112(E5).

Murphy, K. (2012). *Machine Learning: A Probabilistic Perspective*. Adaptive computation and machine learning series. MIT Press.

Nascimento, J. and Dias, J. (2005). Vertex component analysis: a fast algorithm to unmix hyperspectral data. *Geoscience and Remote Sensing, IEEE Transactions on*, 43(4):898 – 910.

Neitz, J., Carroll, J., and Neitz, M. (2001). Almost reason enough for having eyes. *Optics & Photonics News*, 27.

Nielsen, A. A. (2001). Spectral mixture analysis: Linear and semi-parametric full and iterated partial unmixing in multi- and hyperspectral image data. *J. Math. Imaging Vis.*, 15(1-2):17–37.

Parente, M. and Zymnis, A. (2005). Statistical clustering and mineral spectral unmixing in aviris hyperspectral image of cuprite, nv. Technical Report CS229, Stanford University.

Plaza, A., Martinez, P., Perez, R., and Plaza, J. (2002). Spatial/spectral endmember extraction by multidimensional morphological operations. *Geoscience and Remote Sensing, IEEE Transactions on*, 40(9):2025–2041.

Pu, H., Xia, W., Wang, B., and Jiang, G.-M. (2014). A fully constrained linear spectral unmixing algorithm based on distance geometry. *Geoscience and Remote Sensing, IEEE Transactions on*, 52(2):1157–1176.

Ramachandran, V., Mitchell, H., Jacobs, S., Tzeng, N., Firpi, A., and Rodriguez, B. (2014). Spectral comparison using k-means clustering. In *Aerospace Conference, 2014 IEEE*, pages 1–10.

Richards, J. A. and Jia, X. (1999). *Remote Sensing Digital Image Analysis: An Introduction*. Springer-Verlag New York, Inc., Secaucus, NJ, USA, 3rd edition.

Richter, R. and Schläpfer, D. (2011). *Atmospheric / Topographic Correction for Airborne Imagery*. DLR, report dlr-ib 565-02/11 edition.

Robinson, G. D. (1997). Evaluation of two applications of spectral mixing models to image fusion. Master's thesis, AIR FORCE INST OF TECH WRIGHT-PATTERSON AFB OH.

Robinson, G. D., Gross, H. N., and Schott, J. R. (2000). Evaluation of two applications of spectral mixing models to image fusion. *Remote Sensing of Environment*, 71(3):272 – 281.

Rogge, D., Rivard, B., Zhang, J., and Feng, J. (2006). Iterative spectral unmixing for optimizing per-pixel endmember sets. *Geoscience and Remote Sensing, IEEE Transactions on*, 44(12):3725–3736.

Saper, L. and Bishop, J. (2011). Reflectance spectroscopy of nontronite and ripidolite mineral mixtures in context of phyllosilicate unit composition at mawrth vallis. In *Lunar and Planetary Science Conference*, volume 42, page 2029.

Schowengerdt, R. A. (2006). *Remote sensing: models and methods for image processing*. Academic press.

Segl, K., Guanter, L., Kaufmann, H., Schubert, J., Kaiser, S., Sang, B., and Hofer, S. (2010). Simulation of spatial sensor characteristics in the context of the enmap hyperspectral mission. *Geoscience and Remote Sensing, IEEE Transactions on*, 48(7):3046–3054.

Settle, J. and Drake, N. (1993). Linear mixing and the estimation of ground cover proportions. *International Journal of Remote Sensing*, 14(6):1159–1177.

Shaw, G. A. and Burke, H. K. (2003). Spectral imaging for remote sensing. *Lincoln Laboratory Journal*, 14(1):3–28.

Shimabukuro, Y. and Smith, A. (1991). The least-squares mixing models to generate fraction images derived from remote sensing multispectral data. *Geoscience and Remote Sensing, IEEE Transactions on*, 29(1):16–20.

Smith, K., Steven, M., and Colls, J. (2004). Use of hyperspectral derivative ratios in the red-edge region to identify plant stress responses to gas leaks. *Remote sensing of environment*, 92(2):207–217.

Starck, J.-L., Murtagh, F., and Fadili, J. M. (2010). *Sparse Image and Signal Processing: Wavelets, Curvelets, Morphological Diversity*. New York : Springer.

Stathaki, T. (2011). *Image fusion: algorithms and applications*. Academic Press.

Swayze, G. A., Clark, R. N., Goetz, A. F., Livo, K. E., Breit, G. N., Kruse, F. A., Sutley, S. J., Snee, L. W., Lowers, H. A., Post, J. L., Stoffregen, R. E., and Ashley, R. P. (2014). Mapping advanced argillic alteration at cuprite, nevada, using imaging spectroscopy. *Economic Geology*, 109(5):1179–1221.

Talsky, G. (1994). *Derivative Spectrophotometry of First and Higher Orders*. VCH Verlagsgesellschaft mbH, Weinheim (Federal Republic of Germany) VCH Publishers, Inc., New York, NY (USA).

Tang, W., Shi, Z., and Duren, Z. (2014a). Sparse hyperspectral unmixing using an approximate {L0} norm. *Optik - International Journal for Light and Electron Optics*, 125(1):31 – 38.

Tang, W., Shi, Z., and Wu, Y. (2014b). Regularized simultaneous forward-backward greedy algorithm for sparse unmixing of hyperspectral data. *Geoscience and Remote Sensing, IEEE Transactions on*, 52(9):5271–5288.

Tang, W., Shi, Z., Wu, Y., and Zhang, C. (2015). Sparse unmixing of hyperspectral data using spectral a priori information. *Geoscience and Remote Sensing, IEEE Transactions on*, 53(2):770–783.

Themelis, K., Rontogiannis, A., and Koutroumbas, K. (2012). A novel hierarchical bayesian approach for sparse semisupervised hyperspectral unmixing. *Signal Processing, IEEE Transactions on*, 60(2):585–599.

Thomas, C., Ranchin, T., Wald, L., and Chanussot, J. (2008). Synthesis of multispectral images to high spatial resolution: A critical review of fusion methods based on remote sensing physics. *Geoscience and Remote Sensing, IEEE Transactions on*, 46(5):1301–1312.

Tibshirani, R. (1996). Regression shrinkage and selection via the lasso. *Journal of the Royal Statistical Society, Series B*, 58:267–288.

Tropp, J. (2004). Greed is good: algorithmic results for sparse approximation. *Information Theory, IEEE Transactions on*, 50(10):2231–2242.

Tsai, F. and Philpot, W. (1998). Derivative analysis of hyperspectral data. *Remote Sensing of Environment*, 66:4151.

Tsai, F. and Philpot, W. D. (2002). A derivative-aided hyperspectral image analysis system for land-cover classification. *Geoscience and Remote Sensing, IEEE Transactions on*, 40(2):416–425.

Ungar, S., Pearlman, J., Mendenhall, J., and Reuter, D. (2003). Overview of the earth observing one (eo-1) mission. *Geoscience and Remote Sensing, IEEE Transactions on*, 41(6):1149–1159.

van der Meer, F., Jong, S. D., and Bakker, W. (2001). *Imaging spectrometry: basic principles and prospective applications*. Kluwer Academic Publishers.

Vogel, C. R. (2002). *Computational methods for inverse problems*. Philadelphia: Society for Industrial and Applied Mathematics.

Wang, G. and Weng, Q., editors (2013). *Remote Sensing of Natural Resources*. CRC Press.

Wang, Z., Bovik, A. C., Sheikh, H. R., and Simoncelli, E. P. (2004). Image quality assessment: from error visibility to structural similarity. *Image Processing, IEEE Transactions on*, 13(4):600–612.

Wei, Q., Dobigeon, N., and Tourneret, J.-Y. (2013). Bayesian fusion of multi-band images. *ArXiv e-prints*, tbd:tbd.

Winter, M. E. (1999). N-findr: an algorithm for fast autonomous spectral end-member determination in hyperspectral data.

Winter, M. E., Winter, E. M., Beaven, S. G., and Ratkowski, A. J. (2002). Hyperspectral image sharpening using multispectral data. In *Aerospace Conference, 2002 IEEE*, pages 1–9.

Yang, Z., Zhou, G., Xie, S., Ding, S., Yang, J.-M., and Zhang, J. (2011). Blind spectral unmixing based on sparse nonnegative matrix factorization. *Image Processing, IEEE Transactions on*, 20(4):1112 –1125.

Yokoya, N., Chanussot, J., and Iwasaki, A. (2014). Nonlinear unmixing of hyperspectral data using semi-nonnegative matrix factorization. *Geoscience and Remote Sensing, IEEE Transactions on*, 52(2):1430–1437.

Yokoya, N., Yairi, T., and Iwasaki, A. (2011). Coupled non-negative matrix factorization (cnmf) for hyperspectral and multispectral data fusion: Application to pasture classification. In *Geoscience and Remote Sensing Symposium (IGARSS), 2011 IEEE International*, pages 1779–1782.

Yokoya, N., Yairi, T., and Iwasaki, A. (2012). Coupled nonnegative matrix factorization unmixing for hyperspectral and multispectral data fusion. *Geoscience and Remote Sensing, IEEE Transactions on,*, 50(2):528–537.

Zhang, Y., Duijster, A., and Scheunders, P. (2012). A bayesian restoration approach for hyperspectral images. *Geoscience and Remote Sensing, IEEE Transactions on*, 50(9):3453–3462.

Zhukov, B., Oertel, D., Lanzl, F., and Reinhackel, G. (1999). Unmixing-based multisensor multiresolution image fusion. *Geoscience and Remote Sensing, IEEE Transactions on*, 37(3):1212 –1226.